Geologic and Structural Characterization of Shallow Seismic Properties Along The San Jacinto Fault at Sage Brush Flat, Southern California

by

Adam Wade

A Thesis Presented in Partial Fulfillment
of the Requirements for the Degree
Master of Science

Approved June 2018 by the
Graduate Supervisory Committee:

Ramon Arrowsmith, Chair
Stephen Reynolds
Duane DeVecchio

ARIZONA STATE UNIVERSITY

August 2018

ABSTRACT

The study of fault zones is a critical component to understanding earthquake mechanics and seismic hazard evaluations. Models or simulations of potential earthquakes, based on fault zone properties, are a first step in mitigating the hazard. Theoretical models of earthquake ruptures along a bi-material interface result in asymmetrical damage and preferred rupture propagation direction. Results include greater damage intensity within stiffer material and preferred slip in the direction of the more compliant side of the fault. Data from a dense seismic array along the Clark strand of the SJFZ at Sage Brush Flat (SGB) near Anza, CA, allows for analysis and characterization of shallow (<1km depth) seismic structure and fault zone properties. Results indicate potential asymmetric rock damage at SGB, similar to findings elsewhere along the SJFZ suggesting a NW preferred rupture propagation.

In this study, analysis of high resolution topography suggests asymmetric morphology of the SGB basin slopes are partially attributed to structural growth and fault zone damage. Spatial distributions of rock damage, from site mapping and fault perpendicular transects within SGB and Alkali Wash, are seemingly asymmetric with pulverization dominantly between fault strands or in the NE fault block. Remapping of the SJFZ through Alkali Wash indicates the fault is not isolated to a single strand along the main geologic boundary as previously mapped. Displacement measurements within SGB are analogous to those from the most recent large earthquake on the Clark fault. Geologic models from both a 3D shear wave velocity model (a product from the dense seismic array analysis) and lithologic and structural mapping from this study indicate surface observations and shallow seismic data compare well. A synthetic three-

dimensional fault zone model illustrates the complexity of the structure at SGB for comparison with dense array seismic wave products. Results of this study generally agree with findings from seismic wave interpretations suggesting damage asymmetry is controlled by an NW preferred rupture propagation.

DEDICATION

This thesis is dedicated to the following:

My loving and caring wife for her constant love and support, and making a home that always feels safe and inviting at the end of so many long days. I am blessed to have such a wonderful person always by side.

My brother for spending countless hours on the phone making me laugh when I needed it most.

My father and stepmother for providing their kindness, generosity, and support through so many of my life's transitions.

The officers and soldiers of the U.S. Army who provided me with my first topographic map and inspiration to understand the earth's landforms and all the wonder below my feet

ACKNOWLEDGMENTS

I am incredibly grateful to my advisor Ramon Arrowsmith for accepting me as his student and providing me with this exciting research project. His expertise and knowledge of earthquake physics and geology has been and continues to be a huge source of inspiration. I hope I am fortunate enough to continue working with such talented geologists in the future. I appreciate greatly the advice of my committee members Duane DeVecchio and Stephen Reynolds. Their passion for geology and teaching has motivated me, both in my research and work as a teacher's assistant. Many thanks to Pieter-Edward Share for all his help and technical expertise with the geophysical data. His countless correspondences despite his busy schedule were incredibly helpful and insightful. Thank you to my colleagues in the Arrowsmith lab, not only for the encouragement and technical support, but the many laughs along the way.

I'd also like to acknowledge the late Bud Wellman and his family for granting me access to their property to conduct my research. Not only did they allow me to live and work there, but treated me like family and always welcomed me with hugs and smiles. I am grateful I was able to meet Bud before he passed, and I will always remember him for his jokes, smiles, and passion for adventure, even when he could no longer wander out the door.

The research detailed in this thesis was supported by funding through the Southern California Earthquake Center (Award 17085) and through the Strategic University Research Partnership with NASA Jet Propulsion Laboratory. Thank you to the collaborators on this project including Yehuda Ben-Zion, Frank Vernon, and Andrea Donnellan for all their assistance.

TABLE OF CONTENTS

Page

Page

CHAPTER

LIST OF TABLES

Table Page

LIST OF FIGURES

LIST OF FIGURES

CHAPTER 1

INTRODUCTION

1.0 Introduction

The study of fault zones is an important field within geology, providing insights into the location and mechanics of earthquakes. The overarching goal of these studies is to improve the understanding of active fault behavior and to develop physical models that better predict earthquake recurrence, magnitude, and coseismic ground motions. Studies of fault zones and fault zone architecture reveal three principle phases; 1) fault core, where the majority of slip is accommodated, 2) damage zone, consisting of pulverized, brecciated and/or intensely fractured rock, and 3) protolith or undamaged rock (e.g. Chester et al., 1993; Cain et al., 1996; Mitchell and Faulkner, 2009) (Figure1-1). Fault zones may produce interfaces separating bodies of differing material properties: compliant vs. stiff (i.e., damaged material or different rock types) (Dor et al., 2006). Models of rupture along such a bi-material interface show a preference to rupture in the direction of slip of the compliant material and spontaneous generation of damage in the bulk on the stiffer side of the fault (Ben-Zion and Shi, 2005; Shi and Ben-Zion, 2005) (Figure 1-2). Field studies of fault zones have validated this model along the San Andreas, Punchbowl, North Anatolian faults, and the Arima-Takatsuki tectonic line (e.g., Dor et al., 2006; Dor et al., 2008; Mitchel et al., 2011).

The San Jacinto Fault Zone (SJFZ), is considered the most active fault in southern California (Sanders and Kanamori, 1984), splaying from the southern segment of the San Andreas fault (SAF) south of the Transverse Ranges, trending through the Peninsular

Ranges, and terminating within the Imperial Valley of the Salton Trough (Sharp, 1967) (Figure 1-3). The SJFZ is not limited to a single strand, but rather is composed of a complex network of faults that distribute strain across both parallel and orthogonal structures--features observed in early stages of strike slip fault maturation in laboratory experiments (e.g. Wilcox et al., 1973; Reber et al., 2015; Hatem et al., 2017).

Along the SJFZ, fault zone damage asymmetry has been observed as more damage on the NE side of the fault, via studies of fault zone trapped waves (Lewis et al., 2005; Qiu et al., 2017; Share et al; 2017; Qin et al. 2018), fault outcrops (Dor et al., 2006), and DEM analysis (Wechsler et al., 2009); possibly indicating a preferred NW rupture propagation direction for large earthquakes (Figure1-4). However, micro-structural analyses of fault zone architecture along the SJFZ have found an opposite sense of asymmetry (greater in the SW) (Peppard et al., 2018) indicating the potential for different controls of damage zone extent.

Deployment of a dense seismic array along the SJFZ, to characterize fault zone structure in the shallow (<1 km depth) crust, identified fault zone trapped waves exclusively on the NE side of the main seismogenic fault. The purpose of the study described in this thesis is to discern the distribution of geology, structure, and rock damage within the vicinity of the dense seismic array. Topics covered in this thesis include a review of previous studies of the SJFZ, structural and geologic research at the SGB study site, interpretation of geophysical data, and supplemental data products. Chapter 1 includes this introduction and a summary of the geology, timing, nomenclature, seismic structure, and surface fault zone structural studies along the SJFZ. Chapter 2 constitutes all the research elements including descriptions of previous and

ongoing geophysical research from the SGB dense array, methods, analyses, results, and interpretations from this study. Chapter 3 provides a discussion of the site mapping, interpretations, and comparison with data products from the dense array, along with conclusions and recommendations for further research. At the end of each chapter is a list of references cited, and the final section of the thesis lists references for the entire document.

1.1 Fault Zone Damage and Earthquake Rupture Propagation

A fault zone generally consists of the fault core, fractured rock from coseismic rock damage (damage zone), and the undamaged rock or protolith (e.g. Chester et al., 1993; Caine et al., 1996, Mitchell and Faulkner, 2009) (Figure 1-1). Rupture propagation along a fault may be unilateral, bilateral or omnidirectional (Sibson, 2011). The effect of rock damage and fault behavior are interconnected, and both the processes and properties at work within fault zones during fault rupture are subject of ongoing research in the field, laboratory, and numerical modeling.

Principal effects of earthquakes may include the nucleation and growth of rupture along a fault plane, strong ground motion, and stress and fluid pressure changes (Sibson, 2011). Failure along a fault plane is indicated by shear stress (τ_β), normal stress (σ_β) and pore-fluid pressure (p) expressed as Coulomb failure: $\sigma_f=\tau_\beta-\mu(\sigma_\beta-p)$ (King et al., 1994). Cotton and Coutant (1997) modeled both static and dynamic stress changes in a volume of plane-layered elastic medium. The rupture event was modeled as a northward unilateral rupture with similar seismic moment, length, and mechanism to the M_W7.3 1992 Landers, California, earthquake. Results of the static model show symmetrical

stress changes on either side of the fault, while the maxima of Coulomb stress changes are asymmetric with greater stress values on the eastern side of the fault (Figure 1-3c). Strike-slip faults form along vertical to sub-vertical planes and accommodate motion parallel to the earth's surface. At the focus of an earthquake along a fault, the surrounding volume of rock is divided into compressional and dilatational quadrants based on the initial seismic wave properties experienced in the quadrants (e.g. Whitcomb et al., 1971). Numerical calculations of dynamic ruptures in a homogenous solid indicate damage is produced preferentially in the two tensional quadrants (Ben-Zion and Shi, 2005) (Figure 1-2). Faults often juxtapose different earth material, creating an interface separating bodies of differing material classes and/or seismic wave velocities: compliant (lower velocity material) vs. stiff (higher velocity material). Numerical models of rupture in homogenous material versus along a bi-material interface produce symmetric bilateral cracks and uniform damage, contrasting with a unidirectional wrinkle-like pulse with asymmetrical damage (Ben-Zion and Shi, 2005; and Shi and Ben-Zion, 2005). Models of unidirectional wrinkle like ruptures produce dynamic dilation at the tip that propagates in the direction of slip on the more compliant side of the fault and dynamic compression at the tip propagating in the opposite direction (Ben-Zion and Shi, 2005). In the bi-material interface model, rupture propagates preferentially in the direction of slip of the compliant side, which persistently maintains the stiffer material in the tensile quadrant (Figure 1-3b). Because the tensile strength of rocks is significantly less than the compressive strength, the preferred rupture direction of large earthquakes can lead to an asymmetry of fault zone properties. Due to the confining pressures at greater depths, significant fault

normal damage extent is expected only in the top few kilometers of the earth's crust (Ben-Zion and Shi, 2005).

The above scenario describes a simulation of dynamic rupture on a material interface resulting in asymmetric damage across the fault. A special form of fault zone damage is rock pulverization; an intense fracturing of wall rock down to microscopic scales with little to no grain rotation (Dor et al., 2006). Laboratory experiments to create pulverized rock similar to that observed in the field require high strain rates, or supershear rupture, along a fault (Doan and Gary, 2009). Numerical simulations to create similar high strain rates capable of pulverizing rock mass far (~100 m) from the fault, only resulted from unrealistic rupture scenarios (Xu and Ben-Zion, 2017). To compensate for this discrepancy, Xu and Ben-Zion (2017) argue that pulverization occurs at lower strain rates on pre-damaged rocks. Two outcomes from the pulverization simulations include the following. 1) In homogenous material, tensile cracks form on both sides of the fault at high angles or orthogonal to the rupture plane. 2) Through repeated bi-material ruptures, asymmetrical damage occurs with more damage on the stiffer side of the fault with random fracture orientations. An intriguing consequence or the later result is a widening of the pulverized rock mass along pre-existing flaws, which can develop their own branches at greater distances from the fault (Xu and Ben-Zion, 2017).

If preferred rupture propagation is a valid natural phenomenon, it should be expressed/observed as asymmetric damage within fault zones. A number of studies have examined this topic on fault structures globally, including the SAF and the SJFZ. The following sections provide an introduction to the San Jacinto fault, its geologic setting

and segmentation, recent earthquake history, seismic structure, and geologic and geomorphic evaluations of fault zone damage.

1.2 Geology of the San Jacinto Fault Zone

The SJFZ is a major splay of the SAF in Southern California, and accommodates a similar amount of slip of the Pacific-North American plate boundary as the southern SAF (Bennet et al., 2004; Meade and Hager, 2005; Li and Liu, 2007; Lundgren et al., 2009). Sharp (1967) estimated cumulative right-lateral offset of roughly 24 km along the SJFZ in the Peninsular Ranges. By comparing his total offset to that of the entire SAF, and by measuring displacements of Quaternary deposits, Sharp classified the SJFZ a young structure limiting the maximum age of the fault to the Pliocene. His estimate of relative age has been further examined and supported by multiple studies (e.g., Matti and Morton, 1993; Morton and Matti, 1993; Lutz et al., 2006) discussed further in Section 1.2.

The central SJFZ is divided into five major strands: 1) Hot Springs fault (HSF), 2) Buck Ridge fault (BRF), 3) Thomas Mountain fault (TMF), 4) Coyote Creek fault (CCF), and 5) San Jacinto fault (SJF) which was later termed the Clark Fault (CF) (Figures 1-3, 1-4, 1-5, and 1-6). The bedrock geology is predominantly composed of Cretaceous plutonic and metamorphic rock (Figures 1-5 and 1-6) which are overlain by Quaternary deposits, including the Pleistocene Bautista sediments of Frick (1921). In the vicinity of Anza, the SJFZ structure is complex with multiple strands. At the northern and southern borders of Thomas Mountain are the N-S and NW-SE trending TMF and CF, respectively (Figure 1-6). At the eastern margin of Anza Valley, a splay branches from the CF and converges with the TMF, changing trend towards the east, where the BRF begins

(Figures 1-5 and 1-6). The coalescence of these fault structures occurs within, or adjacent to Burnt Valley, which is filled with Bautista and undifferentiated alluvial sediments. Burnt Valley is situated between Lookout Mountain and Table Mountain to the north and south, respectively (Figure 1-6). At the northern base of Table Mountain, the SFJZ includes a pair of northern and southern shallow dipping thrust faults, juxtaposing metamorphic rock of the Burnt Valley Complex (BVC) over Bautista, and tonalite of the Coahuila Valley Pluton (CVP) over BVC. Along strike to the NW, the southern thrust fault evolves into multiple faults with varying sense of slip in a small basin termed Sage Brush Flat (SGB).

1.3 Initiation of the San Jacinto Fault Zone

Determining the timing and mechanics of the SJFZ inception through traditional palinspastic restoration is difficult, as much of the fault displaces crystalline rocks and terrain uplifted from an ancestral (Cretaceous) tectonic system, with resulting complex fault zone geometry. The 24 km cumulative offset of the SJFZ (Sharp, 1967) is just under 10% of the total offset measured on the entire SAF (Crowell, 1962; Sharp, 1967; Matthews, 1976; Graham et al., 1989), which lead many workers to suspect, correctly, that the SJFZ is a much younger fault within the SAF system. Using a constant average slip rate of 10 mm/yr, (Sharp, 1981; Rockwell, 1990) and 24 km cumulative offset along the SJFZ (Sharp, 1967) yields an inception age of 2.4 Ma, however, models and stratigraphic analyses suggest the fault is younger by roughly 1 Myr (Matti and Morton, 1993; Morton and Matti, 1993; Lutz et al., 2006; Li and Liu, 2007).

Initiation of the SJFZ is thought to have resulted from development of a left bend in the Mission Creek strand of the SAF circa 4.0 to 2.5 Ma, at a location known as the "San Gorgonio Pass knot" (Figure 1-3) (Matti and Morton,1993; Morton and Matti,1993). This complex structure of contractional and extensional faults, ultimately led to initiation of the SJFZ at approximately 1.5 to 1.2 Ma, as a new structure transferring right slip around the complex "knot" (Matti and Mortion, 1993). Within or adjacent to the Transverse Ranges, initiation of the new structure involved activation or acceleration of uplift of the eastern San Gabriel Mountains and San Gorgonio Pass, as well as inception of basin deposition in San Bernardino and San Jacinto, and cessation of deposition in the San Timoteo badlands. Based on the stratigraphic ages and depositional rates within the basins, as well as slip rates estimated in the northern part of the San Timoteo badlands, Morton and Matti (1993) concluded that right slip along the fault began around 1.5 Ma.

Evidence for the SJFZ inception model described above is based primarily on data from the northwest portion of the fault, at or near convergence with the SAF. The geology in the central and southeast portion, and through the Peninsular Ranges, of the SJFZ consists of Mesozoic crystalline rock overlain by younger Quaternary sediments (Sharp, 1967), which makes estimating the age of the SJFZ in this section problematic. To constrain timing of the SJFZ initiation in the southeast, and to better understand Pliocene-Pleistocene faulting history in Southern California, Lutz et al. (2006) performed a detailed study of Borrego Badlands stratigraphy. The southwestern portion of the Salton Trough contains a sedimentary record from the Miocene through the Pleistocene. Based on the thickness and spatial distribution of sedimentary units, and basin rotation

(recorded by paleo-current data and magnetostratigraphy), this high resolution stratigraphic study concluded initiation of the SJFZ in the Borrego Badlands occurred 1.1 Ma (Lutz et al., 2006).

1.4 Recent Earthquakes and Slip Rates on the San Jacinto Fault near Anza

Between 1890 and 1969 there were nine ($6<M<7$) earthquakes along the SJFZ between the convergence with the SAF (Cajon Pass), and Superstition Mountain (Thatcher et al., 1975). Four of the earthquakes occurred in the early part of the 20th century (1899 – 1923) NW of Anza, and the remaining five occurred during the early to mid 20th century (1937 – 1969) SW of Anza. Thatcher et al. (1975) estimated the average seismic slip ($\bar{u}$) of each earthquake by determining the seismic moment (M_0) and area of rupture (A) using a constant shear modulus (μ): $M_0 = \mu\, \bar{u}\, A$. Mapping the seismic slip distribution of the nine moderate earthquakes reveals a roughly 40 km gap between Anza and Coyote Mountain bordering Borrego Valley(Borrego Badlands) (Thatcher et al., 1975) (Figure 1-1). Thatcher et al. (1975) noted a complex fault zone at Anza, with multiple fault strands as mapped by Sharp (1967) and concluded the gap may indicate strain accumulation and thus a locus for a future moderate earthquake. In the same vicinity, Sanders and Kanamori (1984) evaluated the location of earthquake epicenters along the SJFZ, revealing a 20 km quiescent segment of the fault known as the "Anza Seismic Gap" (Figure 1-3). The implications of the gap in seismic slip and seismicity include an increased hazard for a large magnitude earthquake. This has spurred a number of focused studies to establish the paleoseismic record of large earthquakes along this

segment of the SJFZ (e.g; Salisbury et al., 2012; Rockwell et al., 2015; Salisbury et al., 2017).

Estimating slip rates is critical to evaluating fault activity and seismic hazard, based on detailed studies involving displacement measurements, dating geologic units, and determining prior earthquake events recorded in geologic layers. Slip rates are often variable across different strands and segments. At the southern base of Table Mountain north of Anza, an alluvial fan consisting of Bautista deposits, incised by younger channels, has been the subject of two SJFZ slip rate studies (Sharp, 1981; Rockwell et al., 1990) (Figure 1-5). Previous mapping and displacement measurements of marker gravels, and dating of the 760 ka Bishop tuff, yield a slip rate of roughly 8 to 12 mm/yr (Sharp, 1981). Through further mapping of the late Quaternary deposits, ^{14}C dating and detailed soil profiles, Rockwell et al. (1990) validated Sharp's estimate at a finer scale deriving slip rates since 9.5, 14, 17, and 50 ka at 9.2, 11, 12, and 13 mm/yr, respectively. Using a long-term average slip rate of 12 mm/yr, the authors of the latter study concluded between 0.8 and 1.1 m of slip accumulation on the Anza segment of the SJFZ based on the potential of through going ruptures from 1918 or 1899 earthquakes, respectively.

The 1995 *Working Group on California Earthquake Probabilities* delineated the Clark fault (CF) as the 90 km Anza segment of the SJFZ. To establish the amount of slip for the most recent surface rupturing events (MRE) on the CF, Salisbury et al. (2012) measured 168 offset features using high resolution topography from lidar and field observations. Twenty-four of these offset measurements were made within Burnt Valley, NW of SGB, and ranged from 2.2 to 3.9 m with an average of approximately 3.3 m. Over the entire 80 km evaluated segment, average slip for the most recent earthquake,

postulated as 21 April 1918 M_w 6.9 earthquake, ranged from 2.5 to 2.9 m of dextral displacement, and a maximum of roughly 4 m at Anza.

Paleoseismic studies at Hog Lake (Rockwell et al., 2015) near the southern base of Thomas Mountain and roughly 5 km to the NW in the South Fork Wilderness (Salisbury et al., 2017) demonstrate at least two large surface rupture events on the CF in the past 300 years, inferred as the M_w 7.3 and M_w 6.9 events that occurred on 22 November 1800, and 21 April 1918, respectively.

1.5 Seismic Structure of the San Jacinto Fault Zone

There is significant work characterizing seismic structure of the SJFZ through evaluation of seismicity and seismic waves in the vicinity of Anza (Sanders and Kanamori, 1984; Li and Vernon, 2001; Lewis et al., 2005; Allam et al., 2014; Yang et al., 2014; Qiu et al., 2017; Ross et al., 2017; Share et al; 2017).

Seismicity is useful for evaluating fault zone structure by resolving earthquake hypocenters and focal mechanisms to indicate slip planes and fault geometry at depth. Employing this method at Anza, Sanders and Kanamori (1984) revealed a 20 km gap in seismicity compared to the previously reported 40 km seismic slip gap (Thatcher et al., 1975), and suggest the gap is resultant from a locked fault due to two primary mechanisms. The first involves convergent fault plane geometries of the CC, CF, and BRF interpreted from hypocentral locations. The second is the non-preferential orientation of the San Jacinto fault at Anza (N53˚W) with respected to the regional maximum compressive stress of N05˚E-S05˚W. These and other factors led Sanders and

Kanamori (1984) to conclude this locked segment of the SJFZ has a high potential for a large ($6 < M < 7$) earthquake.

Another useful feature for evaluating fault zones are low velocity zones detected from seismic energy or waves, radiated from earthquakes and other energy sources. Seismic waves traveling through rock mass decelerate when passing through fractured rock mass within fault zones and thus may define low velocity structures or zones. Within a low velocity zone, fault zone trapped waves (FZTW) are slow seismic energy associated with critically reflected phases, and in a coherent zone of damaged rock can act as a wave-guide highlighting the fault zone structure (Igel et al., 1997; Ben Zion, 1998). Near Anza, FZTW were identified along the BRF, CC and CF strands helping constrain shallow (3-5 km) fault zone structure and geometry (Li and Vernon, 2001; Lewis et al., 2005) (Figure 1-3). Three linear seismic arrays were installed across the fault strands listed above and recorded roughly 250 micro-earthquakes (Li and Vernon, 2001). Analysis of these events indicate the following; 1) a 25–30% reduction in shear wave velocity when passing through the three fault strands, 2) thrust faults located within Horse Canyon act as a shallow (< 10 km) barrier for wave-guides, 3) antithetic NW and SE dipping planes of the Clark and Buck Ridge faults, respectively as previously suggested (Sanders and Kanamori, 1984), and 4) continuation of the Clark fault through the Anza gap. Analysis of FZTW using the same arrays but evaluating earthquakes from sources outside the fault zone defined a roughly 100 m "trapping structure" at depths between 3 and 5 km (Lewis et al., 2005). Furthermore, the structure outlined by FZTW is not centered along the fault's surface trace, but offset by 50–100 m to the northeast (Lewis et al., 2005). Similar findings from linear arrays at Black Burn Saddle (Share et

al., 2017) and Jackass Flat (Qiu et al; 2017) report a roughly 200 m wide trapping structure along the SJFZ. In both cases, the fault separates material with higher and slower seismic wave velocities (bi-material interface) from the NE and SW, respectively, and the trapping structure is wider on the NE side of fault. These observations of asymmetric FZTW are significant and may suggest a preferred rupture propagation direction (Ben-Zion and Shi, 2005; Shi and Ben-Zion, 2006).

1.6 Fault Zone Structure and Rock Damage along the San Jacinto Fault Zone

Fault rocks observed at the surface, within fault zones, can vary in composition and texture depending on the age, mode, and depth of deformation. An early classification of fault rocks based on an exhumed fault, spanning the brittle-ductile boundary, provided a model for rock deformation in fault zones (Sibson, 1977). At or near the surface, rocks exclusively undergo brecciation. Sibson (1986) provided detailed descriptions of breccia and the mechanisms involved in its formation, after making post-earthquake observations on faults in southern California. These descriptions included discussions of fault zone complexities, e.g., dilatational and anti-dilatational fault jogs, and their role in perturbing earthquake ruptures and damaging the fault zone rocks. Exposed ancient faults associated with the SAF, such as the San Gabriel and Punch Bowl faults, provide an excellent resource for evaluating fault zone structure (Chester et al., 1993; Dor et al., 2006). A model for the internal structure of these faults include a core bordered by a roughly 100 m wide damage zone of the host rock (Chester et al., 1993) (Figure 1-1). A traverse across a bi-material interface, juxtaposing sandstone against igneous rock along the Punch Bowl fault, reveals higher fracture density and damage

intensity within the material with higher seismic wave velocity (sandstone) (Dor et al., 2006). In addition to damage asymmetry, Dor et al. (2006) described organized fractures in the sandstone with a preferred orientation and intensity values proportional to distance from the fault core. This contrasts with the igneous rock showing no dependency on distance to the fault, and damage style possibly related to other phases of deformation and/or metamorphic fabric (Dor et al., 2006).

Rock damage on the SJFZ has been observed at macro- (Wechsler et al., 2011), meso-/outcrop (Dor et al., 2006) and micro-scale (Morton, et al., 2012; Whearty et al., 2017; Peppard et al., 2018). Table 1 lists authors, methods, scales, and sense of damage asymmetry of all fault zone damage studies on the CF, and figure 1-4 depicts the study locations. Summaries of these studies are detailed in the following subsections.

1.6.1 Macro-scale Fault Zone Damage

Both movement of crustal plates and displacements along faults have clear and distinctive effects on topography and geomorphic processes. Mountain streams and drainages are effected by regional uplift of the earth's crust (e.g., Whipple, 2004) and through fracturing of the rock mass (e.g., Molnar et al, 2007). Although fracturing of rock mass within a fault zone from coseismic damage can initially increase permeability; successive damage and/or pulverization reduces the fractured rock grain size, ultimately decreasing permeability. This effect may increase moisture retention in the near surface, decreasing infiltration capacity, forcing more runoff and channel initiation, resulting in higher drainage density closer to the fault (Wechsler et al., 2009). This hypothesis was tested on the central CF (Figure 1-4) through analysis of digital elevation models (DEM) for geomorphic metrics, chiefly drainage density (Wechsler et al., 2009). Data sets

included broad (up to 2.5 km scale) and local (≤ 1 kilometer scale) topography from shuttle radar topography mission (SRTM) and B4 lidar 1-m DEMs, respectively. Both were analyzed using hydrologic modeling tools in a GIS to evaluate drainage patterns and variations in the drainage network. Taking into account changes in drainages associated with geologic material, the results from the SRTM analysis indicate a roughly 1-km wide damage zone centered on the CF. Further analysis of the 1-km swath using high resolution B-4 lidar indicates greater damage on the NE side of the fault (Wechsler et al., 2009). Wechsler et al. (2009) also describe more pronounced fault zone damage, recorded in the lidar analysis, in areas with complex structure, e.g. fault bends, double bends and junctions. The authors cautiously note that results of the study indicate damaged rock mass recorded in their analysis is most likely in the form of widely spaced fractures (5 – 20 cm scale) rather than pulverization, per se.

1.6.2 Meso/Outcrop-scale Fault Zone Damage

North of Anza, at the southern base of Thomas Mountain, three excavations along a 140-m long section of the CF exposed the fault core for a detailed structural analysis (Dor et al., 2006) (Figure 1-4). There, the CF juxtaposes middle and late Pleistocene alluvium and alluvial fan deposits. The fault core, in each exposure, was divided into structural domains based on fracture density and cumulative fracture length. An important uncertainty noted by Dor et al. (2006) is to what extent measured fractures formed in the gouge and deformed sedimentary layers are fault related structures as opposed to desiccation of the exposed clayey material. The three fault core exposures displayed consistent asymmetrical deformation with higher fracture densities and greater gouge extent on the NE side of the CF principle slip surface (Dor et al., 2006).

1.6.3 Micro-scale Fault Zone Damage

Three recent studies examined micro-structural properties of fault zone damage on the CF southwest of Anza (Morton et al., 2012; Whearty et al., 2017; and Peppard et al., 2018). Thin section and geochemical analysis from 61 samples collected along two transects across the CF in Horse Canyon revealed chemical alteration and elemental mass change within the fault core (Morton et al., 2012) (Figure 1-4). The fault zone architecture described in the Morton et al. (2012) study includes a primary and secondary fault core (gouge and cataclasite), transition zone (a matrix that supports small, lensoid tonalite fragments), and damage zone (rock fractures filled with dark, fine-grained material that thickens towards the fault). The total damage zone extents are 9 m and 1.25 m wide on the SW and NE side of the fault, respectively. However, the more intensely damaged rock within the fault core and transition zone is thicker on the NE side.

In Rock House Canyon, the SJFZ juxtaposes Cretaceous tonalite against Pleistocene Bautista sediments (Sharp, 1967). Thin section analysis of these rocks reveal intense fragmentation in the tonalite without grain rotation, and contrasting fracture densities in the Bautista with significantly higher values in samples from lower burial depths (Whearty et al., 2017). Cracks observed within the crystal faces exhibit fault normal preferred orientation consistent with studies on the SAF (Dor et al., 2009) which are attributed to dynamic rupture processes. Partial erosion of the damage zone within the Bautista prevented evaluation of lateral extent and possible asymmetry. However, the results from Whearty et al. (2017) demonstrate that rock pulverization can occur within the shallow subsurface at confining pressures as low as 1.4 to 2.4 MPa (i.e., ~100 m).

Within the Peninsular Range, the fault zone structure of the SJFZ is complex. It consists of multiple splays, dilatational jogs (between the CF and CCF), and thrust faults (Sharp, 1967) (Figure 1-5). Works described in the previous paragraphs focus primarily on damage associated with strike-slip faults of the main SJFZ or CF. South of SGB, 23 samples were collected at three locations within Alkali Wash to characterize damaged Bautista sediments, in the footwall of a SW dipping thrust fault (described as part of dismembered positive flower structure), for petrologic and clay minerology content, porosity, and crystal fragmentation (Peppard et al., 2018). At this location, contrasting ~10–12 cm and 15 m wide damage zones are observed within the Bautista sedimentary rock and Burnt Valley complex metamorphic rock on the NW and SE sides of the thrust fault, respectively. This contrasts with findings from Dor et al. (2006) who observed opposite damage asymmetry on the SJFZ, NE of Anza. Peppard et al. (2018) argue that host rock rheological differences (porous sedimentary vs. metamorphic rocks) control damage asymmetry along faults, consistent with a similar finding from laboratory experiments (Aben et al., 2017).

1.7 References

Allam, A.A., Ben-Zion, Y., Kurzon, I., and Vernon, F., 2014, Seismic velocity structure in the Hot Springs and Trifurcation areas of the San Jacinto fault zone, California, from double-difference tomography: Geophysical Journal International, v. 198, p. 978-999.

Aben, F.M., Doan, M., Gratier, J., and Renard, F., 2017, High strain rate deformation of porous sandstone and the asymmetry of earthquake damage in shallow fault zones: Earth and Planetary Science Letters, v. 463, p. 81-91.

Ben-Zion Yehuda, 1998, Properties of seismic fault zone waves and their utility for imaging low-velocity structures: Journal of Geophysical Research: Solid Earth, v. 103, p. 12567-12585,

Ben-Zion, Y., and Shi, Z., 2005, Dynamic rupture on a material interface with spontaneous generation of plastic strain in the bulk: Earth and Planetary Science Letters, v. 236, p. 486-496.

Bennett, R.A., Friedrich, A.M., and Furlong, K.P., 2004, Codependent histories of the San Andreas and San Jacinto fault zones from inversion of fault displacement rates: Geology (Boulder), v. 32, p. 961-964.

Brown, N.N., Fuller, M.D., and Sibson, R.H., 1991, Paleomagnetism of the Ocotillo Badlands, southern California, and implications for slip transfer through an antidilational fault jog: Earth and Planetary Science Letters, v. 102, p. 277-288.

Caine, J., Evans, J., and Forster, C., 1996, Fault zone architecture and permeability structure: Geology, v. 24, p. 1025-1028.

Chester, F., Evans, J.P., and Biegel, R., 1993, Internal structure and weakening mechanisms of the San Andreas Fault: Journal of Geophysical Research-Solid Earth, v. 98, p. 771-786.

Cotton, F., and Coutant, O., 1997, Dynamic stress variations due to shear faults in a plane-layered medium: Geophysical Journal International, v. 128, p. 676-688.

Crowell, J.C., 1962, Displacement Along the San Andreas Fault, California, *in* Crowell, J.C., ed., Displacement Along the San Andreas Fault, California: Geological Society of America.

Doan,M.L., Gary,G, 2009, Rock pulverization at high strain rate near the San Andreas fault: Nature Geoscience, v. 2, p. 709.

Dor, O., Rockwell, T., and Ben-Zion, Y., 2006, Geological Observations of Damage Asymmetry in the Structure of the San Jacinto, San Andreas and Punchbowl Faults in Southern California: A Possible Indicator for Preferred Rupture Propagation Direction: Pure and Applied Geophysics, v. 163, p. 301-349.

Dor, O., Yildirim, C., Rockwell, T.K., Ben-Zion, Y., Emre, O., Sisk, M., and Duman, T.Y., 2008, Geological and geomorphologic asymmetry across the rupture zones of the 1943 and 1944 earthquakes on the North Anatolian Fault: possible signals for preferred earthquake propagation direction: Geophysical Journal International, v. 173, p. 483-504.

Dor, O., Chester, J., Ben-Zion, Y., Brune, J., and Rockwell, T., 2009, Characterization of Damage in Sandstones along the Mojave Section of the San Andreas Fault: Implications for the Shallow Extent of Damage Generation: Pure and Applied Geophysics, v. 166, p. 1747-1773.

DiPietro, J.A., 2013, Chapter 17 - California Transpressional System, *in* DiPietro, J.A., ed., Landscape Evolution in the United States: Boston, Elsevier, p. 281-305.

Frick, C., 1921, Extinct vertebrate faunas of the Badlands of Bautista Creek and San Timoteo Cañon, Southern California: Berkeley: University of California Press.

Graham, S., and Stanley, R., 1989, Oligocene and Miocene Paleogeography of Central California and Displacement Along the San Andreas Fault: Geological Society of America.Geological Society of America Bulletin, v. 101, p. 711.

Hatem, A.E., Cooke, M.L., and Toeneboehn, K., 2017, Strain localization and evolving kinematic efficiency of initiating strike-slip faults within wet kaolin experiments: Journal of Structural Geology, v.101, p. 96–108.

Igel, H., Ben-Zion, Y. & Leary, P., 1997, Simulation of SH and P SV wave propagation in fault zones: Geophysical Journal International, v. 128, p. 533–546.

King, G., Stein, R., and Lin, J., 1994, Static stress changes and the triggering of earthquakes: Bulletin of the Seismological Society of America, v. 84, p. 935-953.

Lewis, M.A., Peng, Z., Ben-Zion, Y., and Vernon, F.L., 2005, Shallow seismic trapping structure in the San Jacinto fault zone near Anza, California: Geophysical Journal International, v. 162, p. 867-881.

Li Y., and Vernon, F.L., 2001, Characterization of the San Jacinto fault zone near Anza, California, by fault zone trapped waves: Journal of Geophysical Research: Solid Earth, v. 106, p. 30671-30688.

Li, Q., and Liu, M., 2007, Initiation of the San Jacinto Fault and its Interaction with the San Andreas Fault: Insights from Geodynamic Modeling: Pure and Applied Geophysics, v. 164, p. 1937-1945.

Lundgren, P., E. A. Hetland, Z. Liu, and E. J. Fielding (2009), Southern San Andreas-San Jacinto fault system slip rates estimated from earthquake cycle models constrained by GPS and interferometric synthetic aperture radar observations, Journal of Geophysical Research, v. 114.

Lutz, A., Dorsey, R., Housen, B.A., and Janecke, S., 2006, Stratigraphic record of Pleistocene faulting and basin evolution in the Borrego Badlands, San Jacinto fault zone, Southern California: Geological Society of America Bulletin, v. 118, p. 1377-1397.

Matti, J.C., and Morton, D.M., 1993, Chapter 2: Paleogeographic evolution of the San Andreas fault in southern California: A reconstruction based on a new cross-fault correlation: in Powell, R.E., et al., eds., The San Andreas fault system: Displacement, palinspastic reconstruction, and geologic evolution: Geological Society of America Memoir, v. 178, p. 107-159.

Matthews III, Vincent. 1976, Correlation of Pinnacles and Neenach Volcanic Formations and Their Bearing on San Andreas Fault Problem: AAPG Bulletin. v. 60, p. 2128-2141.

Meade, B. J., and B. H. Hager (2005), Block models of crustal motion in southern California constrained by GPS measurements, Journal of Geophysical Research, v.110.

Mitchell, T.M., and Faulkner, D.R., 2009, The nature and origin of off-fault damage surrounding strike-slip fault zones with a wide range of displacements: A field study from the Atacama fault system, northern Chile: Journal of Structural Geology, v. 31, p. 802-816.

Mitchell, T.M., Ben-Zion, Y., and Shimamoto, T., 2011, Pulverized fault rocks and damage asymmetry along the Arima-Takatsuki Tectonic Line, Japan: Earth and Planetary Science Letters, v. 308, p. 284-297.

Molnar, P., R. S. Anderson, and S. P. Anderson (2007), Tectonics, fracturing of rock, and erosion, Journal of Geophysics, v. 112. Res., 112.

Morton, D.M., and Matti, J.C., 1993, Extension and contraction within an evolving divergent strike-slip fault complex: The San Andreas and San Jacinto fault zones at their convergence in Southern California, in Powell, R.E., et al., eds., The San Andreas fault system: Displacement, palinspastic reconstruction, and geologic evolution: Geological Society of America Memoir 178, p. 217–230.

Morton, N., Girty, G.H., and Rockwell, T.K., 2012, Fault zone architecture of the San Jacinto fault zone in Horse Canyon, southern California: A model for focused post-seismic fluid flow and heat transfer in the shallow crust: Earth and Planetary Science Letters, v. 329-330, p. 71-83.

Peppard, D.W., Webb, H.N., Dennis, K., Vierra, E., Girty, G.H., Rockwell, T.K., Blanton, C.M., Brown, J.F., Goldstein, A.I., Kastama, K.W., Korte-Nahabedian, M., Puckett, D., and Richter, A.K., 2018, Micro-scale damage characterized within part of a dismembered positive flower structure, San Jacinto fault, southern California, USA: Journal of Structural Geology, v. 112, p. 53-68.

Qin, L., Ben-Zion, Y., Qiu, H., Share, P., Ross, Z.E., and Vernon, F.L., 2017, Internal structure of the San Jacinto fault zone in the trifurcation area southeast of Anza, California, from data of dense seismic arrays: Geophysical Journal International, v. 213, p. 98-114.

Qiu, H., Ben-Zion, Y., Ross, Z.E., Share, P.-., and Vernon, F.L., 2017, Internal structure of the San Jacinto fault zone at Jackass Flat from data recorded by a dense linear array: Geophysical Journal International, v. 209, p. 1369-1388,

Reber, J.E., Lavier, L.L., and Hayman, N.W., 2015, Experimental demonstration of a semi-brittle origin for crustal strain transients: Nature Geoscience, v. 8, p. 712–715.

Ross, Z., Hauksson, E., and Ben-Zion, Y., 2017, Abundant off-fault seismicity and orthogonal structures in the San Jacinto fault zone: Science Advances, v. 3,

Rockwell, T., Loughman, C., and Merifield, P., 1990, Late Quaternary rate of slip along the San Jacinto Fault Zone near Anza, southern California: Journal of Geophysical Research: Solid Earth, v. 95, p. 8593-8605.

Rockwell, T., Dawson, T., Young Ben-Horin, J., and Seitz, G., 2014, A 21-Event, 4,000-Year History of Surface Ruptures in the Anza Seismic Gap, San Jacinto Fault, and Implications for Long-term Earthquake Production on a Major Plate Boundary Fault: Pure and Applied Geophysics, v. 172, p. 1143-1165.

Salisbury, J.B., Rockwell, T.K., Middleton, T.J., and Hudnut, K.W., 2012, LiDAR and field observations of slip distribution for the most recent surface ruptures along the central San Jacinto Fault: Bulletin of the Seismological Society of America, v. 102, p. 598-619.

Salisbury, B., Rockwell, T., and Buga, M., 2017, Paleoseismic Evidence for the 21 April 1918 Mw 6.9 Surface Rupture of the Northern Clark Strand of the Central San Jacinto Fault, California: Bulletin of the Seismological Society of America, Berkeley CA, v. 107, p. 1027-1032.

Sanders, C.O., and Kanamori, H., 1984, A seismotectonic analysis of the Anza Seismic Gap, San Jacinto Fault Zone, southern California: Journal of Geophysical Research: Solid Earth, v. 89, p. 5873-5890.

Share, P., Ben-Zion, Y., Ross, Z.E., Qiu, H., and Vernon, F.L., 2017, Internal structure of the San Jacinto fault zone at Blackburn Saddle from seismic data of a linear array: Geophysical Journal International, v. 210, p. 819-832,

Sharp, R.V., 1981, Variable rates of Late Quaternary strike slip on the San Jacinto Fault Zone, southern California: Journal of Geophysical Research: Solid Earth, v. 86, p. 1754-1762.

Sharp, R.V., 1967, San Jacinto fault zone in the Peninsular Ranges of Southern California: Geological Society of America Bulletin, v. 78, p. 705-729.

Shi, Z., and Ben-Zion, Y., 2006, Dynamic rupture on a bimaterial interface governed by slip-weakening friction: Geophysical Journal International, v. 165, p. 469-484.

Sibson, R.H., 1977, Fault rocks and fault mechanisms: Journal of the Geological Society, v. 133, p. 191-213.

Sibson, R.H., 1986, Rupture Interaction with Fault Jogs, *in* Earthquake Source Mechanics: American Geophysical Union, p. 157-167.

Sibson, R., 2011, The scope of earthquake geology, in: Fagereng, A., Toy, V. G., and Rowland, J. V., ed., Geology of the Earthquake Source: A Volume in Honour of Rick Sibson. Geological Society, London, Special Publications, p. 319-331.

Thatcher, W., Hileman, J., and Hanks, T., 1975, Seismic Slip Distribution along the San Jacinto Fault Zone, Southern California, and Its Implications: Bulletin of the Geological Society of America, v. 86, p. 1140-1146.

Wechsler, N., Rockwell, T.K., and Ben-Zion, Y., 2009, Application of high resolution DEM data to detect rock damage from geomorphic signals along the central San Jacinto Fault: Geomorphology, v. 113, p. 82-96.

Whearty, J.J., 2017, Incipient pulverization at shallow burial depths along the San Jacinto fault, southern California, *in* Thomas, M.Y., ed., Fault Zone Dynamic Processes: Evolution of Fault Properties During Seismic Rupture, American Geophysical Union Monograph 227, p. 3-20.

Whipple, K.X., 2004, BEDROCK RIVERS AND THE GEOMORPHOLOGY OF ACTIVE OROGENS: v. 32, p. 151-185.

Whitcomb, J.H., Allen, C.R., Garmany, J.D., and Hileman, J.A., 1973, San Fernando Earthquake series, 1971: Focal mechanisms and tectonics: Reviews of Geophysics, v. 11, p. 693-730.

Wilcox, R.E., Harding, T.P. and Seely, D.R. (1973). Basic wrench tectonics. The American Association of Petroleum Geologists Bulletin 57:1, 74–96.

Xu, S., and Ben-Zion, Y., 2017, Theoretical constraints on dynamic pulverization of fault zone rocks: Geophysical Journal International, v. 209, p. 282–296.

Yang, H., and Zhu, L., 2010, Shallow low-velocity zone of the San Jacinto fault from local earthquake waveform modelling: Geophysical Journal International, v. 183, p. 421-432.

Yang, H., Li, Z., Peng, Z., Ben-Zion, Y., and Vernon, F., 2014, Low-velocity zones along the San Jacinto Fault, Southern California, from body waves recorded in dense linear arrays: Journal of Geophysical Research: Solid Earth, v. 119, p. 8976-8990.

Table 1: List of geologic and geomorphic studies conducted on the Clark strands of the SJFZ. Listing compiles study authors, scale of the analysis (e.g. micro vs. outcrop mapping), location along the fault and orientation of damage asymmetry if available.

Study	Scale	Methods	Geographic location	Sense of Damage Asymmetry
Dor et al. (2006)	Meso/outcrop	Fracture length and density mapping	N. of Anza, Ramon Indian Reservation	NE
Wechsler et al. (2009)	Macro	Geomorphic Analysis	Blackburn Canyon - Clark Valley	NE
Morton et al. (2012)	Micro	Thin section	Horse Canyon	SW
Whearty et al. (2017)	Micro	Thin section and geochemistry	Rock House Canyon	Asymmetry not Described
Peppard et al. (2018)	Micro	Thin section and geochemistry	Alkali Wash	SW

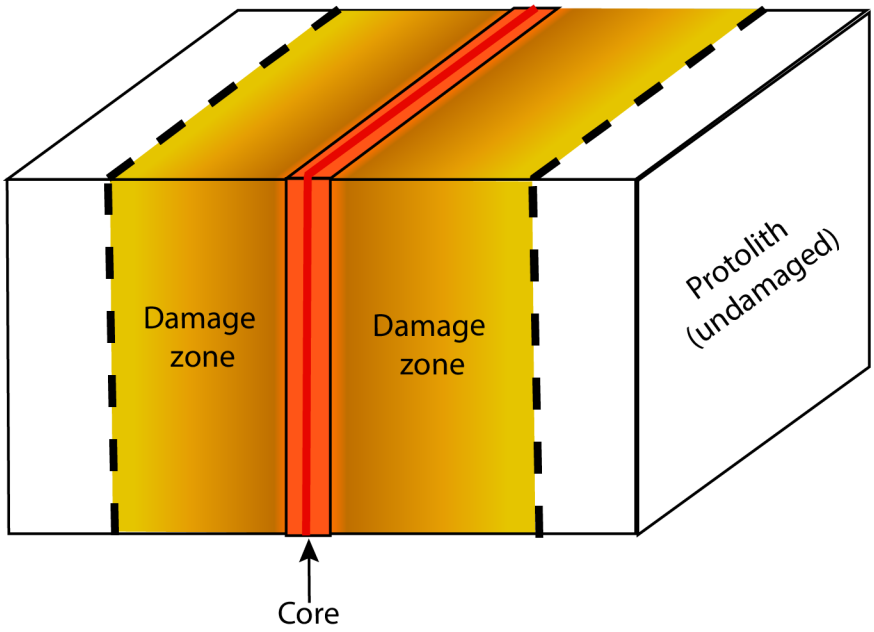

Figure 1-1: Schematic diagram of strike slip fault zone architecture. Major components include the fault core which is surrounded by a damage zone (damaged host rock), and protolith or undamaged host rock.

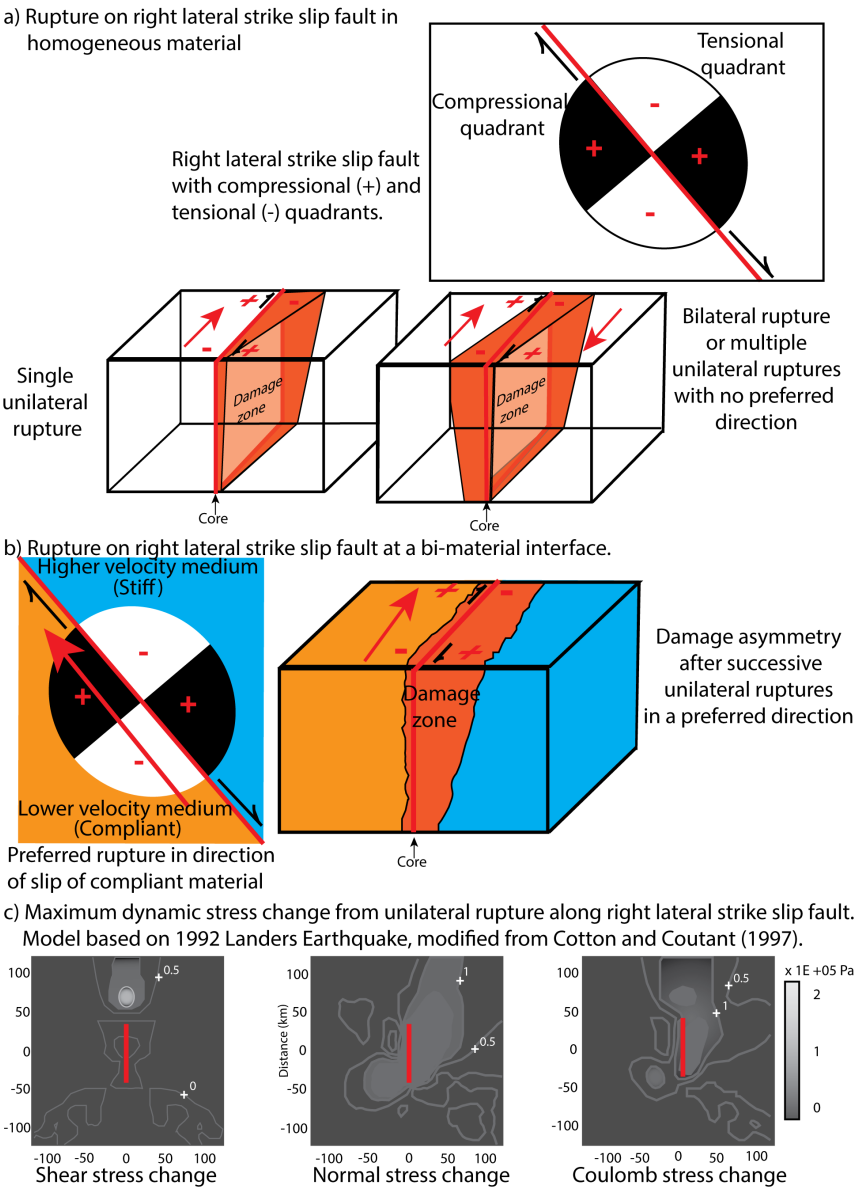

Figure 1-2: Conceptual sketches and model of fault ruptures on a right lateral strike slip fault. a) Upper right box shows compressional (+) and tensional (-) quadrants on a right lateral strike slip fault. Lower left block model depicts a single unilateral rupture (red arrow indicates rupture direction) with damage produced in tensional quadrant. Lower right block model depicts a single bilateral rupture or multiple unilateral ruptures with no preferred rupture direction. b) Left box shows stable self-sustaining rupture propagating along a material interface as a unidirectional pulse in the direction of slip on the more compliant side of the fault. Right block model depicts asymmetric damage zone development from successive unilateral ruptures from preferred rupture direction. c) Model of maxima dynamic stress change (white lines indicate stress contours) from a northward unilateral rupture propagation on a right lateral strike slip fault during the 1992 M_W 7.3 Landers earthquake, modified from Cotton and Coutant (1997).

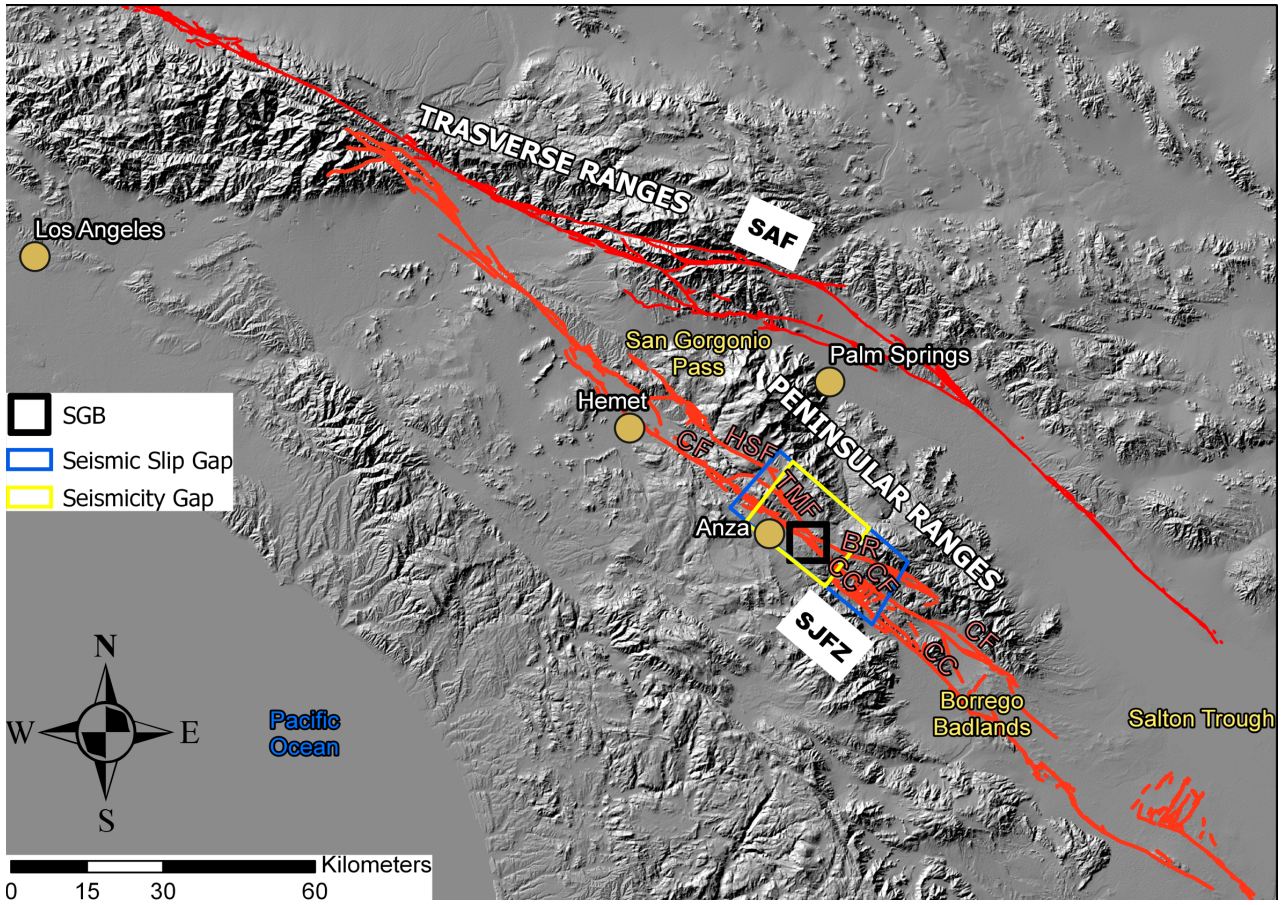

Figure 1-3:SRTM hillshade basemap with the San Andreas fault (SAF) and San Jacinto fault zone (SJFZ) shown s (USGS, 2006). Circles indicate populated areas and black box is centered on the SGB study area. Geographic locations labeled in yellow discussed in text. Dark blue and yellow rectangles, and black square outline the Anza seismic slip and seismicity gaps (Thatcher et al., 1975; Sanders and Kanamori., 1984) and the SGB study area, respectively. Red letters indicate fault segments of the central SJFZ; BR-Buck Ridge fault, CC-Coyote Creek fault, CF-Clark fault, HSF-Hot Springs fault, TMF-Thomas Mountain fault.

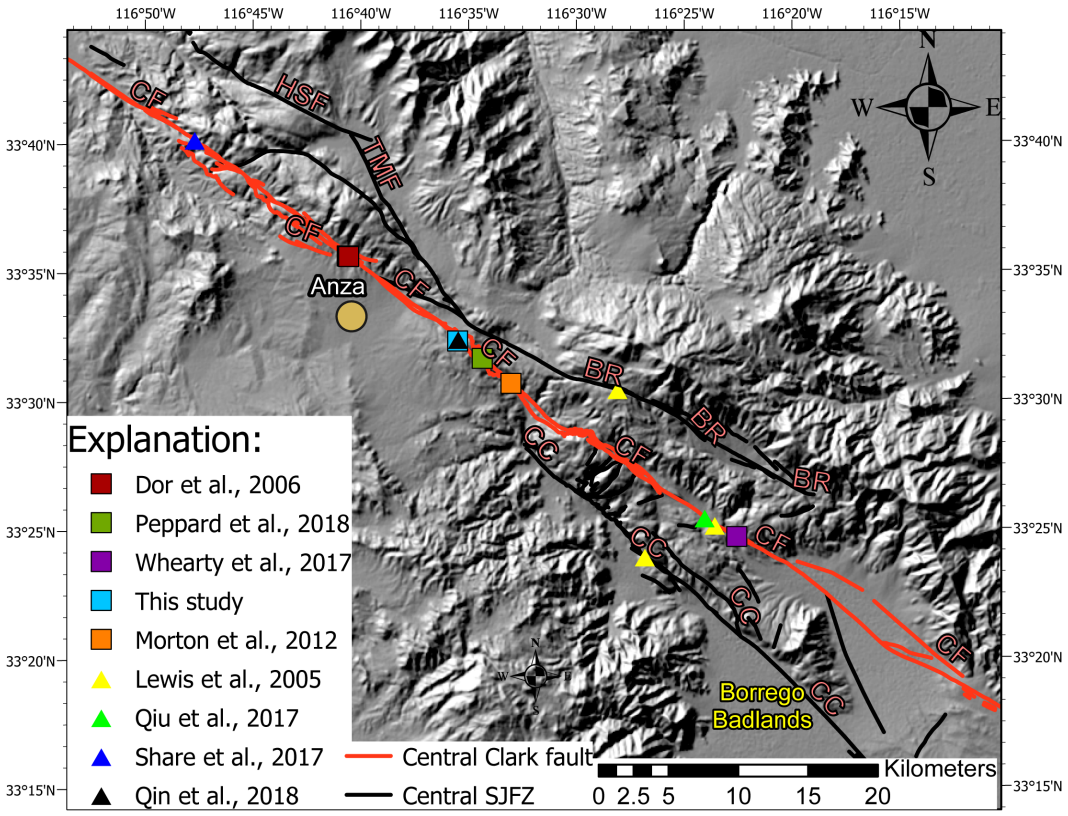

Figure 1-4: Fault zone damage study locations. SRTM hillshade base map with the central Clark strand of the SJFZ (red line) (USGS, 2006) evaluated by Wechsler et al. (2009) and other fault segments of the central SJFZ; all segments labeled in red letters; BR-Buck Ridge fault, CC-Coyote Creek fault, CF-Clark fault, HSF-Hot Springs fault, TMF-Thomas Mountain fault. Individual study locations of localized fault zone rock damage shown as triangles, for fault zone trapped wave studies using seismic arrays, and squares, for geologic and/or microstructural study locations. The town of Anza is shown for reference.

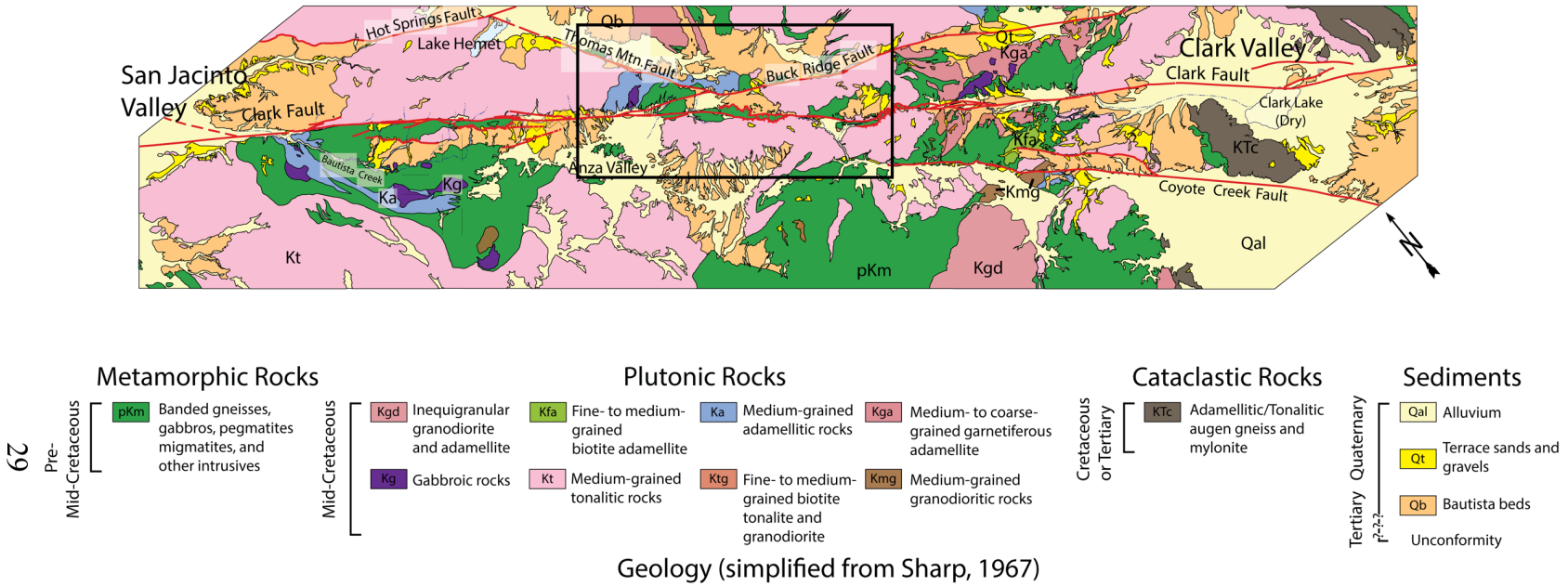

Figure 1-5: Generalized geologic map of the San Jacinto Fault Zone in the Peninsular Ranges, simplified from Sharp (1967) (Digitization by Salisbury in Salisbury et al., 2012). Black box indicates extent of Figure 1-6.

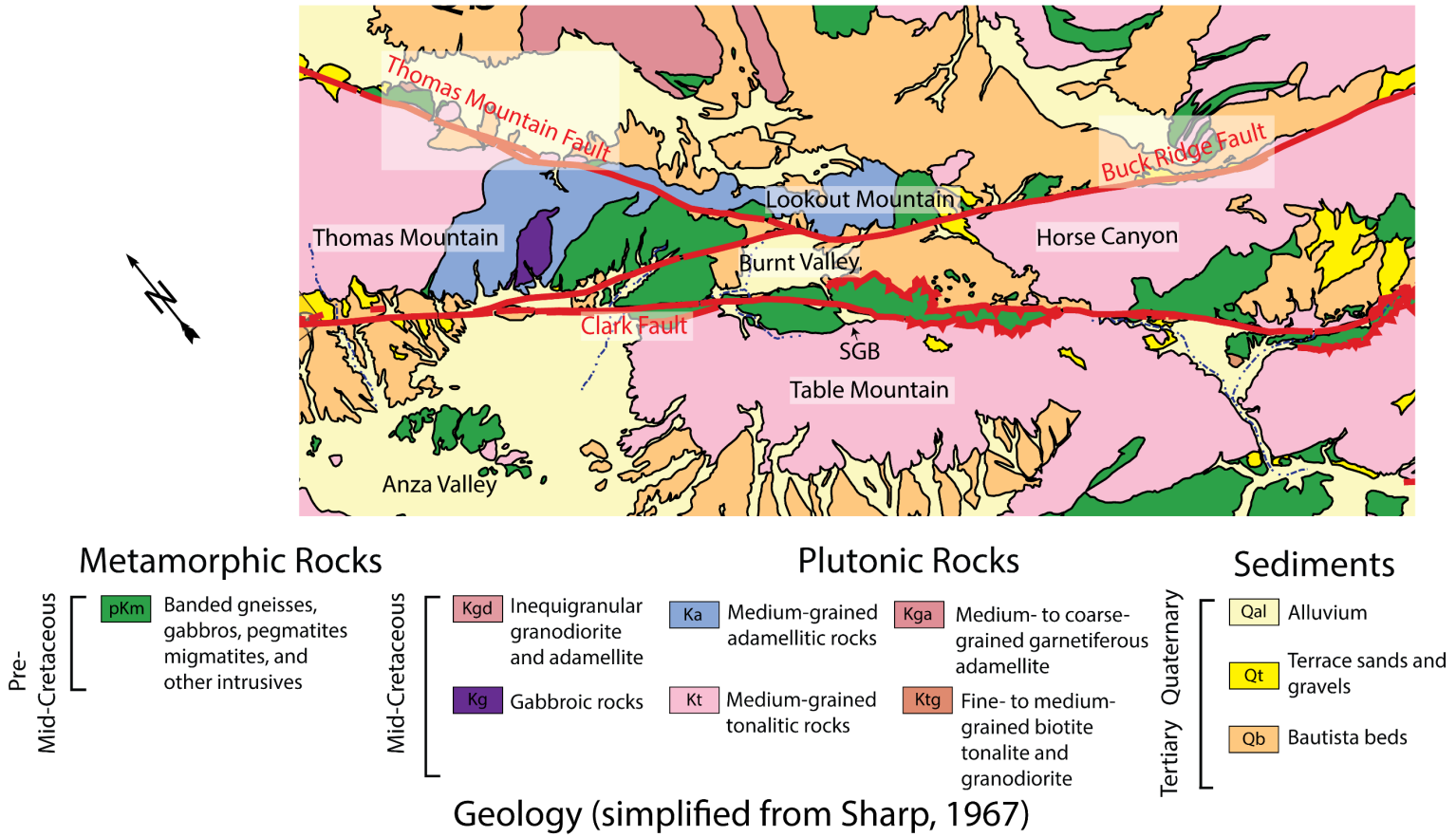

Figure 1-6: Generalized geologic map of the central San Jacinto Fault Zone simplified from Sharp (1967) (Digitization by Salisbury in Salisbury et al., 2012). SGB study location located as small patch of alluvium between pKm and Kt in the center portion of the map.

CHAPTER 2

GEOLOGIC AND STRUCTURAL CHARACTERIZATION OF THE ROCK VOLUME IMAGED BY THE DENSE NODAL SEISMIC ARRAY ALONG THE SAN JACINTO FAULT AT SAGE BRUSH FLAT, SOUTHERN CALIFORNIA

2.1. Introduction

Studies of structural properties of modern and ancient fault zones through geophysical imaging and observations of fault rocks are fundamental to understanding earthquake processes. Slip along a fault induces the formation of secondary damage zones within the host rock (Okubo and Schultz, 2005). In the shallow brittle crust, strike-slip fault zones typically consist of a fault core which accommodates primary slip, surrounded by damaged rock which transitions outward to intact protolith (e.g., Chester et al., 1993; Chester et al., 2004, Mitchel et al., 2011, Lin et al., 2013). Detailed imaging of fault zone velocity structure can reveal important information about the cumulative damage along the fault (Allam et al., 2014).

The San Jacinto fault zone (SJFZ) is a major splay of the San Andreas fault system (SAF) (Sharp, 1967), and is historically the most seismically active part of the plate boundary (Sanders and Kanamori, 1984) (Figure 1-3). Slip rates along the SJFZ have spatio-temporal variability, ranging from 8 mm/yr to 23 mm/yr (Sharp, 1967; Sharp, 1981; Rockwell et al., 1990; Morton and Matti, 1993; Rockwell et al., 2015). Initial mapping of the SJFZ within the Peninsular Ranges segmented the system into five

strands; Buckridge fault (BR), Coyote Creek fault(CC), Hot Springs fault (HSF), Thomas Mountain fault (TMF), and the San Jacinto fault (Sharp, 1967). A 40 km (Thatcher et al., 1974) and 20 km (Sanders and Kanamori, 1984) section of the SJFZ near the town of Anza is termed the "Anza seismic gap," due to a lack of seismic slip and seismicity. This section of the SJFZ was termed the Clark fault (CF) by the Working Group on California Earthquake Probabilities (1995). Evaluations of paleoseismicity near Anza indicate a relatively large earthquake recurrence interval of roughly 250 years (Rockwell et al., 2015), and detailed slip distribution observations along the CF estimate the most recent large (>M7) earthquake occurred on 22 November 1800 (Salisbury et al., 2012, 2017).

Multiple geophysical studies imaging fault-zone trapped waves (FZTW) (Lewis et al., 2005; Qiu et al. 2017; Share et al., 2017; Qin et al., 2017), outcrop mapping (Dor et al., 2006), and regional topographic analysis (Wechsler et al., 2011) (Figure 1-4), observe an asymmetric damage zone along the SJFZ. Results from each study indicate fault zone rock damage has a greater extent on the NE side. Fault zone damage asymmetry is a predicted outcome for preferred unidirectional rupture along a fault juxtaposing differing material types (bi-material interface) (Ben-Zion and Shi, 2005; Shi and Ben Zion, 2005) (Figures 1-3). In such a case, ruptures along the fault propagate preferentially in the slip direction of the compliant (low seismic velocity medium) side, which persistently places the stiffer (higher seismic velocity medium) in the tensional quadrant of the radiated seismic field. Within the fault zone, the expected result is an asymmetric pattern of damaged rock consistently observed on one side of the fault. The asymmetric damage described by FTZW, outcrop mapping, and topographic analyses, are possible indicators

for a preferred NW rupture propagation along the CF as explained by a unidirectional pulse rupture along a bi-material interface.

Along the CF, microstructural and geochemical analyses of fault zone rocks at Horse Canyon, Rock House Canyon, and Alkali Wash (Morton et al., 2012; Whearty et al., 2017; Peppard et al, 2018) help define fault zone architecture along the CF (Figures 1-4). At Rock House Canyon, partial erosion and colluvial cover prevent accurate measurements of damage zone width. However, petrographic analysis reveal clear pulverization of tonalite on the NE side of the fault and incipient pulverization of weakly consolidated sediments on the SW side (Whearty et al., 2017). In Horse Canyon, the damage zone (rock fractures filled with dark, fine-grained material that thickens towards the fault) extent is wider on the SW side of the fault, however the more intensely damaged transition zone (a matrix that supports small, lensoid tonalite fragments) is wider on the NE side (Morton et al., 2012). Fault zone architecture in Alkali Wash, reported from a transect across a dismembered positive flower structure (part of the CF), includes a fault core, followed by an inner intensely damaged zone, and a surrounding outer non-pervasively damaged zone (Peppard et al., 2018). Within the footwall, or NE side of the fault, a weakly consolidated sandstone has a narrow inner damage zone (10 – 12 cm thick) which contrasts with a much wider (5 m) thick inner damage zone in metamorphic rock observed in the hanging wall, SW side. Peppard et al. (2018) argue the asymmetric damage observed in Alkali Wash (within the depths of the sandstone), is indicative of rheological controls on rock damage extent rather than a preferred rupture direction, in agreement with recent laboratory results (Aben et al., 2017)

Imaging of fault zones through geophysical surveys and seismic wave analyses offer a glimpse of seismic structural properties; e.g. low velocity zones, FZTW, and waveform characteristics. What is often lacking from these informative investigations, however, is a clear connection linking individual geophysical elements to observed geologic units and structures in overlying rock mass. Most often this quandary results from two factors; 1) geophysical surveys often resolve fault zone structure at seismogenic depths and 2) interpretations are often simplified based on scales ranging from 100 m to 1 km. At Sage Brush Flat (SGB) near Anza, California, data from a dense seismic array deployed in a 10-m grid spacing to image the shallow crust (Ben-Zion et al., 2015), provide a special opportunity to test how fault zone seismic properties may manifest in the geology at the surface (Figure 2-1). This study addresses three main challenges in fault zone studies; 1) compare and contrast geophysical properties derived from the SGB dense array with surficial geologic and structural observations at a similar dekameter scale resolution, 2) evaluate fault zone structure and rock damage distribution to aid in the analysis of structural controls on damage asymmetry along the SJFZ, and 3) improve understanding of local geology and structural complexity within the vicinity of the SGB basin using high resolution topography.

Products from this research include maps of surficial geology and rock damage, and models of subsurface structure including a 3D model of the CF at SGB validated with high resolution seismic velocity tomography. Detailed in this chapter are the methods and results of mapped geology and structure, and fault zone damage within and around the dense array. These observations reveal, in general a greater NE damage

asymmetry; consistent with a NW fault rupture propagation direction, and damage extent which may grow along pre-existing flaws in rock mass. Use of high resolution topography helps identify multiple fault strands through Alkali Wash and retraces the active fault away from the main lithologic contact as previously mapped.

2.2 Review of SGB Dense Seismic Array Design and Results

A spatially dense array of geophones was deployed in the small (~700 m x 350 m) SGB basin from May to June of 2014 and has been used to develop a variety of new seismic imaging and earthquake detection techniques. The dense array was designed specifically to image shallow (upper 1 km) fault zone structure at high (~10 m or dekameter) resolution. The subsections below provide summaries of the SGB dense seismic array construction, and studies thereof.

2.2.1 Array Construction and Initial Observations

The array configuration includes 1108 geophones arranged in 20 rows with 50 sensors per row, perpendicular to the main trace of CF, at a roughly 10-m grid spacing recording data over a 4 week time period in 2014 (Ben-Zion, 2015). The remaining 108 sensors were added as extensions to selected rows within the grid. Total surface area coverage of the array is approximately 600 m x 600 m, incorporating the entire SGB basin and portions of the northeast and southwest slopes (Figure 2-1). The dense array augments continuous monitoring at SGB from a linear PASSCAL array of six (6) accelerometers, part of larger deployment spanning the SJFZ that began in 2010 (Vernon and Ben-Zion 2010).

In addition to detecting seismic events, the dense array recorded Betsy gunshots and noise data at a frequency of 500 s^{-1} to study fault zone seismic structure at SGB. The tight spacing of the dense array provides a special opportunity to study how wave fields propagate through the subsurface and to image structural features in the upper few hundred meters of the fault zone.

In describing the preliminary results, Ben-Zion et al. (2015) noted numerous recorded earthquakes during each day of the dense array deployment with a peak of 120 observed events in a single day. Anomalous spikes and bursts of high-frequency waves recorded in the array are explained as cultural noise and possibly the interaction of wind/weather with stationary equipment located on site. Study of the effects of local and regional cultural noise on ground sensors at SGB has recently been undertaken to help filter these sources from the dense array dataset.

Within the SGB dense array, two (2) zones of amplification were reported by Ben-Zion et al. (2015) and later refined by Qin et al. (2017). Over the 4 weeks of recording, amplified seismic energy is observed in both the northeast and southwest regions of the site. The latter area has been explained as local basin effects and/or cultural noise associated with local land owners. The former, northeast portion of SGB, is interpreted as a seismic trapping structure; a zone reducing seismic wave velocities thereby amplifying motions at the ground surface (Figure 2-1).

2.2.2 Velocity Model Local Calibration and Earthquake Detection from the SGB Dense Array

As part of the 2014 array deployment, thirty-three (33) Betsy gunshots were fired at selected nodal locations. Betsy gunshots are a method of generating seismic energy at the surface, communicated through the substrate, and recorded by geophone nodes within the grid. Time intervals between energy sources and individual nodal locations provide a local velocity model used to characterize the geophysical properties of the fault zone (Meng and Ben-Zion, 2017). Using the velocity model, Meng and Ben-Zion (2017), developed a methodology for detecting a greater number of small events through the dense array which are not included in the standard earthquake catalog. Their technique, originally developed for underwater acoustics, adopts a method of beamforming and back projection of moving time windows to detect and locate energy sources. Applying this method to data recorded on 2014 Julian day 146, resulted in 723 potential detections, 220 of which were determined local energy sources. 103 of these events were validated as earthquakes from regional seismic recording stations, and the remaining 117 are considered earthquakes too small to detect within the regional network.

2.2.3 Internal Fault Zone Structure and Trapped Waves

In addition to earthquake detection, the dense array at SGB enables fine scale imaging of fault zone seismic structure (Qin et al., 2017). Using data from both dense and linear arrays within the basin, Qin et al. (2017) searched for waveform changes, and analyzed for P wave delay times as well as S and P FZTW (trapping structure from Ben-Zion et al., 2015, described above; Figure 2-1). Observation of waveforms from multiple

events recorded across the entire SGB array display a clear change in phases across a discrete set of sensor nodal columns coincident with a mapped trace of the SJFZ (Figure 2-1). Based on the observed phase change, Qin et al. (2017) concluded that the lineament outlined by the discrete columns represents a bi-material interface between different crustal blocks, and is the main seismogenic structure (at depth) of the local fault zone.

To characterize the velocity structure from the SGB array, Qin et al. (2017) evaluated P wave arrival times from nine (9) teleseismic events. By analyzing data from both the dense and linear arrays, a gradual decrease in delay times is observed SW of the fault indicating a local reversal in the velocity structure. To evaluate the structure in more detail, the dataset was processed for slowness (the ratio of observed P-wave travel time and the along-path distance). Similar to patterns in the delay times analysis, a marked decrease in slowness, from both dense and linear arrays, is observed SW of the fault confirming the velocity structure reversal.

To explain the anomalous area NE of the fault forcing the observed slowing of waveforms recorded within the array, Qin et al. (2017) performed analysis for FZTW. FZTW occur as seismic waves travel through a fault zone, following both P and S body waves, referred to as P-type and S-type FZTW respectively, and have relatively high amplitude and low frequencies. At SGB, FZTW were detected using an automatic algorithm for P-type, in order to observe and model S-type FZTW. Results of the analysis show regular occurrence of P- and S-types FZTW, localized in a zone NE of the Clark fault (Figure 2-1).

2.2.4 3-D Shear Wave Velocity Model from Ambient Noise Imaging

The dense array data collected at SGB allows detailed analysis of waveforms, as described above. These include large sets of longer bursts normally grouped as ambient seismic noise, which through extraction and inversion are used for high resolution tomographic imaging (Mordet et al., 2018). Using a double beamforming phase extraction technique (Roux et al., 2016), Mordet et al. (2018) isolated and extracted Rayleigh waves, or earthquake generated surface waves, in wavelengths characterizing shallow crustal depths between 50 and 500–700 m. These data are further processed in a Monte Carlo simulation using a Neighborhood Algorithm, producing a three-dimensional shear wave velocity (3D-Vs) model based on the average of 110 best models. The reader is referred to Mordet et al. (2018) for a detailed description of the model development.

Results of the 3D-Vs model indicate strong lateral variability across the array dataset at all depths. Similarities between findings from both the Mordet et al. (2018) model and Qin et al. (2017) results include low velocity zones in the NE and SW portions of SGB and strong contrasts delineating a boundary at depth below the western most trace of the CF. Authors of the 3D-Vs model attribute the sharp velocity contrast (Vs = 850 m/s) as the transitional boundary between loose surficial deposits and the crystalline basement rock. This boundary produces a fault parallel velocity high at depth bordered by low velocity troughs to the NE and SW, explained as local effects from the fault damage zone and a deep sedimentary basin, respectively. Based on both the inversion depth uncertainties, and final misfit, Mordet et al. (2018) note the deeper trough (SW low velocity zone) should be interpreted with caution.

2.3 Methods

The high quality and fine spatial scale of the seismological imaging at SGB is at a scale at which detailed geological observations and interpretations can be made and the opportunity was thus presented to advance the geologic models of the SGB site to a similar level of detail. Therefore, the methods adopted for this study included surficial geologic mapping of SGB and surrounding areas using both desktop (computer based) and field methods, and analysis of high resolution topography. Field geologic and structural mapping were recorded using Midland Valley's mobile applications Field Move and Field Move Clino. Topographic basemaps included bare earth digital terrain models (DTM) and hillshade models derived from both B4 lidar (Bevis et al., 2005) and small unmanned aircraft system (sUAS) based structure from motion (SFM) digital elevation models (DEM) (e.g. Johnson et al., 2014). The latter were also produced at fault outcrops for structural measurements and three-dimensional detailed mapping not possible using traditional plan view topographic maps (Bemis et al., 2014). Thick vegetation obstacles were challenging not only for making observations in the field, but also in using high resolution SFM DEMs for topographic analysis. Field mapping and structural measurements were recorded using a traditional paper map and Brunton compass, but primarily using tablet and smart phone devices with the mobile applications described above. All field data were compiled into the software package Move^{TM,} produced by Midland Valley, for structural analyses and cross section interpretation, and ArcGIS Pro for map integration/composite and establishing a geodatabase. Topographic/geomorphic and displacement analyses were performed using the B4 lidar

DTM in Matlab using Topotoolbox (Schwanghart, 2014): and LiDaCaoz 2.1 (Haddon et al., 2016) respectively. Cross-sectional depth slice images of the shear wave velocity model developed from the dense array (Mordet et al., 2018) were produced in Matlab, and imported into Move for comparison and interpretation with surficial mapping. General observations of shear wave velocity images are described in Section 2.10.

2.4 SGB Site Morphology

The SGB array is situated within a small basin (Figures 2-2 and 2-3) flanked by northwest-southeast trending ridgelines. Salisbury et al. (2012) termed this section of the fault "Burnt Valley" after the broader valley located just beyond the northern most ridgeline at SGB (Figure 2-2). Much of the terrain within Burnt Valley and surrounding hilltops support dense vegetative cover which include manzanita, oak, sagebrush, yuccas, tall grasses and pinyon pines. SGB was chosen for the dense array deployment due to its vicinity to the CF as well as the low relief within the small basin and favorable landowners. Broadly speaking, the morphology of the basin consists of a northwest-southeast long axis with asymmetrical flanking sides of long and arcuate vs short and linear, NE and SW slopes, respectively. The topography of the basin's floor generally slopes inward draining southeast into Alkali Wash. A pronounced linear ridge rises above the basin floor and plunges towards the NW (Figure 2-3). NW of SGB, the basin gradually narrows as the gently sloping western flank coalesces with the east ridge at Burnt Valley Road. The southern boundary of the small basin narrows to a small southeast ephemeral stream (Alkali Wash) responsible for draining most of the SGB site as well as draws (gullies) sourced in the adjacent slopes.

Similar to the SGB basin, Alkali Wash is oriented northwest-southeast with asymmetric flanking slopes. These slopes, particularly on NE side of the wash, consist of a series of pronounced draws and spurs, contrasting the subdued gentle slopes to the south. The orientation of the draws and spurs often show asymmetric properties as well, as the majority of the draws in the NE side consistently showing a NW deflection, interpreted as the fault trace (discussed further in section 2.6). Figure 2-3a depicts the hillshade of a digital terrain model (DTM) from B4 lidar data and the traces of fourteen topographic profiles. Profile 1 is drawn across the middle portion of the SGB basin to illustrate topography from SW to NE (Figure 2-3b). Profile 1 is slightly asymmetric, with a longer slope on the SW flank. Topography perpendicular to gullies incised into the flanking SW and NE slopes are shown in profiles 2 and 4, and 3 and 5, respectively (Figure2-3c). Profiles 3 and 5, show relatively low frequency incision and a smoother surface, contrasted against the rugged surface and high frequency incision observed in 2 and 4. Even and odd number profiles 6 through 14 illustrate longitudinal topography of selected spurs formed along the SW and NE slopes leading into Alkali Wash respectively (Figure 2-3d). Consistent, albeit subtle, asymmetric gradients with steeper slopes are observed on spurs to NE.

2.5 SGB Geologic Mapping

Geologic maps of the SGB vicinity are principally at 1:24,000 scale and were compiled using topographic contour base maps (Sharp, 1967). The accuracy and detail of these maps are exceptional given the scales of presentation, yet, one question raised in this study includes: is there more we can learn about geology and structure in the study

area using new technology, notably high resolution topography? DEMs derived from lidar and SFM provide higher detailed topographic data in shorter collection times than traditional manual survey techniques. Removal of vegetation and cultural features (DTMs) allow the observer improved visibility of offset geomorphic features used for tracing fault strands, and landforms. SFM data provides the additional utility of mapping in orientations other than traditional horizontal map view. For this analysis, these techniques were employed to capture the spatial distribution of surficial geologic units (described in the following subsections), fault surface traces (section 2.5), and rock damage (section 2.7). Figure 2-4 displays a geologic map, produced as part of this study, and includes key locations discussed within following subsections. An ANSI C-sized sheet (17 in. x 22 in.) version of the geologic map is provided in the supplemental material.

2.5.1 Rock units

Within and surrounding the SGB basin are two primary crystalline rock types: high grade metamorphic and younger plutonic. At SGB, Sharp (1967) termed these metamorphic and plutonic rocks the Burnt Valley Complex (BVC) and Coahuila Valley Pluton (CVP) respectively. Although not directly observed within the SGB study area, outcrops of the Horse Canyon Pluton (HCP) underlie Bautista sediments south of Burnt Valley (Sharp, 1967). Based on stratigraphic evidence in the western portion of the Peninsular Ranges, Sharp (1967) gave an approximate age of middle Cretaceous to plutonic rocks surrounding the SJFZ. Potassium-Argon ages of the batholith, range from 120 Ma to 70 Ma (Krummenacher et al., 1975). Subsequent thermochronology constrain

the intrusion ages to 99-97 Ma (Miggins et al., 2014). The following subsections provide descriptions from field observations of the mapped rock units.

2.5.1.1 Metamorphic Rocks of the Burnt Valley Complex

Within SGB and Alkali Wash, BVC includes high grade metamorphic rocks of banded gneiss and migmatite, and have been described as pre-middle Cretaceous in age (Sharp, 1967). Discerning the metamorphic fabric is somewhat difficult due to secondary brittle deformation and poor exposure due to weathering and vegetative cover. However, 1 to 2 m diameter float observed within drainages and the main channel of Alkali Wash shows strong foliations and shear bands (Figure 2-5a). Locally, the banded gneiss is fine-grained with roughly equal parts mafic and felsic minerals, but varies compositionally in mica content. Leucocratic dikes and sills are common within the BVC, and appear compositionally as a fine-grained mode of the adjacent plutonic rock. Dikes and sills range in thickness from cm to tens of meters (Figure 2-5d).

2.5.1.2 Plutonic Rocks of the Coahuila Pluton (CVP)

Rocks of the Cretaceous CVP (Sharp, 1967) are observed exclusively on the SW side of the SJFZ. At SGB, these rocks are primarily medium-grained, phaneritic, hornblende, biotite tonalite. Exposure of the CVP within the SGB basin is limited to the local land owner's road cut. The rock mass is highly weathered with only fresh indurated core-stones (Figure 2-5c). As the weathered material erodes downslope, boulders are often translated downslope as observed within and on the SW flanking slopes of Alkali Wash (Figure 2-5d). Pegmatite dikes are observed in outcrops on the SW slopes of both

the SGB basin and Alkali Wash. Within several meters of the contact with the BVC, the long axis of darker mineral grains in the tonalite have a similar NNW-SSE orientation as the metamorphic foliation.

2.5.1.3 Quaternary Bautista Beds

Sharp (1967) mapped a thick deposit of poorly consolidated sediments, termed the Bautista beds, overlying the basement plutonic and metamorphic rocks in the Peninsular Range. The deposit fills the majority of the topographic lows within the range including Burnt Valley, and were initially dated as Pleistocene in age based on vertebrate fossils (Frick, 1921). The deposits, as described by Sharp (1967), range in coarseness from boulder gravel to silt and clay beds, having accumulated through fluvial and lacustrine processes within the intermontane basins. The mapping unit, Bautista beds, was applied to all poorly consolidated Quaternary sediments mapped in vicinity of the SJFZ in the Peninsular Range (Sharp, 1967).

2.5.2 Quaternary Landforms and Deposits

Sedimentary deposits and associated landforms developed within the SGB basin are alluvium and colluvium eroded from the surrounding slopes. Within the main basin floor, these deposits consist of dark grayish brown sand and silt with gravels, cobbles and boulders generally fining towards the basin interior. At the southern end of the basin, one and two stream channels are incised into the hillslopes and alluvium from the east and west flanks of the basin, respectively, and feed the main drainage into Alkali Wash. At the surface, these channels are filled with loose coarse sand, gravels and cobbles and occasional boulders.

Located on the lateral extents of Burnt Valley are thick deposits of massive to weakly bedded sands and gravels (Figure 2-6). Opposite the NE ridge of SGB, within Burnt Valley, the topography is incised by numerous drainages that flow into and across the valley floor. Exposed within the drainages are roughly 10 m high remnants of deposits of fine to medium grained light yellowish-brown to orangish-brown sand, capped by gravels in some locations (Figure 2-6a). Similar deposits are found on the NW and SE side of Burnt Valley Road (Figure 2-6 b and 2-7). A small outcrop of fine to medium sands and gravels are also observed in between Burnt Valley Road and the SGB basin (Figure 2-6c).

Within Alkali Wash are two generations of deposits; 1) the modern stream channel which is covered with a mixture of gravels, cobbles and boulders, and 2) an older coarsening upwards sequence of sands and gravels with remnants that stand over 20 m above the modern channel (Figure 2-6d). Older sedimentary materials in the wash are similar in clast lithology and size as those observed in road cut in the Burnt Valley Road roughly 2 km north the SGB basin (Figures 2-3a and 3). Larger boulders, almost exclusively tonalite, ranging up to 2 meters in diameter are strewn across the southwestern slopes, create knickpoints within the wash channel and to lesser extent rest upon the lower edge of the northeastern slopes.

2.6 SGB Fault Nomenclature and Surface Trace

At large mapping scale, the CF appears as a single, relatively simple and straight structure (Figures 1-1 and 1-3), however, at smaller scales the fault consists of multiple curved strands (Figure 2-8). Discussed in the following paragraphs are previous fault

trace mapping, revisions to fault traces using high resolution topography, and fault identification nomenclature and fault parameters adopted for the three dimensional model discussed in section 2.10.

2.6.1 Previous Fault Mapping

Previous mapping of the CF through SGB by Sharp (1967) shows multiple strands within vicinity of SGB; these include a west-dipping thrust fault juxtaposing metamorphic rock over the Bautista beds, a ridge bounding fault with SW side down vertical displacement on the northern edge of SGB, and three NW trending faults within the basin (Figure 1- 6). At the head of Alkali Wash, Sharp mapped the faults merging into a single strand which juxtaposes the Coahuila Valley Pluton (CVP) against the Burnt Valley Complex (BVC) metamorphic rock, evolving into a second SW dipping thrust fault farther to the SW.

2.6.2 Fault Trace Mapping Using High Resolution Topography and Focused Field Work

Previous mapping of the CF described in the paragraph above is based on coarse scale topographic contour maps and 1:24,000 scale geologic mapping. Surface trace mapping of the CF for this study uses a high resolution (0.25–0.5 m) DTM and hillshade, which allows for identification of topographic lineaments and offset geomorphic features (Figure 2-8). Individual fault traces are assigned a numerical identifier (ID) to help guide fault descriptions within this section, and are used as parameters for the 3D fault model (discussed in Section 2.10). Fault traces illustrated in figure 2-8 are based on the following; 1) topographic lineaments, 2) breaks in slope, 3) displaced landforms, and 4) offset geologic units observed primarily in the field. Faults labeled 100 - 109, and 200

through 206 are considered most recent, or active within the Holocene, and Quaternary active (no sense of Holocene activity), respectively. Described from NW to SE, faults presented in figure 2-8 are summarized in the text below beginning at Burnt Valley road.

Faults F100 and F102 are both observed as strong NW-SE trending lineaments within the DTM. Salisbury et al. (2012) measured six offset drainages along fault 102 SW of Burnt Valley road. The road cut is oblique to the fault trace and contains a roughly 60 m section with multiple fault planes bisecting the BVC and a consolidated gravel bed of the Bautista (Figure 2-7). A small failure of the road cut slope exposes a free face of the eastern most plane (Figure 2-7d). Between the eastern and western most extents, the fault juxtaposes cemented Bautista gravels against BVC. Both faults (F100 and F102) trend parallel along a linear ridge before diverging from one another roughly 840 m SW of the road cut. There, F100 offsets the linear ridge approximately 400 m to the SE and terminates. Along strike to the SE, F102 is mapped at the base of the ridgeline and the northeastern boundary of the SGB basin. F102 appears to terminate, or merge into faults F104 and F106, near the main channel stem that drains SGB into Alkali Wash.

Located at the northwestern margin of the SGB basin, a large outcrop of BVC protrudes from the valley floor with multiple NW-SE trending lineaments labeled F101, F103 and F104. The higher ground surface is covered by thick vegetation making direct observations difficult, however, at the NE edge of the outcrop, F104 displaces a small drainage by approximately 3 meters (Salisbury et al., 2012). Following F104 SW along strike, the fault splits along a shutter ridge that extends roughly one-half to two-thirds of the E-W width of the basin. On the NE side of the wash, F104 is easily traced using

multiple small shutter ridges with dextral offset. At the edge of the mapping area, F104 is observed in the DTM deflecting a small SW draining channel, and in the field juxtaposing young colluvium against the metamorphic rock (Figure 2-8d). Fault F106 is mapped along SW boundary of the long linear ridge extending into SGB. F108 is drawn as an inferred fault based on a small stream channel deflection to the SW of the offset gap in F106, and topographic lineaments channel meanders at the head of Alkali Wash. At the latter location, F106 and F108 are mapped as single strand where in the field, the fault was located within a terrace juxtaposing BVC and CVP (Figure 2-4). Surface trace of F110, within a large SW flowing drainage into Alkali Wash, is slightly obscure with a small dextral deflection in the channel thalweg, but in the field is roughly coincident with intense fracturing/brecciation of the rock mass. Detailed descriptions of displacement measurements and fault zone rock damage observed during this study are provided in sections 2.6 and 2.8 respectively. Faults F103, F105, F107 and F109 were not observed in the field, but appear as sharp lineaments/topographic features in the DTM and topographic profiles (Figure 2-3).

Faults F202, F204, F206, and F208 are thrust faults with poor to no expression in the topography. F202 is a SW dipping thrust fault originally mapped by Sharp (1967), juxtaposing BVC over Bautista sediments within Burnt Valley and near the head of Horse Canyon. Best exposure of this fault is near the Pacific Crest Trail, within a deep erosional cut on the NE side of the ridge opposite Alkali Wash. An outcrop of the thrust fault is also found within a small NE flowing drainage within Burnt Valley (Figure 2-8). F204, F206 and F208 are discontinuous east-dipping thrust faults, observed primarily as

low dipping fault planes offsetting and/or brecciating internal structures within the metamorphic fabric.

2.7 SGB Fault Displacement

Displacement from the most recent large surface rupturing earthquake, within or near Anza, produced an average 2.5–2.9 m of right-lateral slip, possibly during the large earthquake on 22 November, 1800 (Salisbury et al., 2012). The Burnt Valley section measurements collected by Salisbury et al. (2012) are primarily field based on faults F102 and the northern extreme of F104. For this study, displacement along the fault traces within SGB and Alkali Wash were measured from B4 lidar DTM using the Matlab application LaDiCaoz 2.1 (Zielke et al., 2015; Haddon et al., 2016) (Figures 2-9 and 2-10) to better characterize the recent offset along each structure. All displacements measured for this study and discussed in the text below are based on dextral stream channel offsets in SGB and Alkali Wash; value, fault trace, and location information of each offset are listed in table 2, and illustrated in figure 2-9. Detail images of measured displacement from LaDiCaoz are found in figure 2-10. We followed standard procedures for measurement and quality assessment as discussed by Zielke et al., 2015 and Salisbury, et al., 2015.

Only the main elements including fault ID, displacement feature and location, are discussed within this paragraph. Estimation of slip distribution for the faults within SGB are found in the Section 3.1.2. Fault trace F102 represents the NE border of the SGB basin, bounding a NW-SE trending linear ridge. Gullies developed within the ridge's eastern slope are shallow with little to no channel development impeding fault horizontal

displacement evaluation (Figure 2-8). Only one location, SCO-02b, near the southern end of the SGB basin, is coincident with a 15 m channel deflection and the mapped fault trace (Figures 2-9 and 2-10). Farther downstream, the channel is offset approximately 16 m at SC-02a along F104. Approximately 150 m along strike to the SE along F104, ~3.4 m of dextral displacement is measured at SCO-06. Along F106, displacement measurements include 12.3 m, 16 m, and 3.1 m at locations SCO-01, SCO-03, and SC-04, respectively. Fault F108 is primarily mapped from lineaments at the head of Alkali Wash, however, at location SCO-07, a small stream measures 2.8 m of dextral offset. Finally, fault F110, near the source of larger drainage feeding into Alkali Wash, and roughly coincident with a zone of intense rock damage (discussed further in Section 2.8, displaces the channel 3.4 m at location SCO-05).

2.8 Observations from Site Excavation

Despite strong surface expression of fault scarps within SGB, alluvial fill and channel deposits covering the valley floor obscure direct observation of fault zone damage. To expose a cross-sectional view of the fault zone and underlying rock units, a roughly 50 m long by 1.4 m deep trench was excavated across the prominent NW-SE trending ridgeline transecting the northern portion of the basin (Figure 2-11). The excavation location was chosen based on three elements; 1) distinct fault scarps along a fault parallel ridgeline, 2) previous geologic mapping indicating metamorphic rock composition of the ridgeline (bounded by Quaternary units), and 3) clearance from vegetation and cultural features. Figure 2-11 includes the surface fault trace mapping of SGB and location of the excavation, and includes a sUAS SFM digital surface model

(DSM) hillshade collected to record the excavation extent with reference to mapped faults. The southern trench wall was cleaned and photographed to create an orthomosaic for logging using methods prescribed by Gray et al. (2016) (Figures 2-12 through 2-15). Soil units were described using the unified soil classification system (ASTM, 2006) (Table3). The subsections below provide detail descriptions of observations made within the SGB excavation.

2.8.1 Trench rock units

Units observed within the SGB excavation are classified into two main groups based on texture; chiefly grain size and consolidation. Generally, these 2 units consist of consolidated stiff clast-rich material, and loose dark brown fine grained deposits, units 200 through 205, and 100 through 103, respectively (Table 3 and Figures 2-12 through 2-15).

Units 100 through 103 include grayish brown sandy silts, clayey sands to sand with clay, contain abundant mica and quartz grains, and observed at the lateral extremes of the excavation. Units with higher sand concentrations have weak to no cementation and generally lack soil structure, while the more fine-grained soft material has a weakly developed platy structure. Units 101-1 and 101-2, on the SW and NE ends of the trench,in color and texture but differ in gravel and cobble concentrations and sizes, with larger values of each on the latter side of the trench.

The majority of the excavation consists of units 200 through 205; composed of angular to sub-angular cobble to boulder-rich deposits with no soil structure development. Clasts in units 200 through 205 are chiefly metamorphic rock, range in size

between 10 cm and 2 m, have chaotic orientations and are at various stages of weathering/disintegration. Larger boulders are generally intensely fractured to disintegrated with a well-developed chemical weathering rind. In general, larger clasts are more concentrated on the NE side of the excavation. Units 200 through 205 each have a variety of colors including dark orangish brown, grayish brown, greenish gray, and dark gray. Units with cohesive matrix include stiff medium plasticity clays.

2.8.2 Excavation Geologic Structures

Based on Sharp's (1967) mapping and initial observations at SGB, the substrate of the fault scarp and ridgeline were anticipated to be metamorphic rock of BVC. The purpose of the excavation was to expose fault zone structure preserved in the rock mass of fault F104 and F106 as well gradational variations in damage between the traces.

Unexpectedly, the near surface stratigraphy within the excavation, lacks the metamorphic rock mass as previously mapped (Sharp, 1967). The fault surfaces within the vicinity of F106, in the excavation, are interpreted based on a thin vertical fracture penetrating units 201 and 202, and a sub-vertical oriented long flat boulder clast (Figures 2-13 and 2-14). In contrast, the excavation exposed much more developed zones of structural planes below mapped trace F104. These include five zones, labeled A through E, primarily defined by thin light gray to orangish brown clayey zones that dip between 50° and 70° toward the NE (Figure 2-12). Between the shear planes are elongated clasts of intensely fractured, brecciated, and pulverized metamorphic rock.

Depth to bedrock was deeper than expected in the excavation (none was encountered), and the exposed material lacked the strength to preserve the greater fault

structure initially anticipated. However, the material encountered was beneficial to the overall understanding of the basin stratigraphy and indicates material translation along the main fault planes within SGB. Interpretation of these features with greater context of fault zone structure are expanded upon in the Section 3.1.1.

2.9 Rock Damage Survey and Transects

To assess the extent of rock damage within SGB and help validate observations of FZTW in the dense array (Qin et al., 2017), outcrops within the study area were classified for damage characteristics and intensity using definitions from Dor et al. (2006) (Table 5) (Figure 2-15). These qualitative ratings are relatively straightforward to make in the field. We worked to make many and maintain consistency among a few different observers. Within the surveyed extent, rock damage ranges from weak fracturing (class 1) to weak/selective pulverization (class 4) (Table 5). Survey points color coded by damage class are depicted in Figures 2-15 to 2-18.

Rock exposure within the SGB basin is limited to the NE and SW slopes. These surfaces however, are often covered by colluvium, saprolite, and vegetation. On the SW slope, a road-cut leading into the basin provides some exposure. Outcrops on the SW are generally low in observed damage, with fracture spacing greater than 10 cm. Much of the NE slope is covered by thick brush and trees, which limit the survey to gully exposures and occasional fresh rock faces found near the base of drainages. These exposures reveal large variations in damage intensity from trace fracturing to pulverization. Zones of pulverized rock in the NE slope are generally white, light gray and yellowish to orangish brown, loose, and fine grained (sand to silt sized particles) material.

Although rock damage observations within the SGB basin are relatively asymmetric, the lack of continuous exposure, particularly across the sediment covered basin floor, hinders that assessment's spatial coverage. To supplement this characterization, the survey was extended south of SGB into Alkali Wash (Figures 2-15 through 2-17) where there is significantly better exposure. The main channel of the wash is generally covered by recent deposits, offering few rock exposures, however, drainages incised into the NE and SW slopes allow for additional damage assessment and structural characterization. As described in section 2.3, the NE and SW slopes of Alkali Wash are asymmetric with more incision observed in the former. The best exposure of fresh rock, within the drainages, is generally restricted to the base of deeply cut channels. Figure 2-15 provides example images of each rock damage class observed during the survey, an overview map of all the survey points color coded by damage classification, and the location of transects 1 through 4 in Alkali Wash. The transects included four drainages incised into the NE and SW slopes; 2 transects on each side of the wash. The transects provide the best opportunity make observations across the fault zone to assess the extent and intensity of rock damage. Figures 2-16 and 2-17 include mapped geology, structural measurements, and rock damage classification survey points of transects 1 and 2, and 3 and 4, described in the following subsections.

2.9.1 Transect 1

Within a large tributary drainage on the NW slope of Alkali Wash, Transect 1 spans three mapped fault strands (F106/F108, F104, and F110) and the two major rock units (CVP and BVC) (Figures 2-15 and 2-16). At the start of the transect within the main

channel of Alkali Wash, there is little exposure of rock damage, but metamorphic rock observed farther downstream consists of partially pulverized rock on the NE side of F106 (Figure 2-16). The initial ~100 m of Transect 1 is within sedimentary deposits of sand, silt, gravels and cobbles. These are juxtaposed against a metamorphic outcrop and a deflected/shutter ridge along F106. Damage at the juxtaposition appears primarily as brecciated rock, but transitions to more pulverized material immediately to the NE. From 100 and roughly 130 m of Transect 1, the rock mass is covered by a veneer of colluvium, and terrace deposits obscuring damage assessment. Between 130 m and F110 the main channel of the drainage has incised between 1 and 2 m providing good exposure. This stretch of the transect includes banded gneiss of the BVC, and numerous faults ranging between 10 cm and 50 cm wide, dipping primarily towards the SW to sub-vertical, which cut across the metamorphic fabric. Damage within the rock volume ranges from weak widely spaced fractures to intense fracturing. The location of F110 is demarcated by a roughly 1.5 to 2 meter knickpoint and adjacent boundary with a >100 m thick leucocratic dike (BVC-t). The initial ~50 m of BVC-t along Transect 1 ranges in damage from fragmentation (class II) to partial pulverization (class IV). Surveying of damage within the upper portion of the transect proved difficult due to steep terrain, but generally indicated lower damage intensity.

2.9.2 Transect 2

Transect 2 (Figure 2-16) includes observations up slope of the main Alkali Wash drainage and a portion of the Pacific Crest Trail on the SE slope. The transect does not directly cross any fault trace, but includes observation points adjacent to F106 entirely

within the tonalite of CVP. Observations of Kt in transect 2 are consistent with those on the SW slopes of SGB exposing relatively indurated corestones surrounded by a loose weathered matrix. Discerning damage class within the tonalite (CVP) along transect 2 is somewhat ambiguous as the exposures are highly weathered. The loose material contains granules of intact mineral grains and do not resemble the powdery, fine grained texture of pulverization. Survey points are based on exposed corestones within the weathered matrix. Exposures at the base of the drainage and within Alkali Wash contain no core stones and are classified as class 3. Exposures near the start of the transect on SW side of the wash appear primarily as class 2. Corestones in the remainder of the transect range from class 2 to 1.

2.9.3 Transect 3

Transect 3 (Figure 2-17) spans a complex set of structures that include the NE dipping thrust fault (F206) that appears offset along F105. Between and adjacent to the faults, damage intensity ranges from class 2 to 4. From approximately 100 m upstream along transect 3, damage intensity gradually decreases, before outcrops reveal sharp increases near the end of the traverse. Rock exposure quickly fades at the top of the ridge due to thick brush and trees. Within the drainage of transect 3 exposure is relatively poor due to a lack of incision, soil and regolith cover, and vegetation within and surrounding the channel.

2.9.4 Transect 4

Transect 4 (Figure 2-17) traverses the gentle gradient of a drainage on the SW slope spanning both CVP and BVC/BVC-t. Damage class values are low within the main

channel of Wash, and increase to class 2 near the mapped main fault trace of the SJFZ from Sharp (1967) and the USGS (2006) (queried fault trace in this study) (figure 2-17). Exposure is relatively poor upstream of approximately 50 m along transect 4. Near the contact between the CVP and BVC the damage class 3 and gradually decreases to class 1 near the end of the transect.

In summary, the transects provide a first order observation of damage distribution across the mapped fault traces spanning the two main rock units (BVC and CVP). These observations depict asymmetric properties, with more damage intensity concentrated on the NE side of the main fault trace. Transects 1 and 3, on the NE side of the Alkali Wash, also contain more structures/mapped fault traces in contrast with Transects 2 and 4.

2.10 Geologic Model of Fault Zone Structure

Analysis of the CF internal fault zone structure using seismic wave data recorded in the dense array indicates that the main seismogenic fault is coincident with the southwestern most fault trace, and define a trapping structure located on the NE side of the basin (Qin et al., 2017). The 3D-Vs model developed by Mordre et al. (2018) illustrates the heterogeneity and complexity of the shallow subsurface below the SGB basin, and a low velocity section below the fault zone and trapping structure. To accomplish the task of building a geologic model and help validate these geophysical findings, two sets of cross sections were constructed. The transect line of each cross-section is drawn over the geologic map in figure 2-18. The first set of cross sections is based solely on the data collected from surface observations, and the second set is guided

by both geologic mapping and depth slices of the 3D-Vs dataset (Figures 2-19 through 2-24).

2.10.1 Geologic Model from Structural Measurements in Alkali Wash

Structural elements, recorded mainly in BVC, include foliations, thin faults (>0.5 m thick) and fractured rock. In Transect 1, between the intensely fractured rock of BVC-t and fault trace F104, the foliation is primarily sub-vertical possibly folded, and cut by two sets of faults; one shallow and one steeply dipping. Above BVC-t, the foliation fabric exhibits a gentle dip towards the NE, roughly parallel to fault trace F204. In Transect 3, the fabric has variable geometry, and thin faults occur exclusively at low angles. Opposite the NE ridge of Alkali Wash, within Burnt Valley, BVC is juxtaposed over the Bautista sediments along fault F202. Although not directly observed within the study area, south of Burnt Valley, the Horse Canyon Pluton (HCP) underlies the Bautista. For this geologic model, HCP is interpreted directly underlying the Bautista, and juxtaposed against BVC. The geometry of the fault at the surface is constrained by measurements within Burnt Valley.

2.10.2 Geologic Model from 3D Vs Data and geologic map data at SGB

Using the 3D-Vs model developed by Mordret et al. (2018), twenty-one vertical depth slices were generated at equal intervals, normal to the mapped average orientation of the fault traces at SGB. The depth slices were given a numerical ‘line’ identifier listed sequentially from SE to NW. Four slices were selected, (Lines 05, 10, 15 and 20) for integration and geologic interpretation with site mapping (Figures 2-21 through 2-24). Two sets of each 3D-Vs (Mordret et al., 2018) slice were produced to illustrate 1) the

upper 100 m and 2) lower 300 to 700 m depth interval. Common features amongst all four lines in the deeper interval include: 1) apparent highest velocity values occur between depths of 200 to 400 m which extend to the bottom of the domain; and 2) apparent low velocity "troughs' observed in 2 to 3 locations within each depth slice (Figures 2-21b through 2-24b). The troughs are located on the SW, within the NE half (middle trough) and extreme NE of the dataset. The SW trough forms a relatively long thin tabular body extending to a depth of roughly 600 m, while the middle trough expresses a wedge shape with a slightly elongated NE side which transitions to an apparent higher velocity between 350 m and 500 m depths. The trough to the NE is most pronounced in Line 05 (Figure 2-21) and appears either removed towards the NW (Lines 10 through 20) or perhaps merging with the middle trough.

Vs depth slices of the upper 100 m are displayed with velocity values between 300 and 600 m/s, to better show contrast in the lower velocity material in the shallow subsurface (Figures 2-21c though 2-24c). In general, the apparent lowest velocity is visible within the upper 10 m, with no sharp discontinuities. Lines 5 through 15 show a thick transitional zone between roughly 10 m and 90 m. Line 20 shows a similar transition, with an NE down dip surface.

An additional tool to assist in visualizing discontinuities within Vs data involved calculating the numerical gradient. The numerical gradient estimates the partial derivatives in the x and y direction using known values at certain points. For a function of two variables, F(x,y):

$$F(x,y) = \frac{\partial F}{\partial x} i + \frac{\partial F}{\partial y} j$$

Part d of figures 2-22 through 2-25 shows a color map illustrating the gradient of the depth slice down to 700 m depth. The gradient plot also helps provide confidence to geologic interpretations based the strength of the discontinuity. Changes observed in the gradient plot appear consistent with the Vs depth slice plots, and depict no to relatively subtle changes between the upper 200 m, and a gradual transition between roughly 350 m to 500 m. By far the strongest contrast in velocity is observed adjacent to the SW low velocity trough of the Vs depth slices.

Geologic interpretations of Lines 05 through 20 are a synthesis of both the surficial mapping, and geophysical data. Part a, of figures 2-21 through 2-24, depict the geologic model of the SGB basin. The highest velocity values, observed consistently across each Vs depth slice are sensibly the plutonic rock. The middle low velocity trough is coincident the three mapped fault traces F102, F104 and F106. The gradient map indicates a lack of significant velocity contrast on either side of the middle trough suggesting that in the upper few hundred meters, the fault does not juxtapose significantly contrasting material. The "V" shaped taper of the middle trough implies the fault zone structure narrows, most likely merging into a single structure at depth. Also persistent within each Vs depth slice, the middle low velocity trough has an asymmetric form, with lower velocity values extending deeper on the NE side, interpreted as the overall dip of the fault zone structure.

The second constant, and most pronounced trough appears in the SW end of the Vs-depth slice. The feature extends to almost the entire depth range of the dataset; however, Mordret et al (2018) cautioned on the interpretation of this trough based on the

misfit and uncertainty of the model there. In vicinity to Line 10 is the borehole location for B946 which involved the installation of a strain meter as part of the Plate Boundary Observatory (UNAVCO, 2010). The borehole is roughly coincident with the SW trough, encountering fractured rock and clayey material at depths between 400 ft and 500 ft. Cuttings from the borehole were described entirely as granitic, corresponding to the tonalite rock of CVP. On the basis of these data, the large discontinuity in the SW portion of the data is interpreted as a sub-vertical fault within the CVP.

A third low velocity trough, best defined in Line 5 in the extreme NE of the Vs dataset (Figure 2-21), possibly merging with the middle trough in the subsequent Vs depth slices. The gradient plot does indicate a contrast in velocity within the area of the second trough in Line 5, but shows little change in Lines 10 through 20. In the geologic model, this feature is interpreted as fault F202 steepening to a vertical dip below the NE ridgeline of SGB.

2.11 Three Dimensional Model of the Clark Fault

Surface trace mapping described in section 2.6 builds from previous work (Sharp, 1967) using high resolution topography and field work. Structural attitudes collected from outcrops of the fault constrain the near surface geometry. In traditional structural geology, these attitudes are projected into the subsurface using two-dimensional (2D) cross-sections. Using Midland Valley's software package Move allows the geologist to produce the same product in three-dimensions. Building a 3D model of the fault zone structure based on surface observations is necessary for the task of validating shallow geophysical properties at dekameter scale.

2.11.1 Fault Model Parameters and Justification.

Producing the 3D fault model in Move requires individual line sources (fault traces) and geometric attributes, and can be input by two methods. The first requires digitizing the surface trace line and projecting the fault using a plunge, or dip angle, down dip into the subsurface. The second involves more traditional methods of creating multiple successive 2D cross sections along strike, manually drawing the fault geometry, and digitally connecting the fault by projecting a surface between sections. For this analysis, a combination of these methods was implemented (See supplemental material for 3D pdf version of the fault zone model). Mapped fault surface traces from this study were imported into Move as a shape file from the project GIS, and the fault plane projected into the subsurface using attributes and constraints from Table 6 (Figure 2-25)

The Burnt Valley Road cut exposure provides an opportune location to collect attitudes of faults F100 and F102 (Figure 2-7). Multiple measurements were made on three separate fault planes yielding a mean dip of 77° towards the SW. The low angle failure planes observed in the excavation below F104 most likely are not representative of the fault at depth. The exposure of F104 at the southern end of the map area is vertical, and is a preferential orientation given the strong and straight fault trace. Geometry of F106 is difficult to constrain with a lack of clear exposure of the fault plane. Within the trench, the fracture penetrating units 201 and 202 dips approximately 80° towards the NE (Figure 2-12). Given this sub-vertical value and strong strike-slip offset observed in landforms, this measurement is adopted for the model. The last fault used in the model includes F202; a SW dipping thrust fault. Sharp (1967) approximated the dip on this fault

at 37° in the vicinity of SGB. During the mapping campaign, fault planes in a similar vicinity were measured closer to 55° at two locations approximately 1 km apart (see oversized geologic map in supplemental material), and is the value used in the 3D model. The remaining faults found on the geologic map (Figure 2-4, and 2-8) either because of poor exposure (odd numbered faults F101 through F109) making fault geometry difficult to constrain, and/or short trace length (F204 and F206) are not included in the fault model and most likely secondary features, not seismogenic.

2.12 References

Aben, F.M., Doan, M.-., Gratier, J.-., and Renard, F., 2017, High strain rate deformation of porous sandstone and the asymmetry of earthquake damage in shallow fault zones: Earth and Planetary Science Letters, v. 463, p. 81-91.

Allam, A.A., Ben-Zion, Y., Kurzon, I., and Vernon, F., 2014, Seismic velocity structure in the Hot Springs and Trifurcation areas of the San Jacinto fault zone, California, from double-difference tomography: Geophysical Journal International, v. 198, p. 978-999.

Bemis, S.P., Micklethwaite, S., Turner, D., James, M.R., Akciz, S., Thiele, S.T., and Bangash, H.A., 2014, Ground-based and UAV-Based photogrammetry: A multi-scale, high-resolution mapping tool for structural geology and paleoseismology: Journal of Structural Geology, v. 69, p. 163-178.

Ben-Zion, Y., and Shi, Z., 2005, Dynamic rupture on a material interface with spontaneous generation of plastic strain in the bulk: Earth and Planetary Science Letters, v. 236, p. 486-496.

Ben-Zion, Y., Vernon, F.L., Ozakin, Y., Zigone, D., Ross, Z.E., Meng, H., White, M., Reyes, J., Hollis, D., and Barklage, M., 2015, Basic data features and results from a spatially dense seismic array on the San Jacinto fault zone: Geophysical Journal International, v. 202, p. 370-380.

Bevis, M., K. Hudnut, R. Sanchez, C. Toth, D. Grejner-Brzezinska, E. Kendrick, D. Caccamise, D. Raleigh, H. Zhou, S. Shan, (2005). The B4 project: Scanning the San Andreas and San Jacinto fault zones, Eos Trans. AGU 86, no. 52 (Fall Meet. Suppl.), H34B–01.

Chester, F., Evans, J.P., and Biegel, R., 1993, Internal Structure and Weakening Mechanism of the San Andreas Fault: Journal of Geophysical Research-Solid Earth, v. 98, p. 771-786.

Chester,F.M., Chester, J.S., Kirschner, D.L., Schulz, S.E., Evans, J.P., 2004, Structure of large-displacement, strike-slip fault zones in the brittle continental crust, *in Karner, G.D., et al.,* Rhyology and Deformation in the Lithosphere at Continental Margins: New York, Columbia University Press, p.223-260.

Dor, O., Rockwell, T., and Ben-Zion, Y., 2006, Geological Observations of Damage Asymmetry in the Structure of the San Jacinto, San Andreas and Punchbowl Faults in Southern California: A Possible Indicator for Preferred Rupture Propagation Direction: Pure and Applied Geophysics, v. 163, p. 301-349.

Frick, C., 1921, Extinct vertebrate faunas of the Badlands of Bautista Creek and San Timoteo Cañon, Southern California: Berkeley: University of California Press

Gray, B., Graehl, N., Bozkurt, S., Baldwin, J., and Clahan, K., 05/30, Seamless Photomosaic Trench Logging Using Trench-Based Photogrammetry Methods: Workflow and Case-Studies, *in* 7th International INQUA Meeting on Paleoseismology, Active Tectonics and Archeoseismology (PATA) Crestone, Colorado, p. 4.

Haddon, E. K., C. B. Amos, O. Zielke, A. S. Jayko, and R. Buergmann (2016), Surface Slip During the Large Owens Valley Earthquake, G-cubed.

Johnson, K., Nissen, E., Saripalli, S., Arrowsmith, J R., McGarey, P., Scharer, K., Williams, P., Blisniuk, K., 2014, Rapid mapping of ultra-fine fault zone topography with Structure from Motion, Geosphere, v. 10; no. 5; p. 1-18.

Krummenacher, D., Gastil, R., Bushee, J., and Doupont, J., 1975, K-Ar Apparent Ages, Peninsular Ranges Batholith, Southern California and Baja California: Bulletin of the Geological Society of America, v. 86, p. 760-768.

Meng, H., and Ben-Zion, Y., 2017, Detection of small earthquakes with dense array data: example from the San Jacinto fault zone, southern California: Geophysical Journal International, v. 212, p. 442-457.

Miggins, D.P., Premo, W.R., Snee, L.W., Yeoman, R., Naeser, N.D., Naeser, C.W., and Morton, D.M., 2014, Thermochronology of Cretaceous batholithic rocks in the northern Peninsular Ranges batholith, southern California: Implications for the Late Cretaceous tectonic evolution of southern California, in Morton, D.M. and Miller, F.K., eds., Peninsular Ranges Batholith, Baja California and Southern California: Geological Society of America.

Mitchell, T.M., Ben-Zion, Y., and Shimamoto, T., 2011, Pulverized fault rocks and damage asymmetry along the Arima-Takatsuki Tectonic Line, Japan: Earth and Planetary Science Letters, v. 308, p. 284-297.

Mordret, A., P. Roux, P. Boué and Y. Ben-Zion, 2018. Shallow 3-D structure of the San Jacinto Fault zone revealed from ambient noise imaging with a dense seismic array: Geophysical Journal International., in review

Morton, D.M., and Matti, J.C., 1993, Extension and contraction within an evolving divergent strike-slip fault complex: The San Andreas and San Jacinto fault zones at their convergence in Southern California, in Powell, R.E., et al., eds., The San Andreas fault system: Displacement, palinspastic reconstruction, and geologic evolution: Geological Society of America Memoir 178, p. 217–230.

Morton, N., Girty, G.H., and Rockwell, T.K., 2012, Fault zone architecture of the San Jacinto fault zone in Horse Canyon, southern California: A model for focused post-seismic fluid flow and heat transfer in the shallow crust: Earth and Planetary Science Letters, v. 329-330, p. 71-83.

Okubo, C.H., and Schultz, R.A., 2005, Evolution of damage zone geometry and intensity in porous sandstone: insight gained from strain energy density: Journal of the Geological Society, v. 162, p. 939-949.

Peppard, D.W., Webb, H.N., Dennis, K., Vierra, E., Girty, G.H., Rockwell, T.K., Blanton, C.M., Brown, J.F., Goldstein, A.I., Kastama, K.W., Korte-Nahabedian, M., Puckett, D., and Richter, A.K., 2018, Micro-scale damage characterized within part of a dismembered positive flower structure, San Jacinto fault, southern California, USA: Journal of Structural Geology, v. 112, p. 53-68.

Qin, L., Ben-Zion, Y., Qiu, H., Share, P., Ross, Z.E., and Vernon, F.L., 2017, Internal structure of the San Jacinto fault zone in the trifurcation area southeast of Anza, California, from data of dense seismic arrays: Geophysical Journal International, v. 213, p. 98-114.

Qiu, H., Ben-Zion, Y., Ross, Z.E., Share, P.-., and Vernon, F.L., 2017, Internal structure of the San Jacinto fault zone at Jackass Flat from data recorded by a dense linear array: Geophysical Journal International, v. 209, p. 1369-1388,

Rockwell, T., Loughman, C., and Merifield, P., 1990, Late Quaternary rate of slip along the San Jacinto Fault Zone near Anza, southern California: Journal of Geophysical Research: Solid Earth, v. 95, p. 8593-8605.

Rockwell, T., Dawson, T., Young Ben-Horin, J., and Seitz, G., 2015, A 21-Event, 4,000-Year History of Surface Ruptures in the Anza Seismic Gap, San Jacinto Fault, and Implications for Long-term Earthquake Production on a Major Plate Boundary Fault: Pure and Applied Geophysics, v. 172, p. 1143-1165.

Roux, P., Moreau, L., Lecointre, A., Hillers, G., Campillo, M., Ben-Zion, Y., Zigone, D., and Vernon, F., 2016, A methodological approach towards high-resolution surface wave imaging of the San Jacinto Fault Zone using ambient-noise recordings at a spatially dense array: Geophysical Journal International, v. 206, p. 980-992.

Salisbury, J. B., Haddad, D. E., Rockwell, T., Arrowsmith, J R., Madugo, C., Zielke, O., Scharer, K., 2015, Validation of meter-scale surface faulting offset measurements from high-resolution topographic data, Geosphere, v. 11, no. 6, p. 1–18.

Salisbury, B., Rockwell, T., and Buga, M., 2017, Paleoseismic Evidence for the 21 April 1918 Mw 6.9 Surface Rupture of the Northern Clark Strand of the Central San Jacinto Fault, California: Bulletin of the Seismological Society of America.Berkeley CA, v. 107, p. 1027-1032.

Sanders, C.O., and Kanamori, H., 1984, A seismotectonic analysis of the Anza Seismic Gap, San Jacinto Fault Zone, southern California: Journal of Geophysical Research: Solid Earth, v. 89, p. 5873-5890.

Schwanghart, W., Scherler, D., 2014, TopoToolbox 2 – MATLAB-based software for topographic analysis and modeling in Earth surface sciences. Earth Surface Dynamics, v.2, p. 1-7.

Share, P., Ben-Zion, Y., Ross, Z.E., Qiu, H., and Vernon, F.L., 2017, Internal structure of the San Jacinto fault zone at Blackburn Saddle from seismic data of a linear array: Geophysical Journal International, v. 210, p. 819-832,

Sharp, R.V., 1967, San Jacinto fault zone in the Peninsular Ranges of Southern California: Geological Society of America Bulletin, v. 78, p. 705-729.

Sharp, R.V., 1981, Variable rates of Late Quaternary strike slip on the San Jacinto Fault Zone, southern California: Journal of Geophysical Research: Solid Earth, v. 86, p. 1754-1762.

Shi, Z., and Ben-Zion, Y., 2006, Dynamic rupture on a bimaterial interface governed by slip-weakening friction: Geophysical Journal International, v. 165, p. 469-484.

Thatcher, W., Hileman, J., and Hanks, T., 1975, Seismic Slip Distribution along the San Jacinto Fault Zone, Southern California, and Its Implications: Bulletin of the Geological Society of America, v. 86, p. 1140-1146.

UNAVCO, 2010, San Jacinto Fault Zone at Anza B946 sagebf946bcs2010, Unpublished Installation Report.

US Geological Survey, 2006, Quaternary fault and fold database for the United States: https://earthquake.usgs.gov/hazards/qfaults/ (accessed January 2017).

Vernon, F., and Ben-Zion, Y.2010. San Jacinto Fault Zone Experiment. International Federation of Digital Seismograph Networks. Other/Seismic Network, doi:10.7914/SN/YN_2010.

Wechsler, N., Rockwell, T.K., and Ben-Zion, Y., 2009, Application of high resolution DEM data to detect rock damage from geomorphic signals along the central San Jacinto Fault: Geomorphology, v. 113, p. 82-96.

Whearty, J.J., Rockwell, T. K., and Girty, G., 2017, Incipient pulverization at shallow burial depths along the San Jacinto fault , southern California, *in* Thomas, M.Y., Mitchell, T.M., and Bhat, H.S., ed., Fault Zone Dynamic Processes: Evolution of Fault Properties During Seismic Rupture, American Geophysical Union Monograph 227, p. 3-20.

Yang, H., and Zhu, L., 2010, Shallow low-velocity zone of the San Jacinto fault from local earthquake waveform modelling: Geophysical Journal International, v. 183, p. 421-432.

Yang, H., Li, Z., Peng, Z., Ben-Zion, Y., and Vernon, F., 2014, Low-velocity zones along the San Jacinto Fault, Southern California, from body waves recorded in dense linear arrays: Journal of Geophysical Research: Solid Earth, v. 119, p. 8976-8990.

Zielke, O., Y. Klinger, and J R. Arrowsmith (2015), Fault Slip and Earthquake Recurrence Along Strike-Slip Faults --Contributions of High-Resolution Geomorphic Data, Tectonophysics, v. 638, p. 43-62.

Table 2: Displacement measurements of offset stream channels along faults (F102, F104, F106, F108, and F110) within SGB and Alkali Wash produced using LiDaCaoz 2.1 (Zielke, et al, 2015; Haddon, et al., 2016). Locations and detailed images of offset location are found in figures 2-9 and 2-10 respectively.

Offset Location ID	Latitude	Longitude	Best Horz. Offset (m)	Best Vert. Offset (m)	Vert. Offset Range (m)	Fault ID	Quality
SCO-01	33.53756	-116.59021	12.3	0.6	0.0 - 1.3	F106	Fair
SCO-02a	33.53776	-116.58974	16.2	0.9	0.0 - 1.7	F104	Good
SCO02b	33.53779	-116.58943	15	2	0.0 - 2.7	F102	Poor-Fair
SCO-03	33.53592	-116.58805	15.9	1.6	0.0 - 2.4	F106	Good
SCO-04	33.53551	-116.58723	3.1	0.3	0.0 - 1.5	F106	Poor-Fair
SCO-05	33.53525	-116.58517	3.4	2.9	0.0 - 5.0	F110	Fair (Good but not on main trace)
SCO-06	33.53686	-116.58861	5.7	0.3	-0.5 - 1.0	F104	Very good
SCO-07	33.53622	-116.58901	2.8	1	0.0 - 2.0	F108	Fair

Table 3 SGB Excavation Soil Descriptions from fault perpendicular trench (Figures 2-12 through 2-14.

Soil Unit	Soil Description
Unit 100	Light grayish brown, med. dense clayey sand/sand w/clay, dry, 15% cohesive fines, 85% fine to med. grained sub rounded sand; trace carbonate. Abrupt contact with bedrock.
Unit 101-1 and 101-2	Alluvium. Clayey SAND/SAND w/Clay, dry, med. dense light grayish brown, 15% cohesive fines, 85% fine to med. grained sub rounded sand; trace carbonate. Few 1mm to 1 cm roots. Occasional angular metamorphic gravel and cobbles up to 10 cm in size at beginning and terminus of unit. Diffuse contact with 100. Unit 101-2 on SE side of trench similar in color and texture but with larger values of clasts concentration
Unit 102	Dark grayish brown, loose to med. dense, sandy silt, dry, 25% low plasticity fines, 75% fine to coarse angular to sub-rounded sand. Abundant fine mica and coarse quartz grains. Trace 1mm to 1 cm roots. Abrupt contact with 101.
Unit 103	Dark grayish brown, loose to med. dense, sandy silt, dry, 25% low plasticity fines, 75% fine to coarse angular to sub-rounded sand. Abundant fine mica and coarse quartz grains. Trace angular metamorphic gravels. Platy horizontal structure.
Unit 200 :	Dark yellowish brown, grayish brown and orangish brown, dry to moist, med .dense, gravely, clayey sand. 15% sub angular to angular decomposed to intensely weathered gneiss gravels. 30% fines. 65% fine to med sand. Diffuse color change and stone line contact with 100b.
Unit 201	Dark yellowish brown to orangish brown, dry to moist, med dense to dense, clayey sand with gravel. 15% angular to sub angular decomposed to intensely weathered 2 cm to 5 cm (trace 10cm) gneiss gravels. 30% med plasticity fines. 65% fine to med sub rounded sand. Diffuse contact with 200
Unit 202	Dark grayish brown and dark orangish brown, dry, med. dense to dense, silty gravely sand. 15% non plastic fines, 30% angular decomposed to intensely weathered cobbles and gravels, 65% fine to med. sub rounded to sub angular sand. No soil structure. Gradational/diffuse contact with 201.
Unit 203	Dark orangish brown and light brownish gray, dry, med. dense to dense, silty sand with gravel. 15% non plastic fines,15 % 2-10cm angular gneiss gravels, 70% fine to med. sand grains. Abrupt boulder contact with 202.

Table 3 continued.

Soil Unit	Soil Description
Unit 204	Dark orangish brown and light brownish gray, dry, med. dense to dense, silty Gravel and sand. 15% non plastic fines, ~50% sub angular to angular gneiss graves, cobbles and boulder clasts. Partially clast supported partially matrix supported. No soil structure. Abrupt dark gray stone line contact.
Unit 205	Light yellowish brow, med. dense, dry, Gravely Silty SAND. 15% non plastic fines, 20% 2-10cm angular metamorphic gravels, 65% fine to coarse sub angular to angular sand grains. Cut and fill unit over 204.

Table 4: Deformation Zone Descriptions from SGB excavation below F104 on NE side of trench (Figure 2-12)

Zone ID	Zone Descriptions
Zone A:	Light gray to grayish brown weak to med. strong moderately weathered poorly indurated sandstone (?). Fault dip's 50 degrees east. Subvertical to fault parallel oriented fractures spaced 1-10 cm apart. Trace 2cm or less sized metamorphic gravels. Includes a roughly 1 - 10 cm thick shear with several <2cm metamorphic gravels near the base. Approximately 60 cm thick.
Zone B:	Light gray to dark orangish brown soft to medium hard poorly indurated breccia. 2cm to 10cm angular gneiss clasts with orangish brown silt and sand size matrix. No visually identifiable orientation to clast or matrix. Stops at station 12h. Bottom shear oriented approximately 070.
Zone C:	Light gray to dark orangish brown soft to medium hard poorly indurated breccia. 2cm to 20cm angular gneiss clasts with orangish brown silt and sand size matrix. Less consolidated than zone B. 55 degree east dipping shear at base with 5 cm thick orangish brown oxidation. 0.5 -1 m thick.
Zone D:	Grayish brown, brown, and orangish brown, soft poorly indurated breccia. > 1 - 10 cm angular gneiss clasts with orangish brown silt and sand size matrix. Partially matrix supported near surface. 70 degree east dipping shear at base.
Zone E:	White, light grayish brown with trace orangish brown, soft, poorly indurated breccia. Primarily silty matrix and pulverized rock with rare 10cm angular gneiss clasts and scattered 2cm or smaller angular clasts. 50 degree east dipping shear at base.

Table 5. Rock damage classification (Dor et al., 2006) used in the rock damage survey in SGB and Alkali Wash (Figures 2-15 through 2-17).

Rock Damage Class	Description
(I) weak fracturing	Macroscopic large fractures in density that exceeds the background level of damage in the country rock.
(II) Fragmentation	Fractures are in the cm scale and the rock is fragmented, resulting in the creation of rugged surfaces. Some of the fragments can be easily crushed by hand into smaller, visible pieces.
(III) Intense fracturing	Fractures are in the grain size scale. Although similar in texture to grus, its mechanical origin is attested by its structural context and location in the deformation gradient. It is typically characterized by rough, rounded surfaces.
(IV) Weak/ selective pulverization	Some of the crystals survive and remain intact, some break along sub-crystal fractures, and some yield powdery texture due to microscopic fractures. The typical appearance in the field often can be similar to that of the next (highest) damage class.
(V) Pervasive pulverization	All crystals yield a powdery texture when crushed by hand. Associated geomorphic landforms tend towards smooth, rounded outcrops or bad-land topography with extremely high drainage density, which is typical of very weak, easily eroded impermeable rock.

Table 6: Parameters used to construct 3D fault zone model in Move (Figure 2-25). Fault surface trace location imported from ArcGIS and initial surface geometry projected based surface measurements listed in the table below.

Fault ID	Sense of motion	Geometry/Dip	Justification
F100	Dextral Strike Slip	77° SW	Burnt Valley Rd Cut
F102	Dextral Strike Slip	77° SW	Burnt Valley Rd Cut
F104	Dextral Strike Slip	90°	Alkali Wash Outcrop
F106	Dextral Strike Slip	80° NE	Trench exposure
F202	Thrust (SW up)	55° SW	Burnt Valley Outcrops

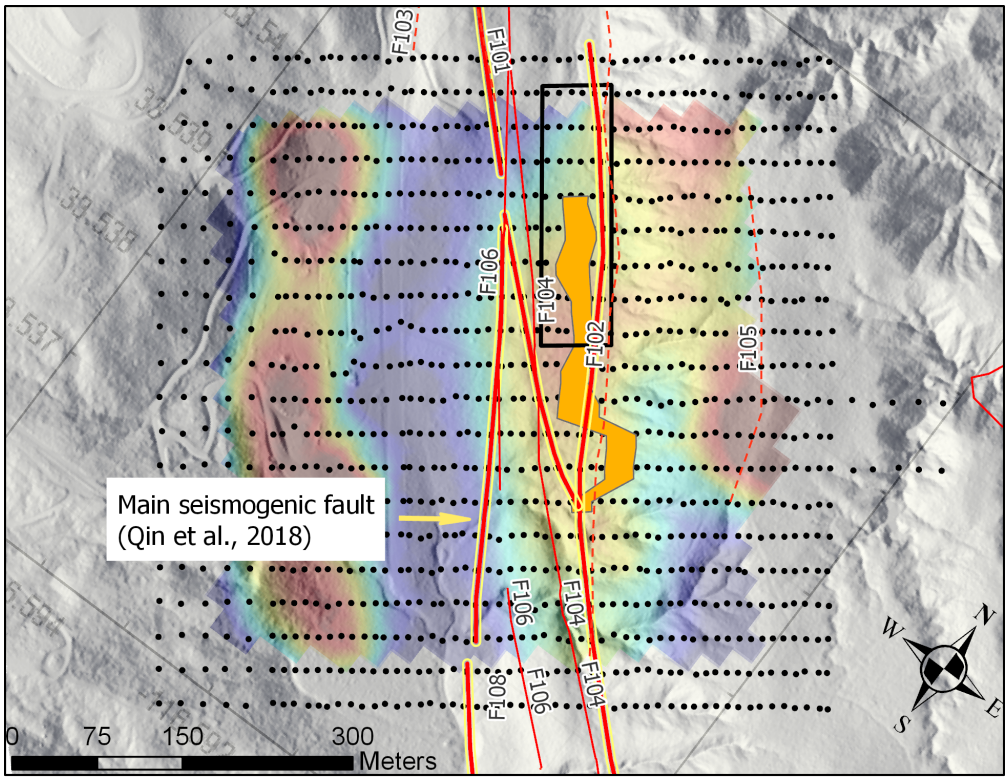

Explanation:

- SGB Dense Array Node

SJFZ (This study)

Fault

Fault-Inferred

SJFZ(USGS, 2006)

Trapping structure
(Ben-Zion et al., 2015)

Trapping structure
(Qin et al., 2018)

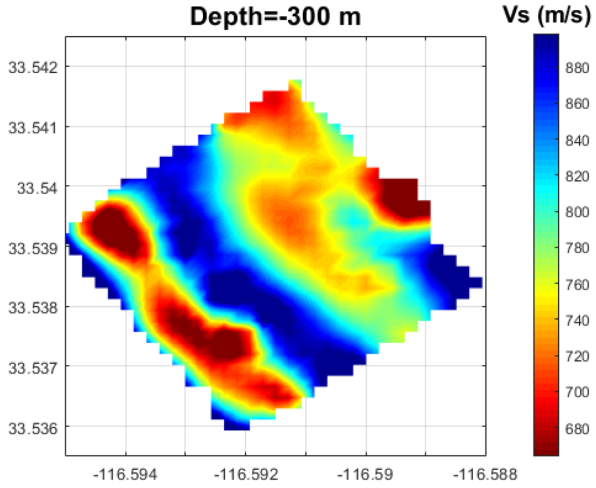

Plot of Vs shear wave velocity model at
300 m depth, georeferenced in map above.

Figure 2-1: SGB dense array configuration and FZTW locations. B4 DTM hillshade base map with mapped fault traces (red lines) based on USGS (2006) Quaternary fault database and my mapping. 1108 black dots indicate individual node locations. Orange polygon and black box indicate FZTW as identified by Ben-Zion et al. (2015) and Qin et al. (2018), respectively. Plot of Vs shear wave model (Mordret et al., 2018) from 300 m depth georeferenced and shown below the array configuration

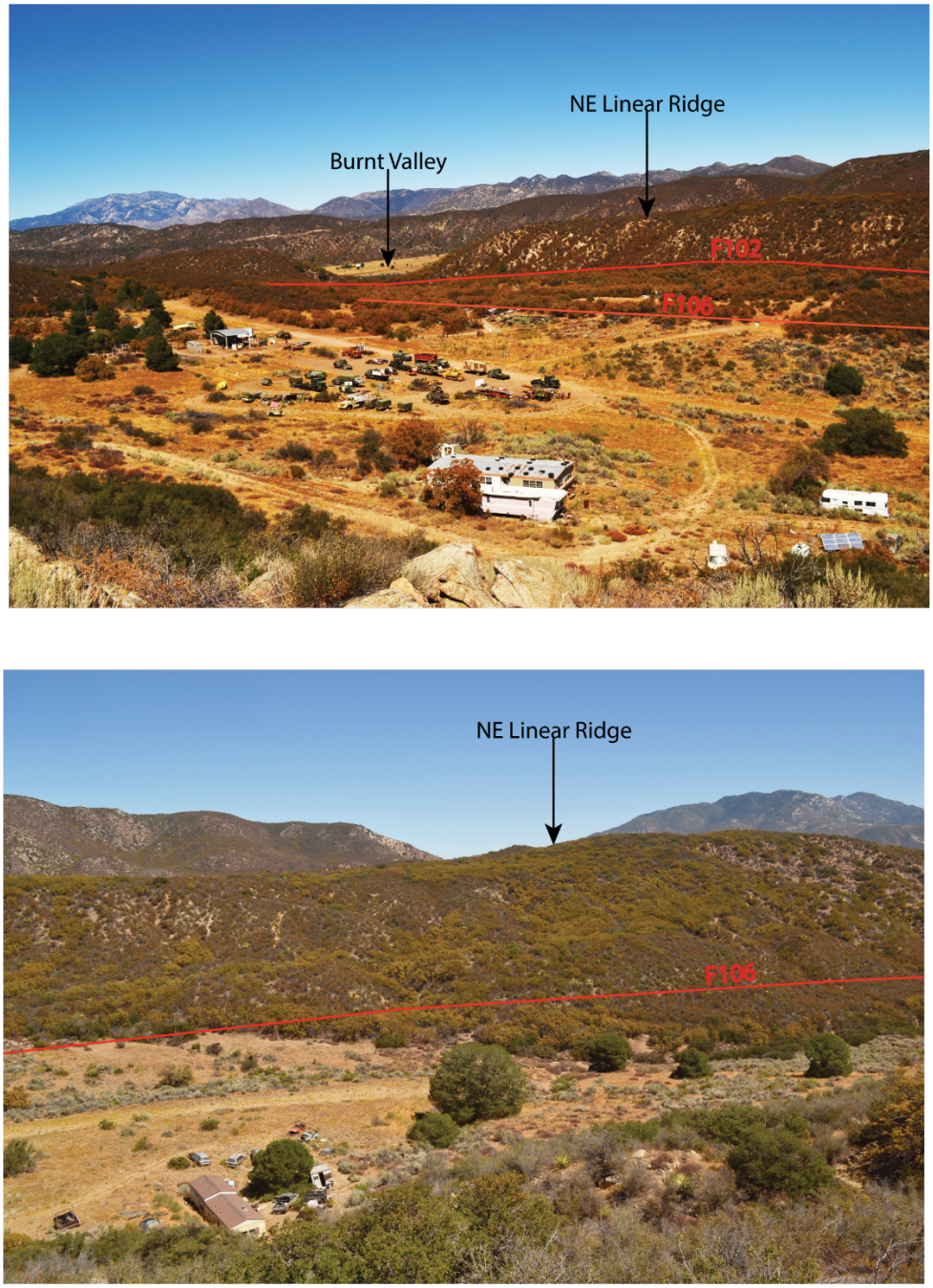

Figure 2-2: Overview photographs of Sage Brush Flat (SGB). Upper photograph shows the linear ridge line separating Burnt Valley (seen in background) and the SGB basin, and mapped fault traces (red lines) as viewed towards the north. Cultural features (land owner's equipment) are observed scattered throughout the basin floor. Lower photograph shows the linear ridge on the NE side of the basin, mapped fault trace, and narrowing of the basin towards the SW into Alkali Wash (to the right; not observed in this photograph).

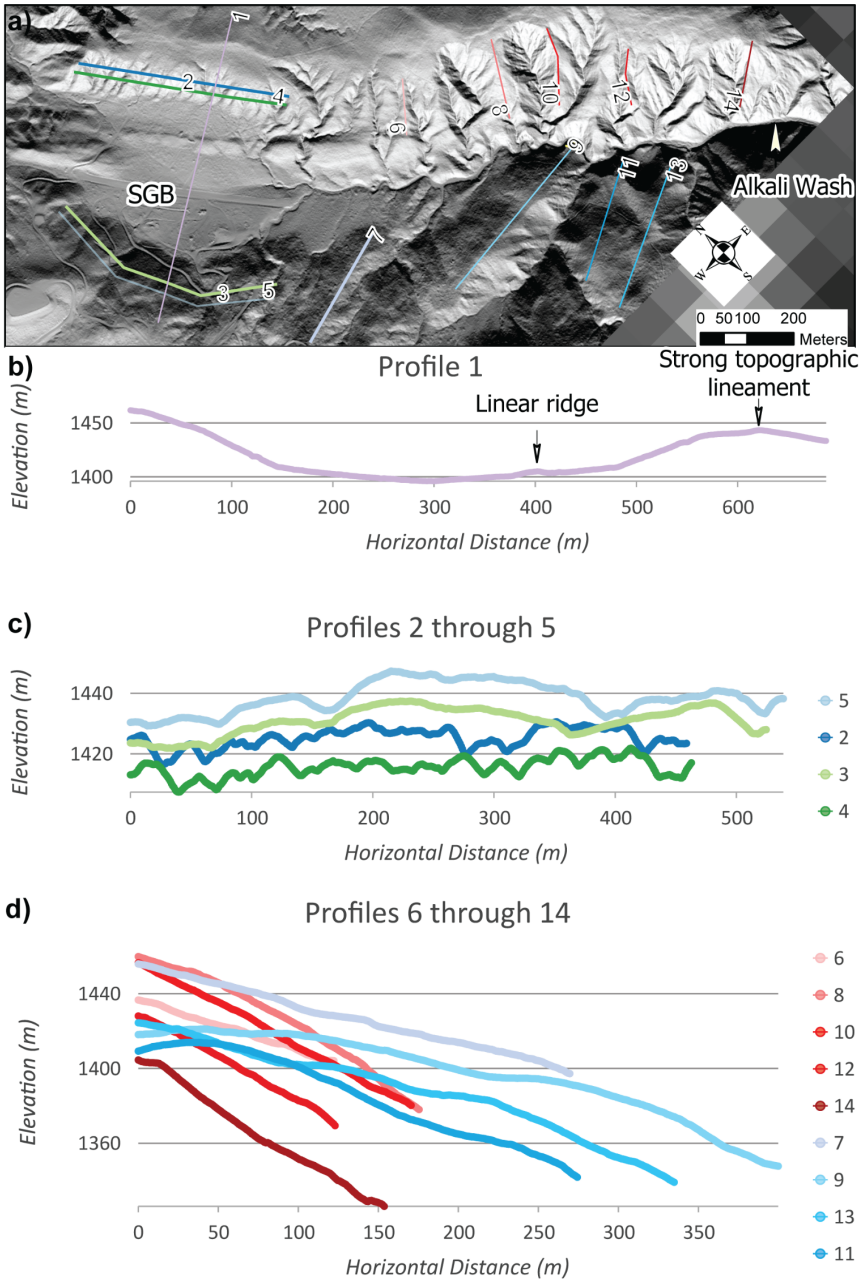

Figure 2-3: Overview of SGB site morphology. a) B4 hillshade basemap with locations, and topographic profile lines in yellow. b) Profile line 1 represents slope parallel topography across the valley floor from SW to NE illustrating a longer slope on the SW side and prominent linear ridge and lineaments used for fault trace mapping. c) Profile lines 2 through 5, even and odd numbers represent SW and NE flanking slopes respectively. Lines 2 and 4, and 3 and 5, show relatively low frequency incision and a smoother surface contrasted against the rugged surface and high frequency incision observed in 2 and 4. d) Profile lines 6 through 14, even and odd numbers illustrated by warmer and cooler colors, and representing SW vs NE spurs in SGB and Alkali Wash. Spurs on the NE side the study area (within the BVC) generally have steeper gradients.

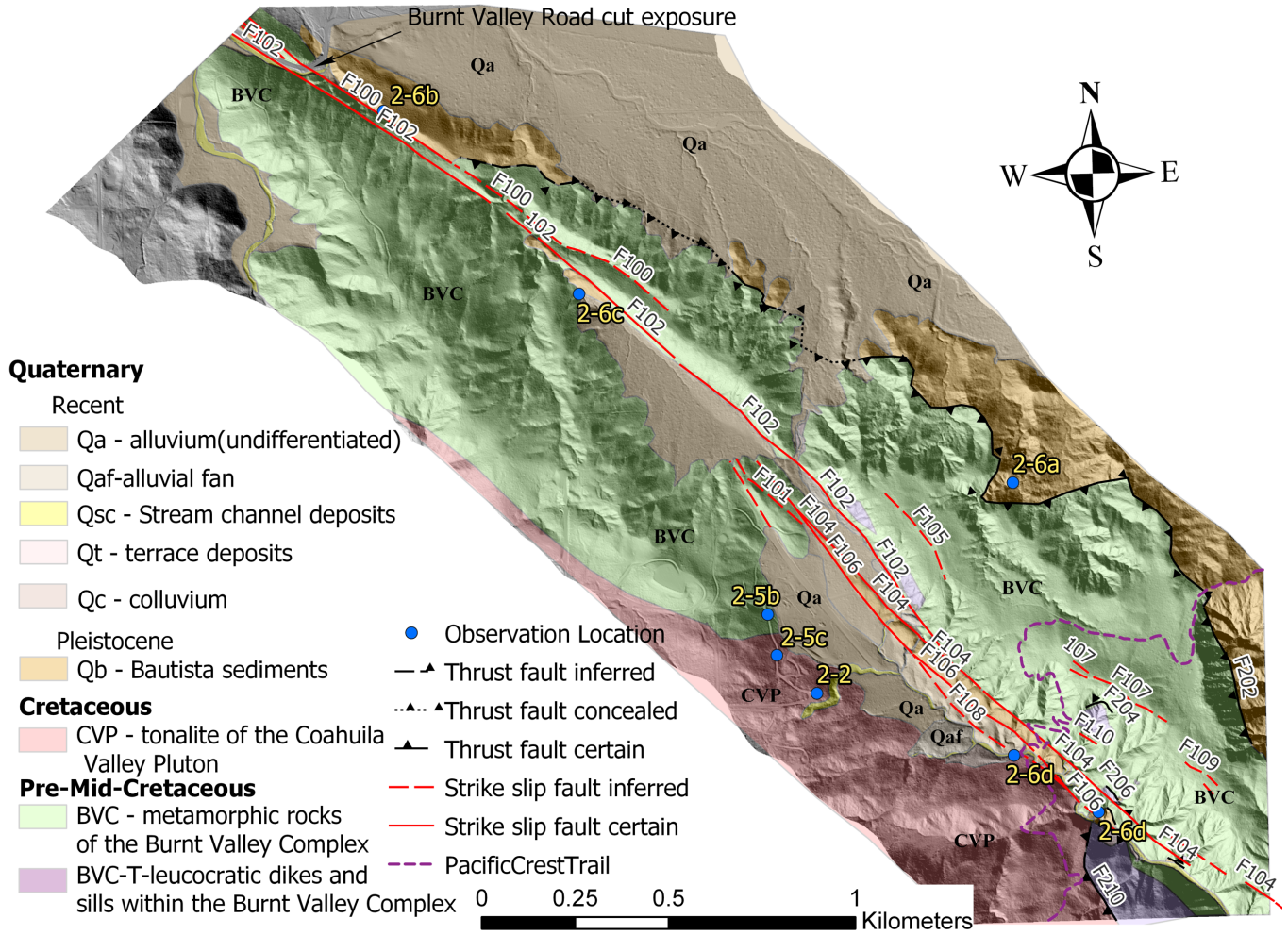

Figure 2-4: Geologic Map of SGB and surrounding areas. B4 hillshade basemap (Bevis et al., 2005) from Burnt Valley Road (NW)to Alkali Wash (SE). Fault trace mapping and nomenclature based on efforts from this study, described in Section 2.6, and illustrated in more detail in figures 2-8 and 2-9. Blue dots with yellow numbers indicate locations described in text and observed in figures 2-5 and 2-6.

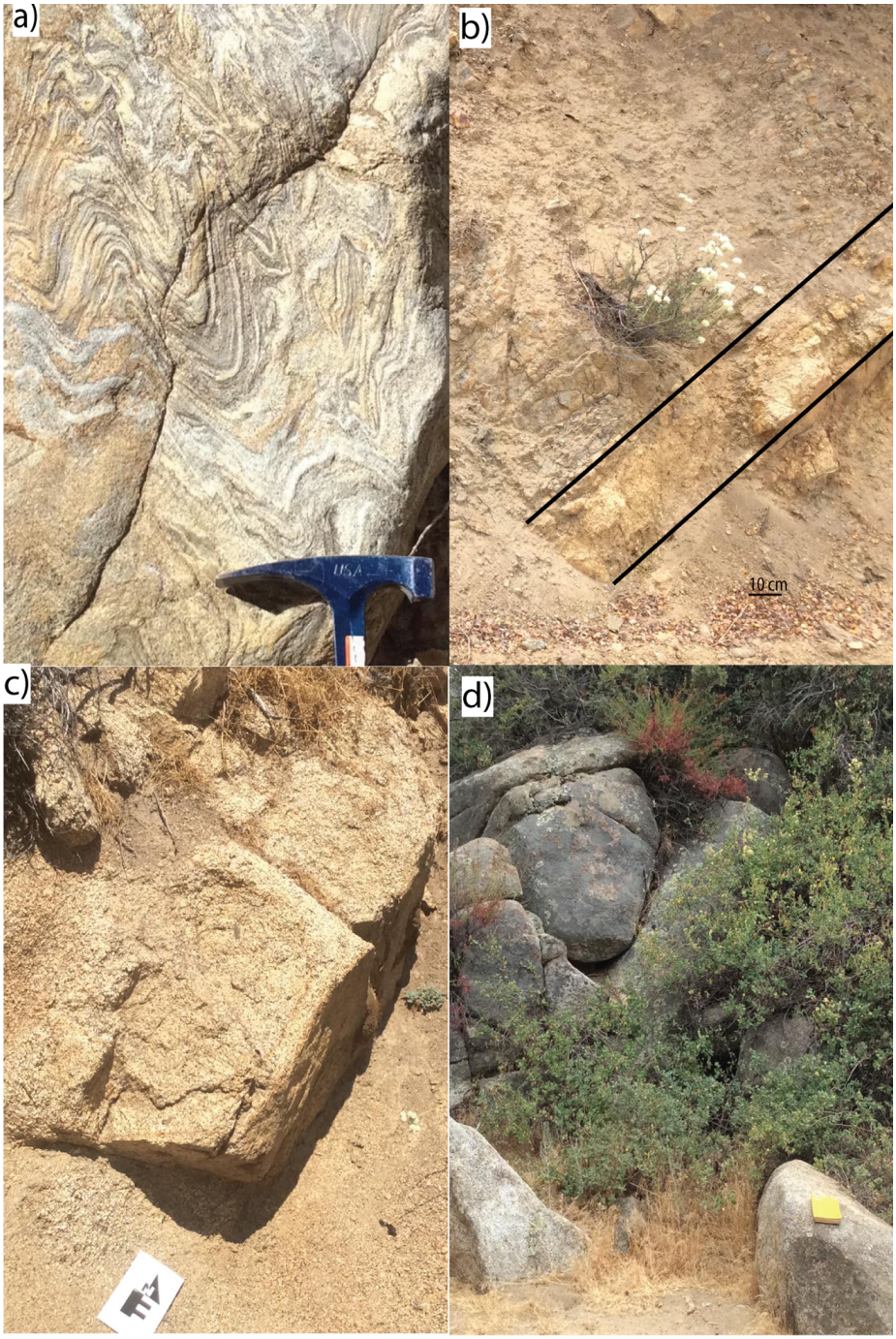

Figure 2-5: Examples of metamorphic and plutonic rock units of SGB (see locations in Figure 2-4): a) float of gneiss showing shear bands in Alkali Wash (BVC), b) roughly 20 cm leucocratic dike (outlined with parallel black lines) within BVC outcrop in landowner's road cut (BVC), c) indurated core-stone of tonalite within weathered material, observed on SW slope of SGB basin CVP); d) tonalite boulders strewn on SW slope and main channel in Alkali Wash (CVP).

Figure 2-6: Thick older sedimentary deposits observed throughout the study area. Locations for each image are found on the geologic map in Figure 2-3. a) 8 m thick massive silt and sand deposit observed in NW flowing drainage within Burnt Valley. b) Gravel and sand unit found near the Burnt Valley Road cut. c) 2.5 to 3 m thick exposure of sand and gravel between SGB basin and Burnt Valley Road. d) 20 m thick deposit of interbedded sand and gravel within Alkali Wash.

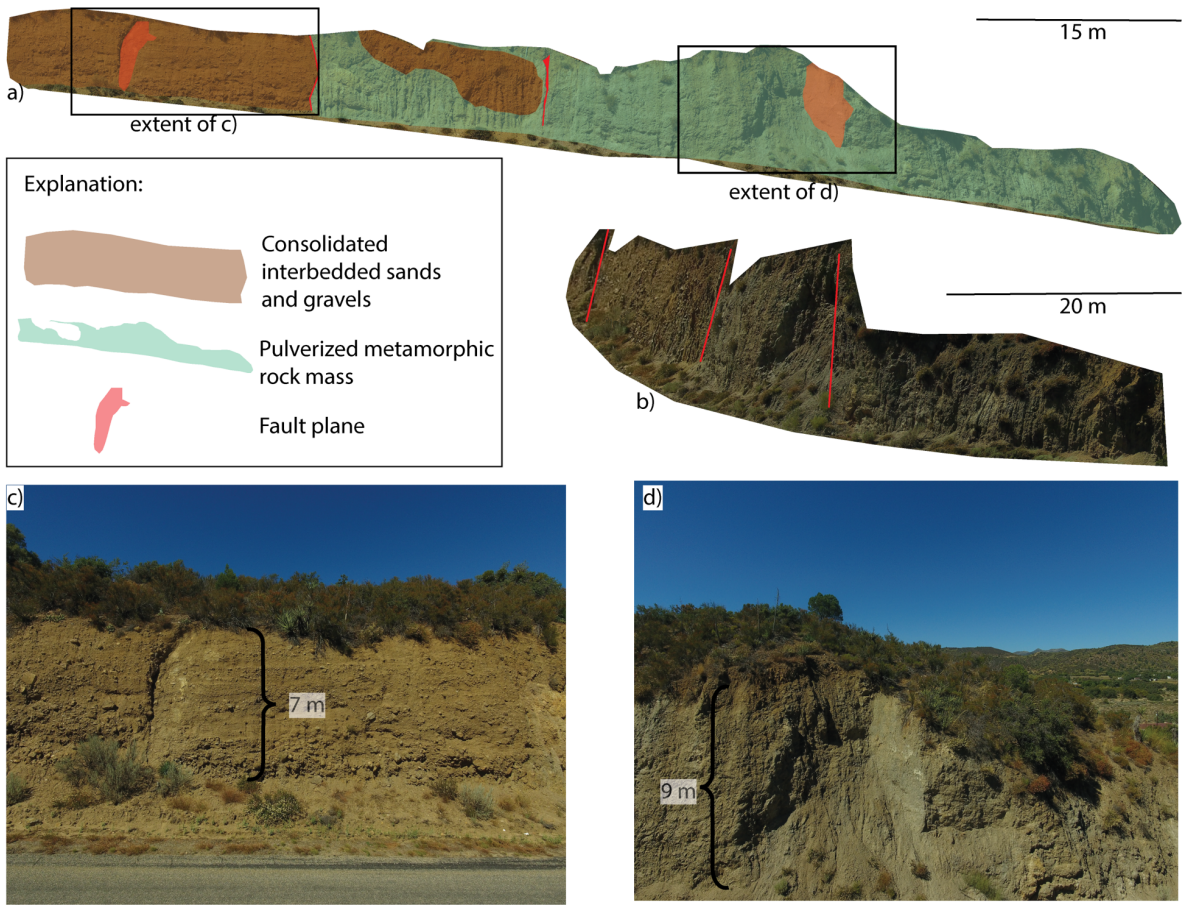

Figure 2-7: Burnt Valley Road cut exposure(location noted in figure 2-6 and 2-7). a) Oblique view of the CF juxtaposing interbedded sands and gravels against pulverized metamorphic rock as viewed towards the NW from the Burnt Valley Road. Individual fault planes are highlighted in red. Note that all pulverized rock is within the BVC. b) Fault parallel view of the CF showing observable thickness of intensely fractured metamorphic rock (fault planes drawn as red lines). c) Close up view of fault plane within interbedded sedimentary unit. D) Close up view of fault plane within pulverized metamorphic rock

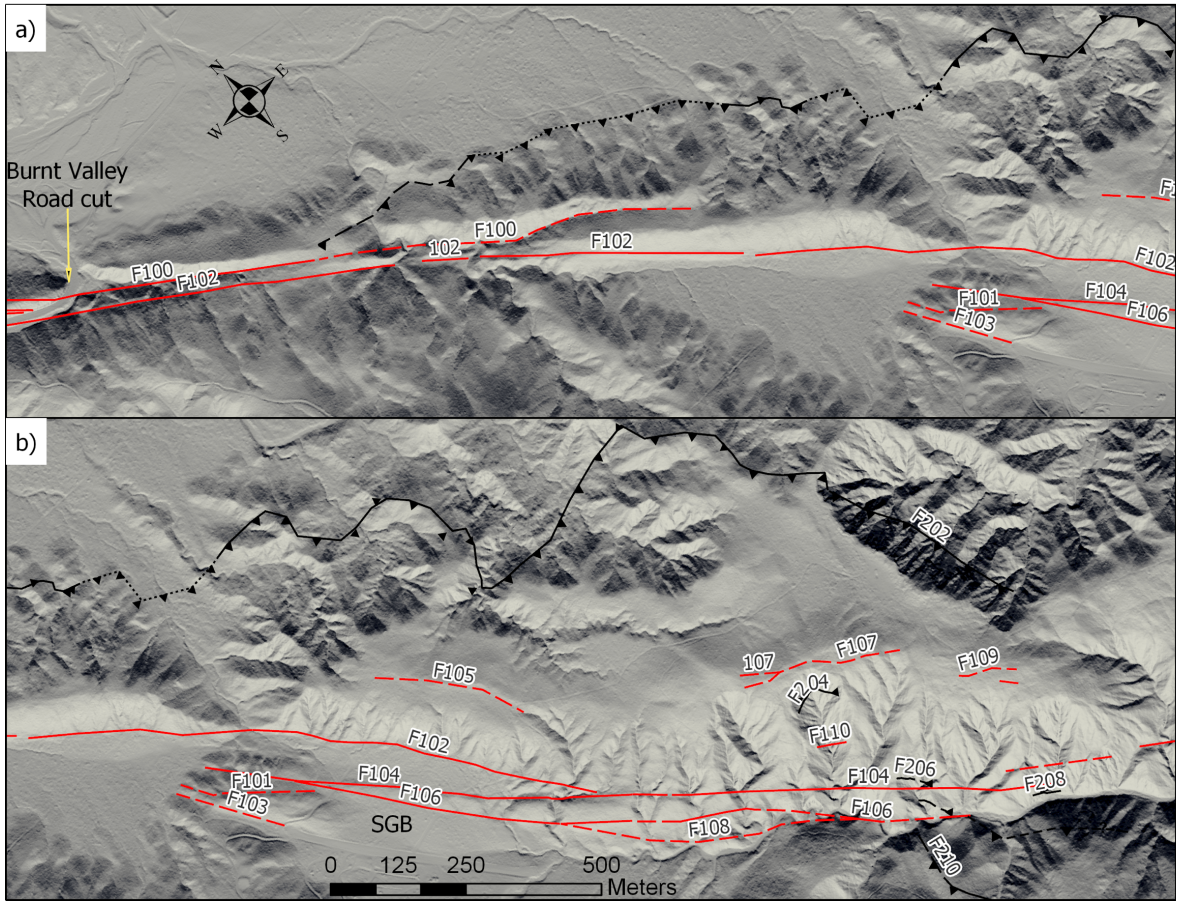

Figure 2-8: SGB fault trace map. Faults traced in red labeled 100 through 109 are considered recently active based on displaced geomorphic features and strong topographic lineaments. Faults with even and odd numbered labels indicate confidence based on offset features or verified in the feature, and inferred only through lineament identification. Faults traced in black indicate a lack of evidence for Holocene activity and primarily based on field mapping with compilation from Sharp, 1967. a) NW half of mapping area from Burnt Valley Road to the edge of the SGB basin. b) SE half of mapping area from the SGB basin to Alkali Wash.

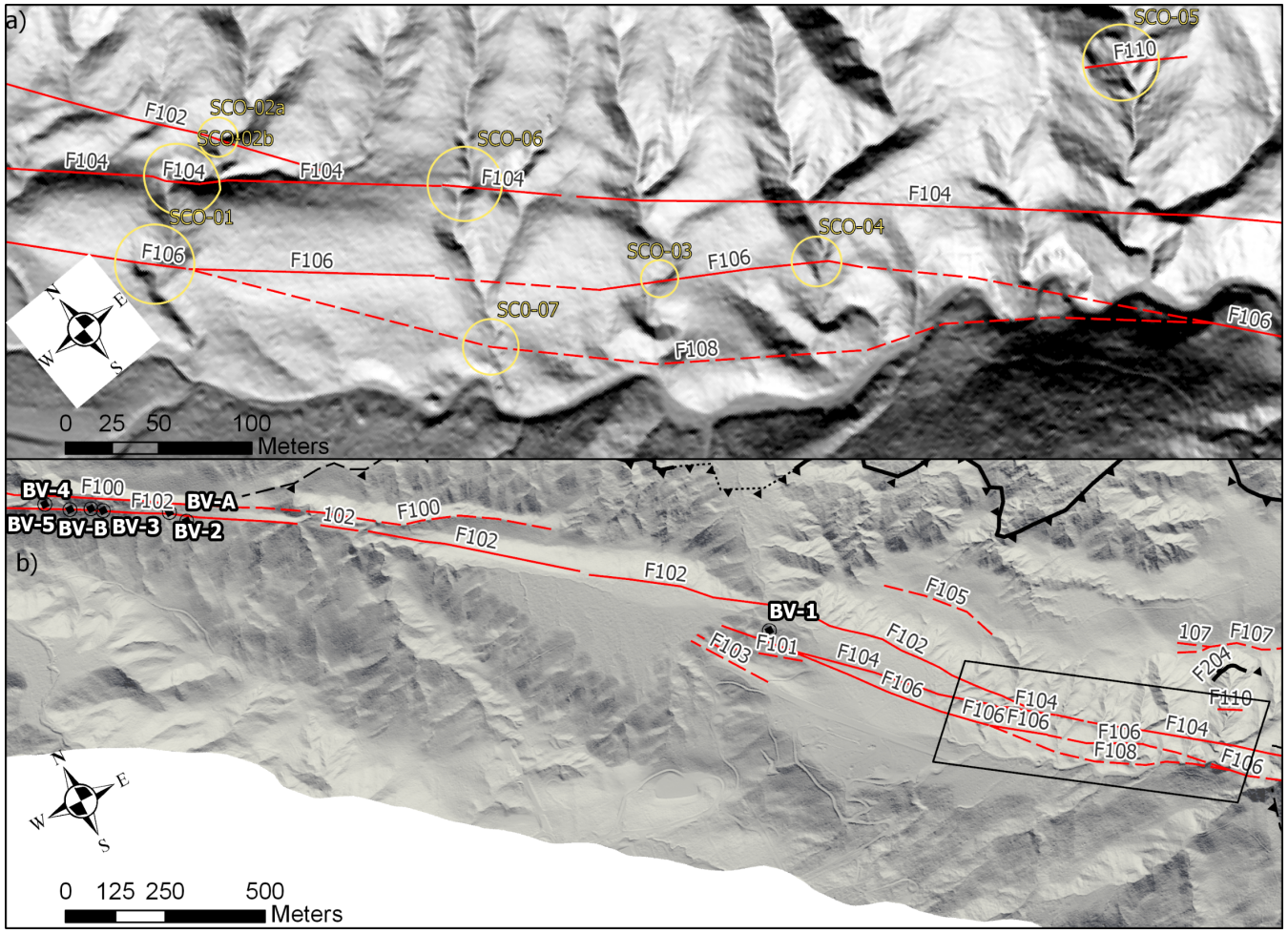

Figure 2-9: Location map of stream channel offsets, yellow circles, along faults F102, F104, F106, F108, and F110, within the SGB basin. Yellow letters are labels for each displacement measured in LaDiCaoz 2.1 (Zielke, et al, 2015; Haddon, et al., 2016) on stream channels showing dextral offset. Labels BV-A, BV-B, and BV-1 through BV-5, are locations of dextral offset measured by Salisbury et al. (2012). Detailed images of each location and value are illustrated in Figure 2-10 and listed

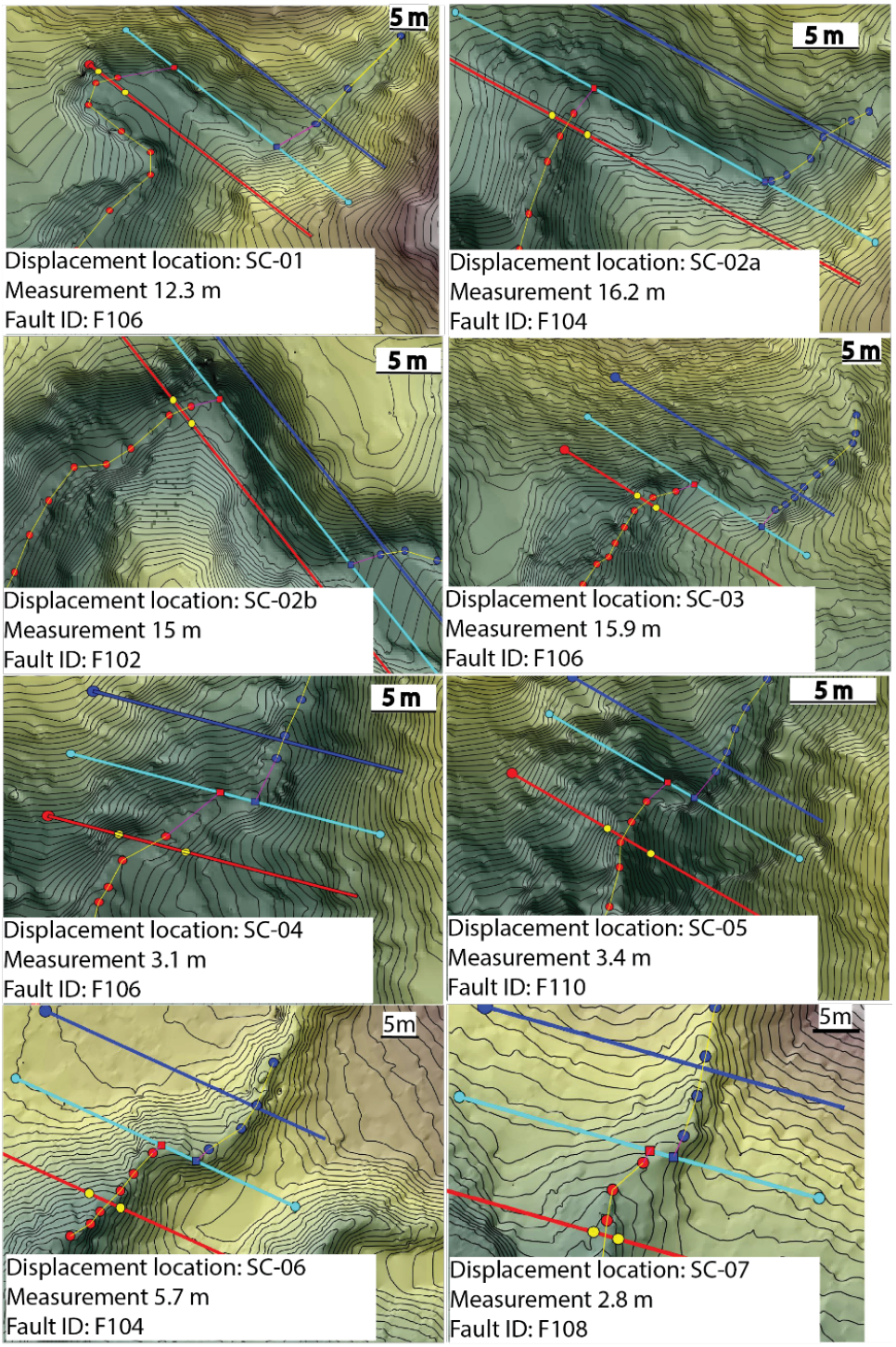

Figure 2-10: LaDiCaoz displacement measurements at 8 locations (SCO-01 through SCO-07) on faults F102, F104, F106, F108, and F110within the SGB basin. Turquoise, blue, and red lines indicate the fault trace, locations of channel profiles used to measure offset respectively. A listing of geographic coordinate location, displacement values and corresponding faults is found on Table 2

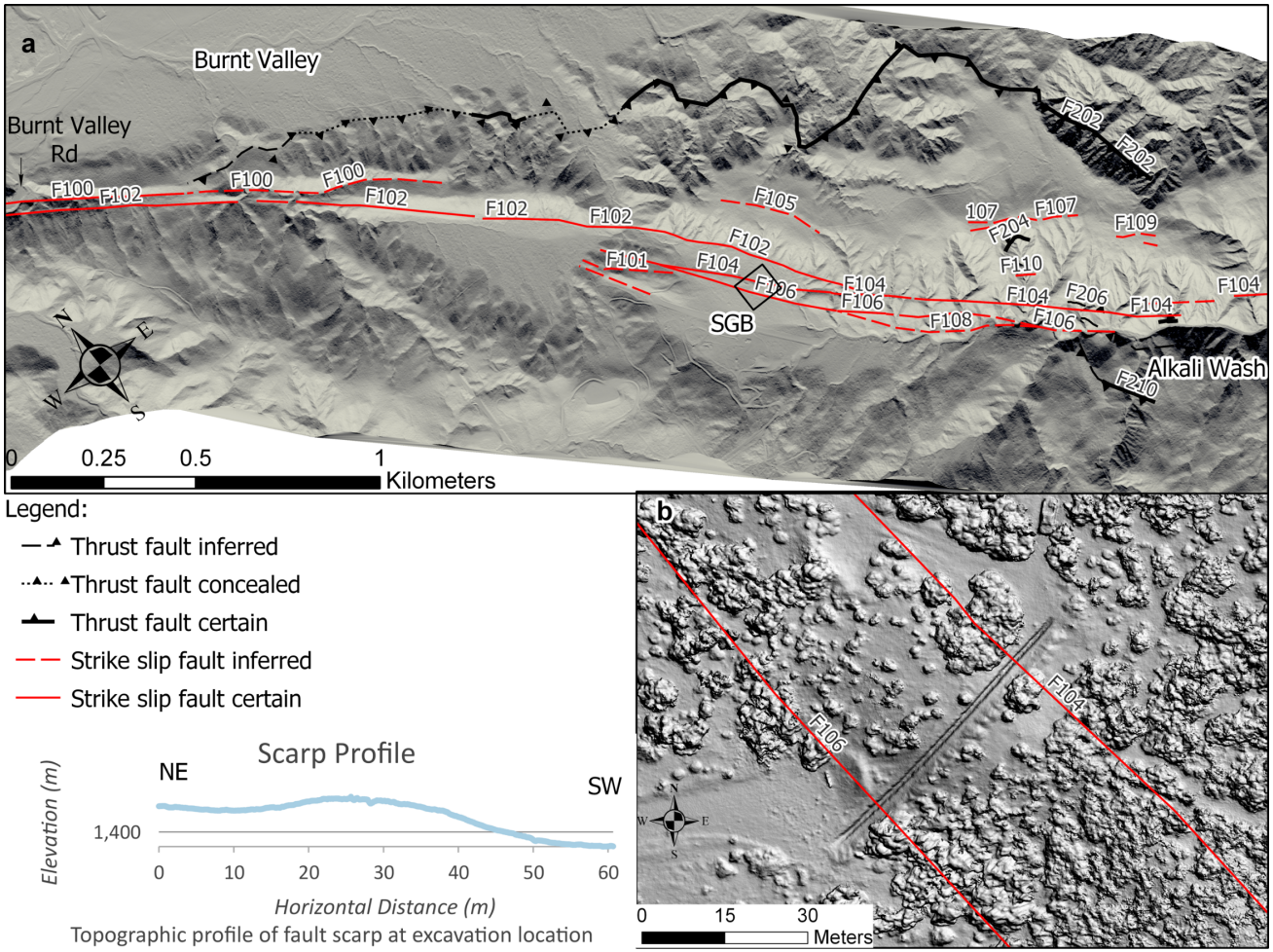

Topographic profile of fault scarp at excavation location

Figure 2-11: SGB fault map and excavation location. a) B4 lidar (Bevis et al., 2005) DTM hillshade with mapped fault traces. Geographic locations Burnt Valley, SGB, and Alkali Wash labeled for reference. Extent of b is indicated by black box. b) Structure from motion DEM hillshade of SGB excavation. Excavation transects the entire length of elongated and fault bounded hill within SGB. Topographic profile illustrates the fault scarp topography of the excavation location.

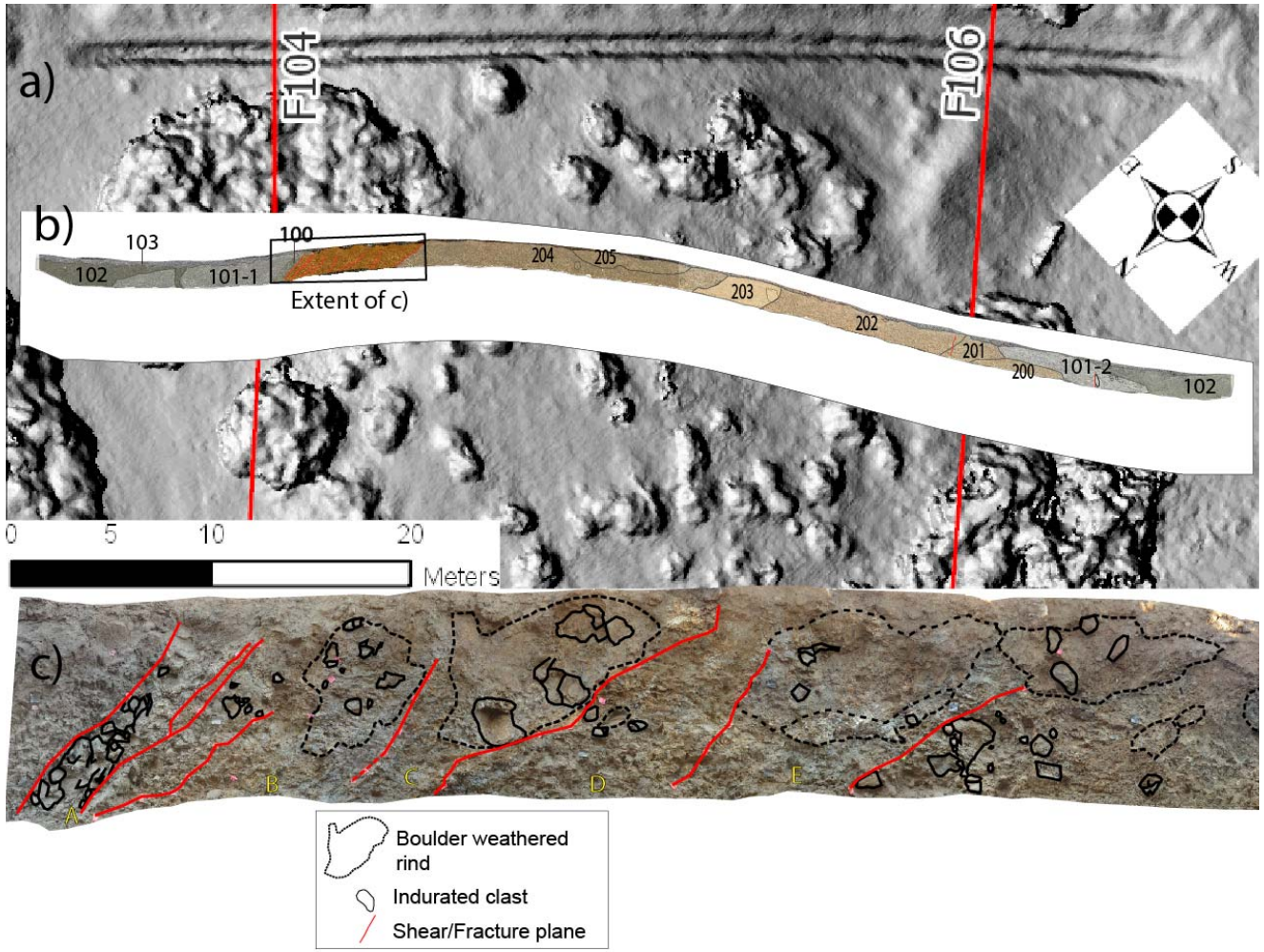

Figure 2-12: Log of excavation with close up photo-logs of the fault zones (F104). A) High resolution sUAS SFM elevation model of excavation location showing the fault-bounded SJF-parallel ridge. b) Trench log of entire exposure showing units 100 through 103, and 200 through 205. Black box indicates extent of c. c) Close up view of deformation zone observed below F104. Weathering rind of individual boulders indicated by dashed black lines. Solid lines indicate indurated clasts. Low angle failure planes (red lines) mapped along clayey patches along boulder weathering extents. Soil unit descriptions and zones A through E described in Tables 3 and 4.

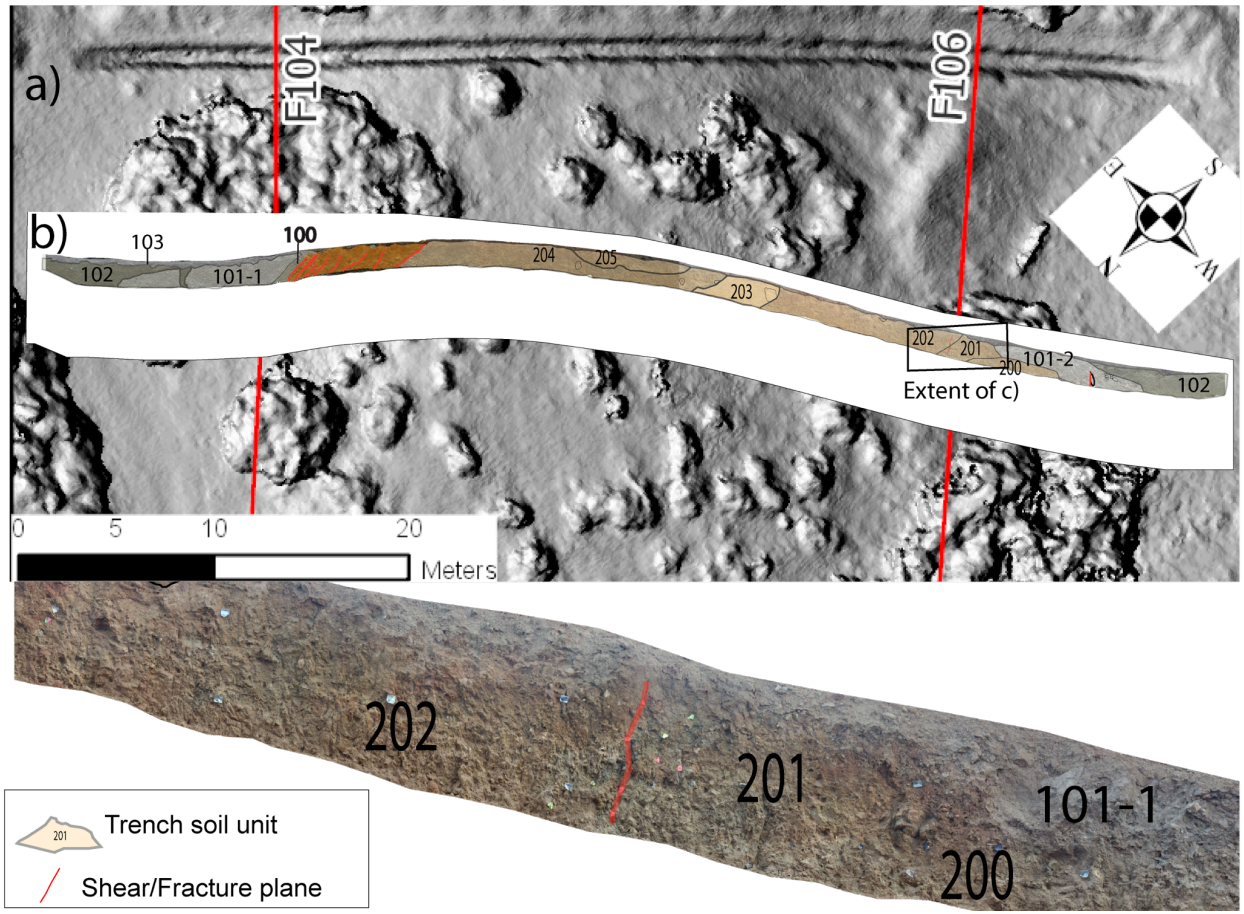

Figure 2-13: Log of excavation with close up photo-logs of the fault zones (F106). a) High resolution sUAS SFM elevation model of excavation location showing the fault-bounded SJF-parallel ridge. b) Trench log of entire exposure showing units 100 through 103, and 200 through 205. Black box indicates extent of c. c) Close up view of deformation zone observed below F106. Fault plane (red line) mapped along fracture extending through units 201 and 202. Soil unit descriptions in Table 3.

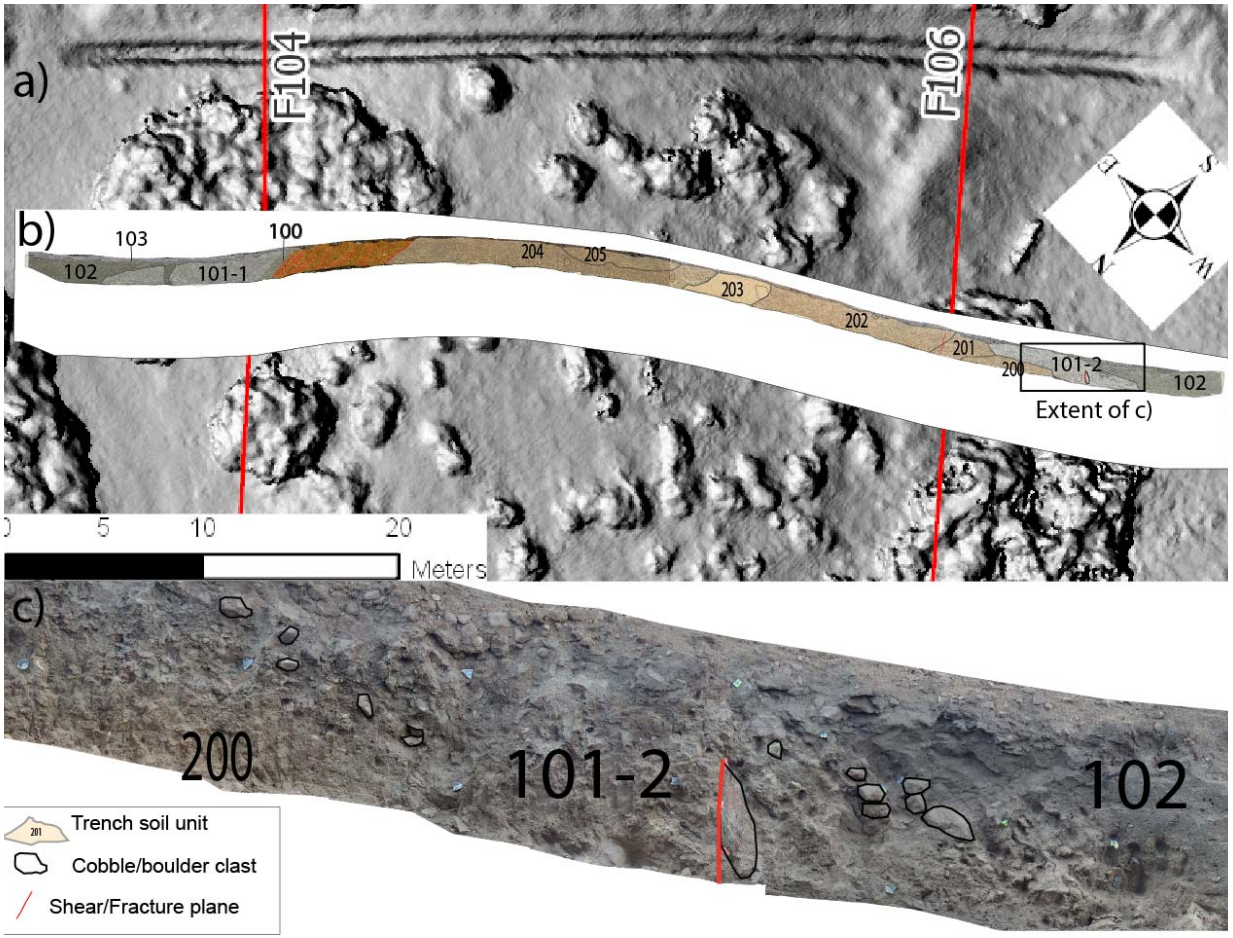

Figure 2-14: Log of excavation with close up photo-log of SW portion below F106. a) High resolution sUAS SFM elevation model of excavation location showing the fault-bounded SJF-parallel ridge. b) Trench log of entire exposure showing units 100 through 103, and 200 through 205. Black box indicates extent of c. c) Red line indicates interpreted fault plane based on vertically oriented long flat boulder clast. No clay gouge, fracture planes or displaced layers observed in young deposits. Units 101-2 and 102 differentiated by color cobble/boulder clast content. Soil unit descriptions in Table 3.

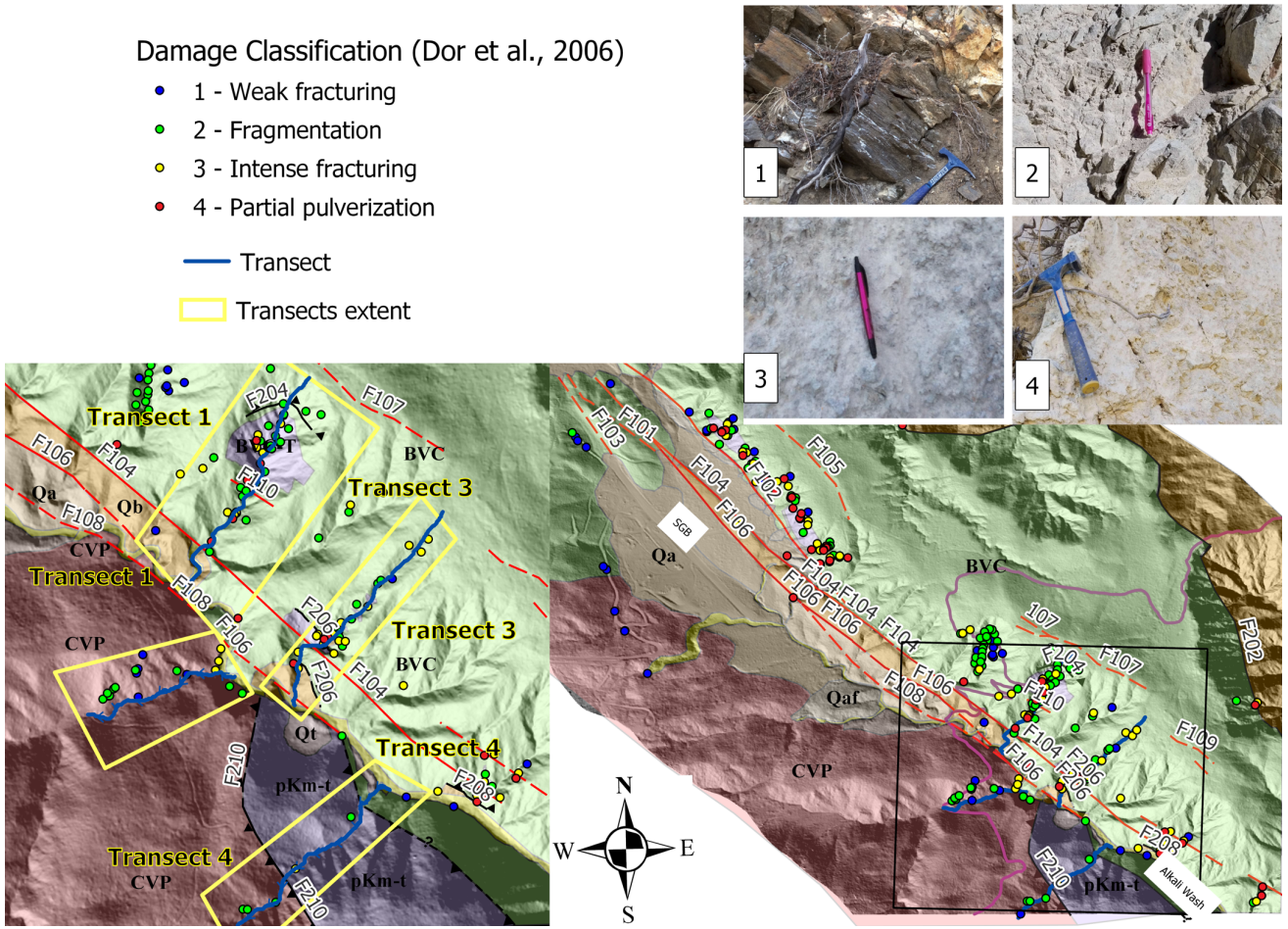

Figure 2-15: Transect location map. a) Abbreviated damage classification from Dor et al. (2006) and pictures of each class (1 through 4) within SGB and Alkali Wash. b) Geologic map of SGB and surrounding areas with rock damage survey points color coded by damage class. Non-survey areas covered by soils/sediments and or dense vegetation. Black box indicates extent of c). c)Location and extents of transects 1 through 4. Transects 1 and 3, and 2 and 4 on NE and SW side of Alkali Wash, respectively.

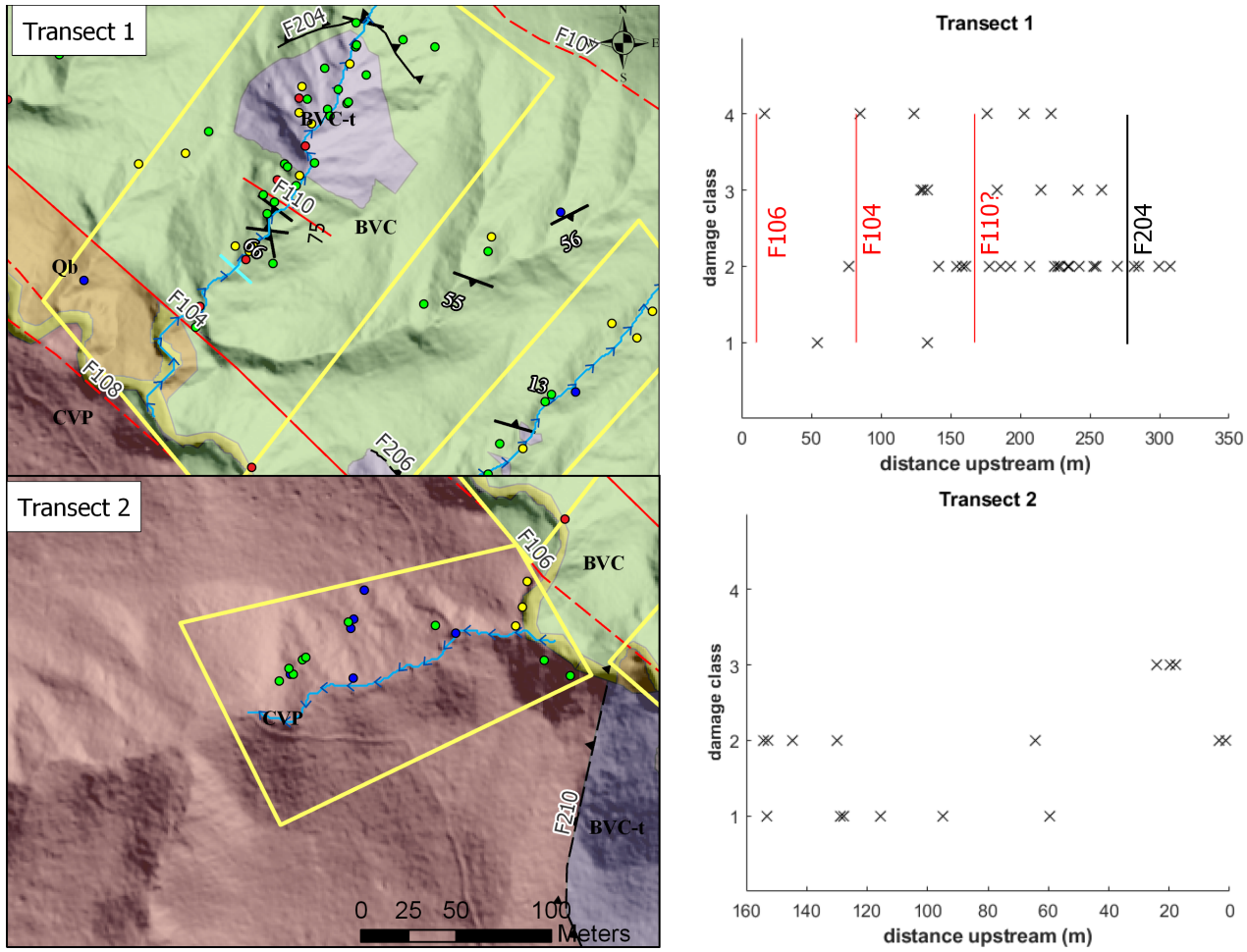

Figure 2-16: Transects 1 and 2. Transect 1 (upper panels) and transect 2 (lower panels). Left side of figure includes the transect geologic map overlain with route, extent and survey points color coded by damage class (see explanation in figure 2-15 for description). Right side of figure displays a plot of damage classification vs. distance upstream along transect route. Transect 1 (NE side of SJFZ) shows consistent higher damage class values at greater distance from the main fault traces

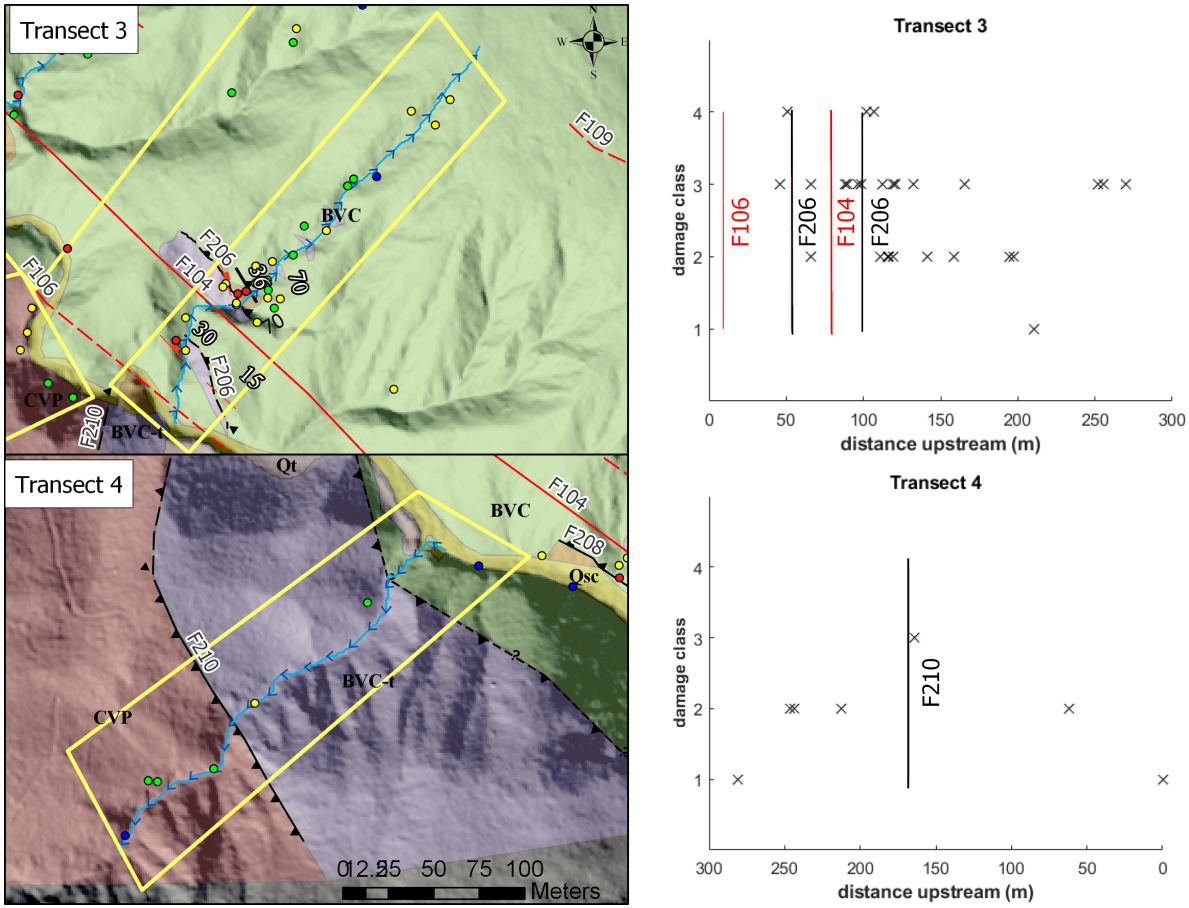

Figure 2-17: Transects 3 and 4. Transect 3 (upper panels) and transect 4 (lower panels). Left side of figure includes the transect geologic map overlain with route, extent and survey points color coded by damage class (see explanation in figure 2-15 for description). Right side of figure displays a plot of damage classification vs. distance upstream along transect route. Transect 3 (NE side of SJFZ) general shows higher damage class values compared to transect 4. Queried fault is the approximate location of the main SJFZ from Sharp (1967) and the USGS (2006). Fault F210 is relocated contact between the CVP and BVC from this study.

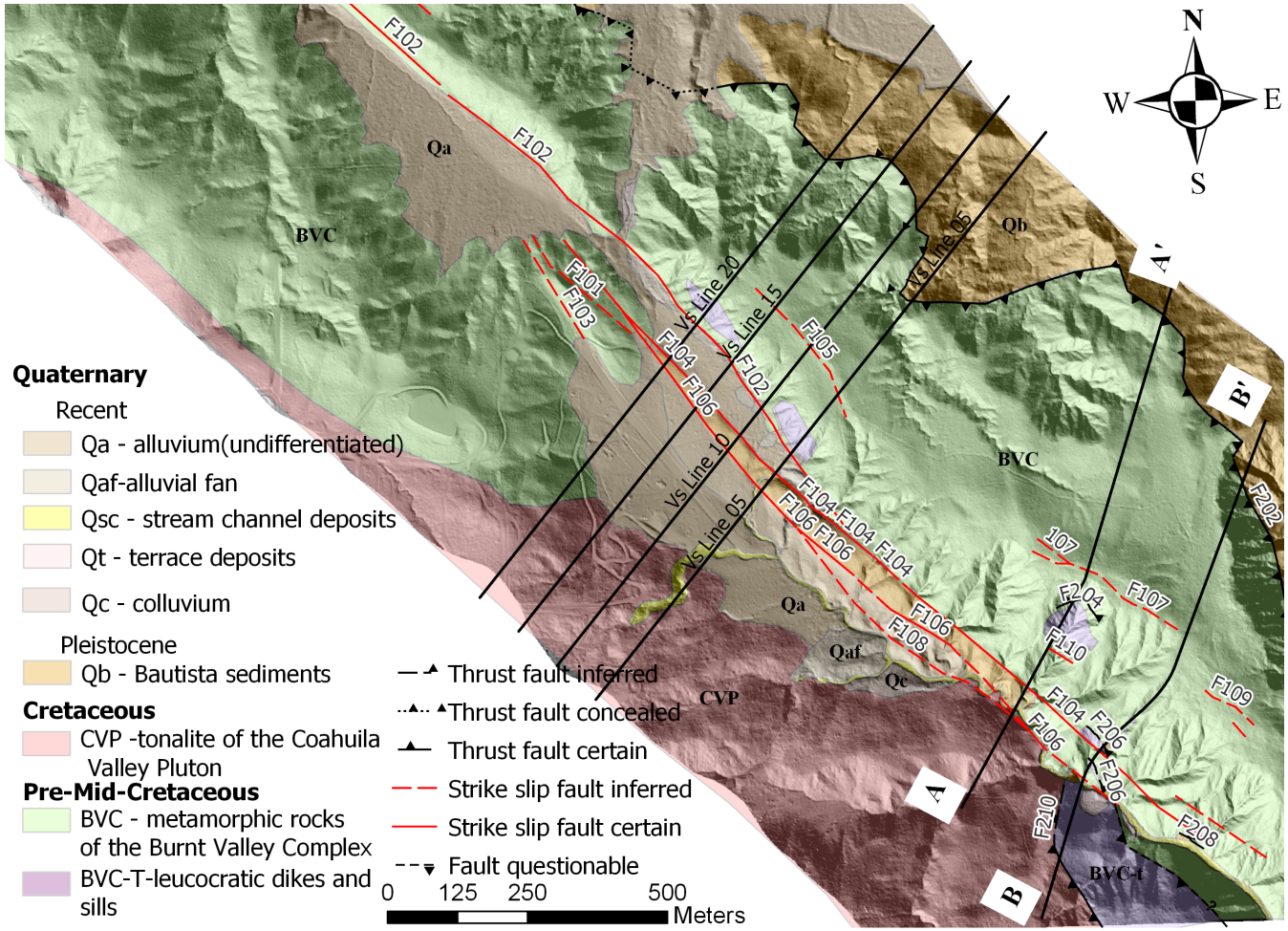

Figure 2-18: Portion of geologic map showing cross-section locations. Cross-sections A-A' and B-B' are based on mapping and structural measurements in Transects 1 through 2, and 3 through 4, illustrated found in figures 2-20 and 2-21, respectively. Cross-sections lines Vs-05, -10, -15, and -20 represent 2D depth slices of the 3D Vs model (Mordret et al., 2018) used for making geologic interpretations found in figures 2-22 through 2-26.

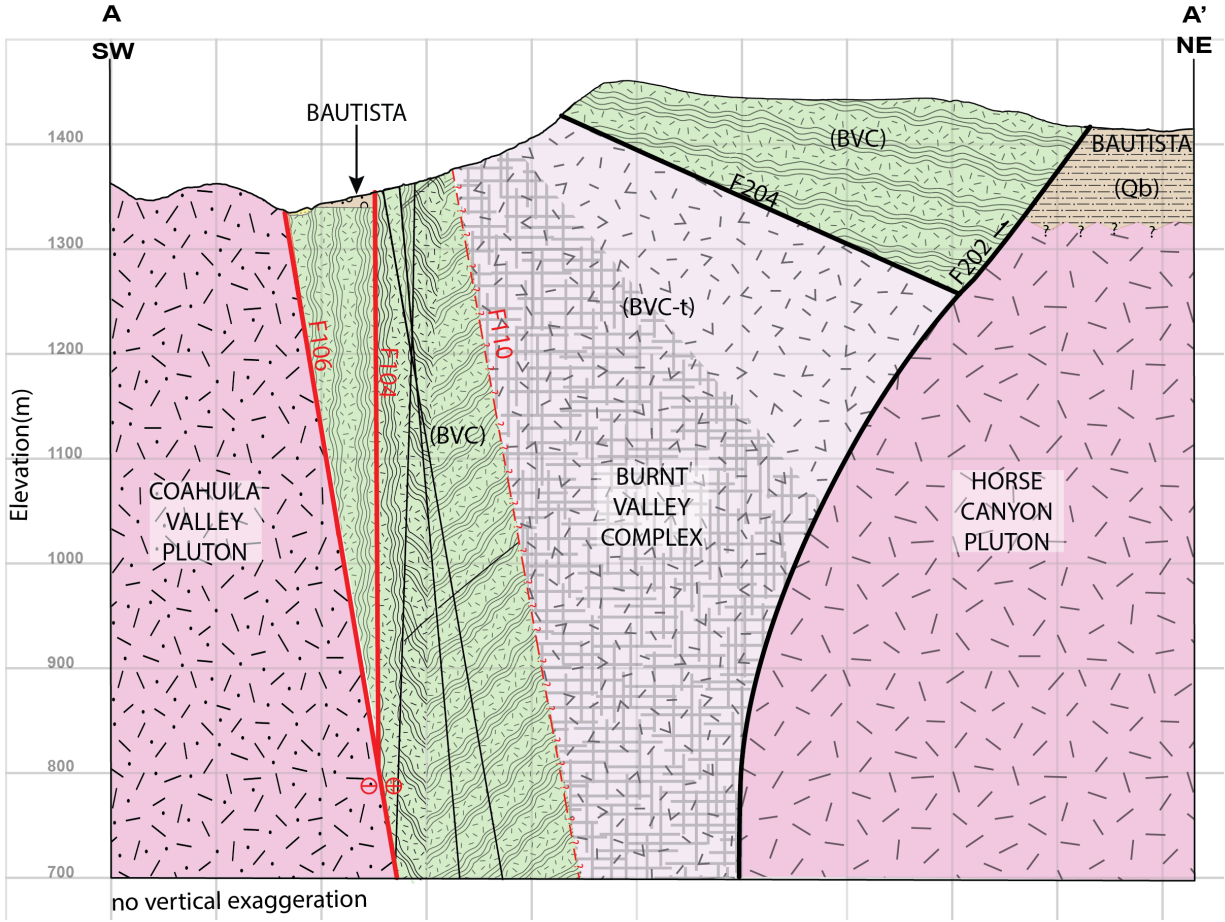

Figure 2-19: Geologic cross-section A to A'a) Cross-section illustration incorporating geologic and structural data from Transects 1 and 2. Swatch pattern within BVC based on foliation measurements. Red lines (F104 and F106)indicate the main CF. Thick black lines represent mapped fault traces with no topographic signature (F202 and F204). Thin black lines indicate thin faults observed in Transect 1. Red dashed line represents contact with leucocratic dike. Hash pattern in Burnt Valley Complex denotes portions of intense fracturing and partially pulverized rock observed at the surface.

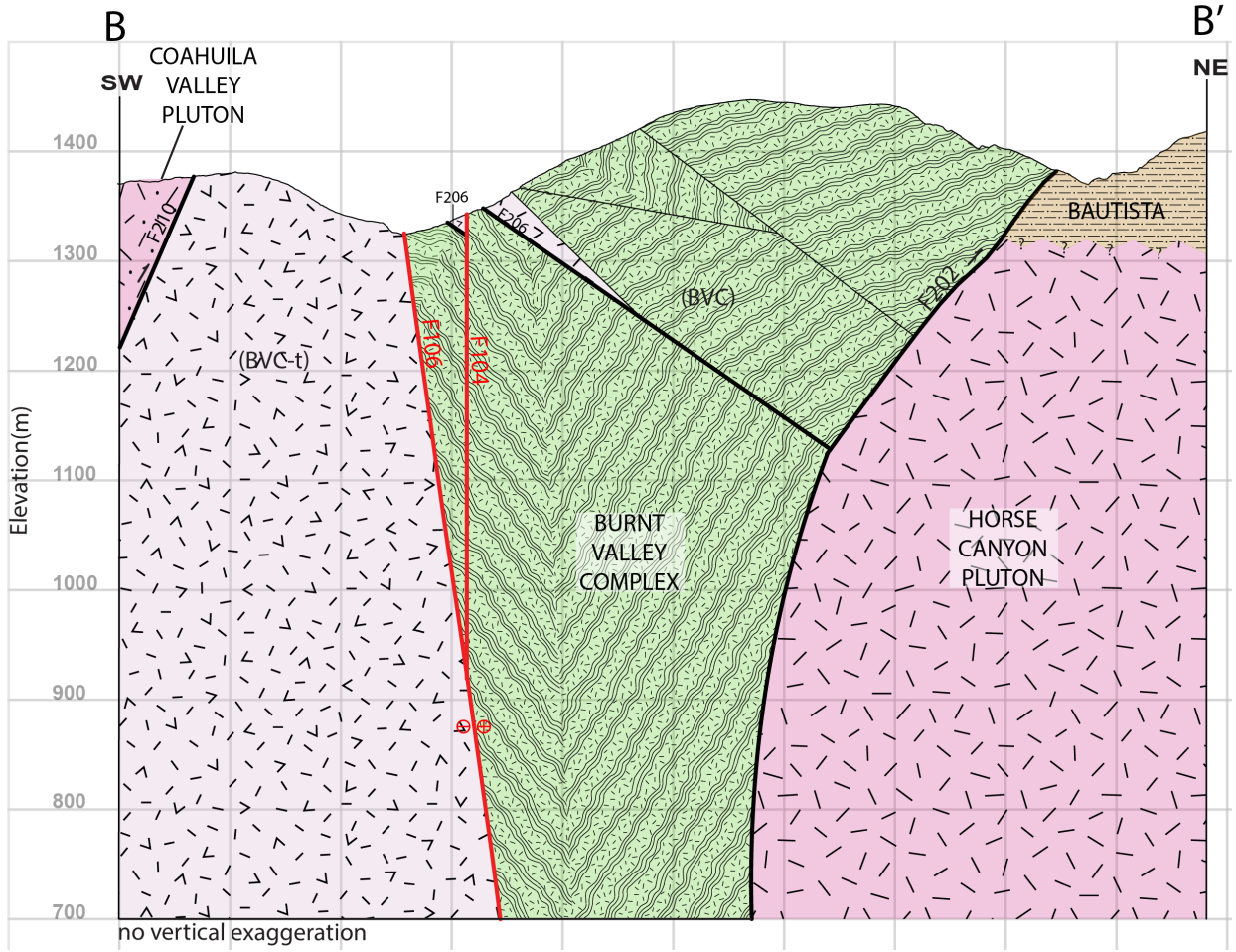

Figure 2-20: Geologic cross-section B to B'. a) Cross-section illustration incorporating geologic and structural data from Transects 3 and 4. Swatch pattern within BVC based on foliation measurements. Red lines (F104 and F106) indicate the main CF. Thick black lines represent mapped fault traces with no topographic signature (F202 and F204). Thin black lines indicate thin faults observed in Transect 1. Red dashed line represents contact with leucocratic dike.

Cross Section Vs Line 05

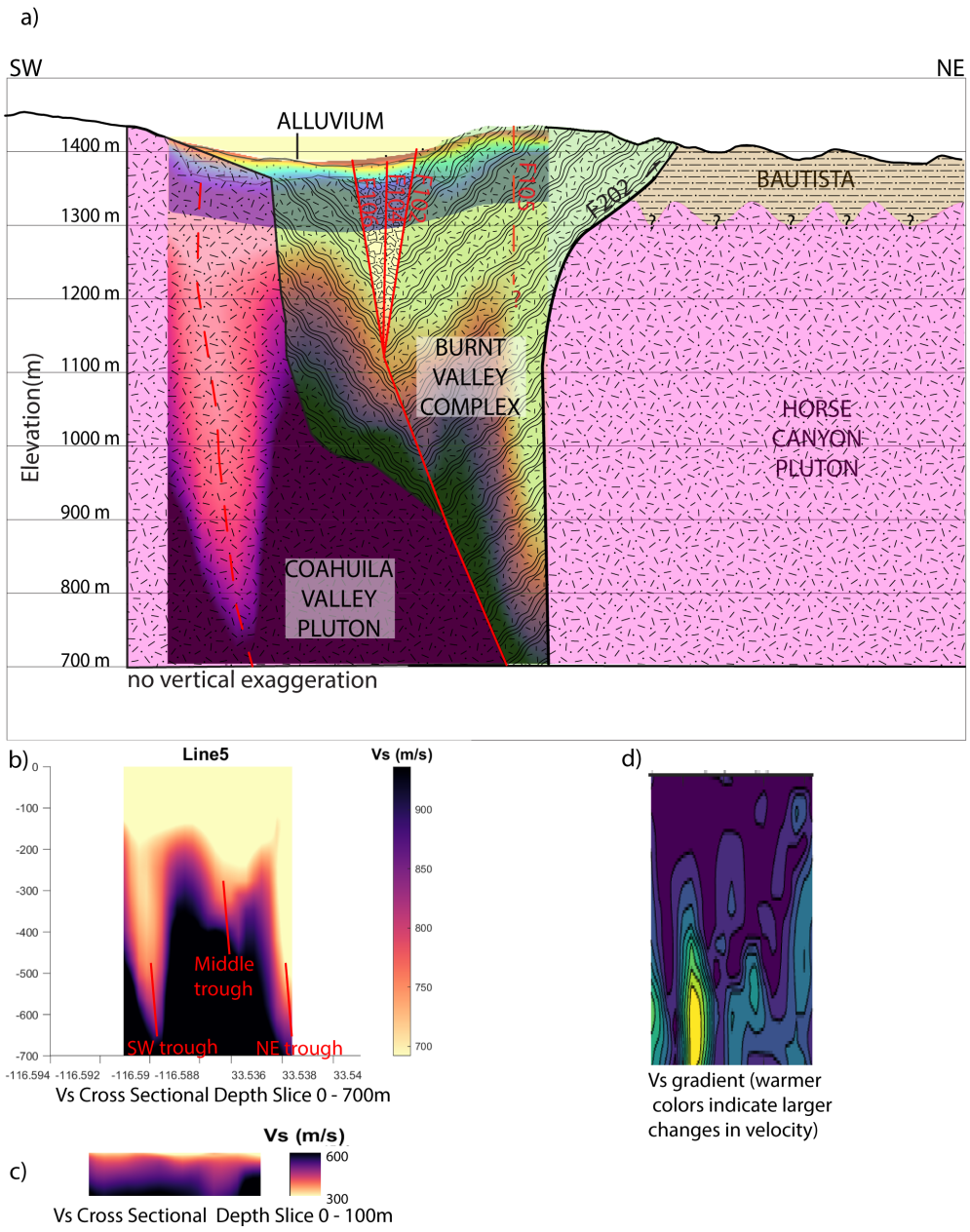

Figure 2-21: Geologic Cross-section Vs Line 05. a) Interpretive cross section incorporating geologic mapping from this study and depth slice from 3D Vs model (Mordret et al., 2018). b) Vs depth slice from 3D Vs model extending from ground surface to 700 m. c) Vs depth slice from 3D Vs model extending from ground surface to 100 m. d) Gradient depth map based on a. Warmer colors indicate areas with greater velocity contrast (e.g., yellow patch adjacent to low velocity trough on SW of a and b.

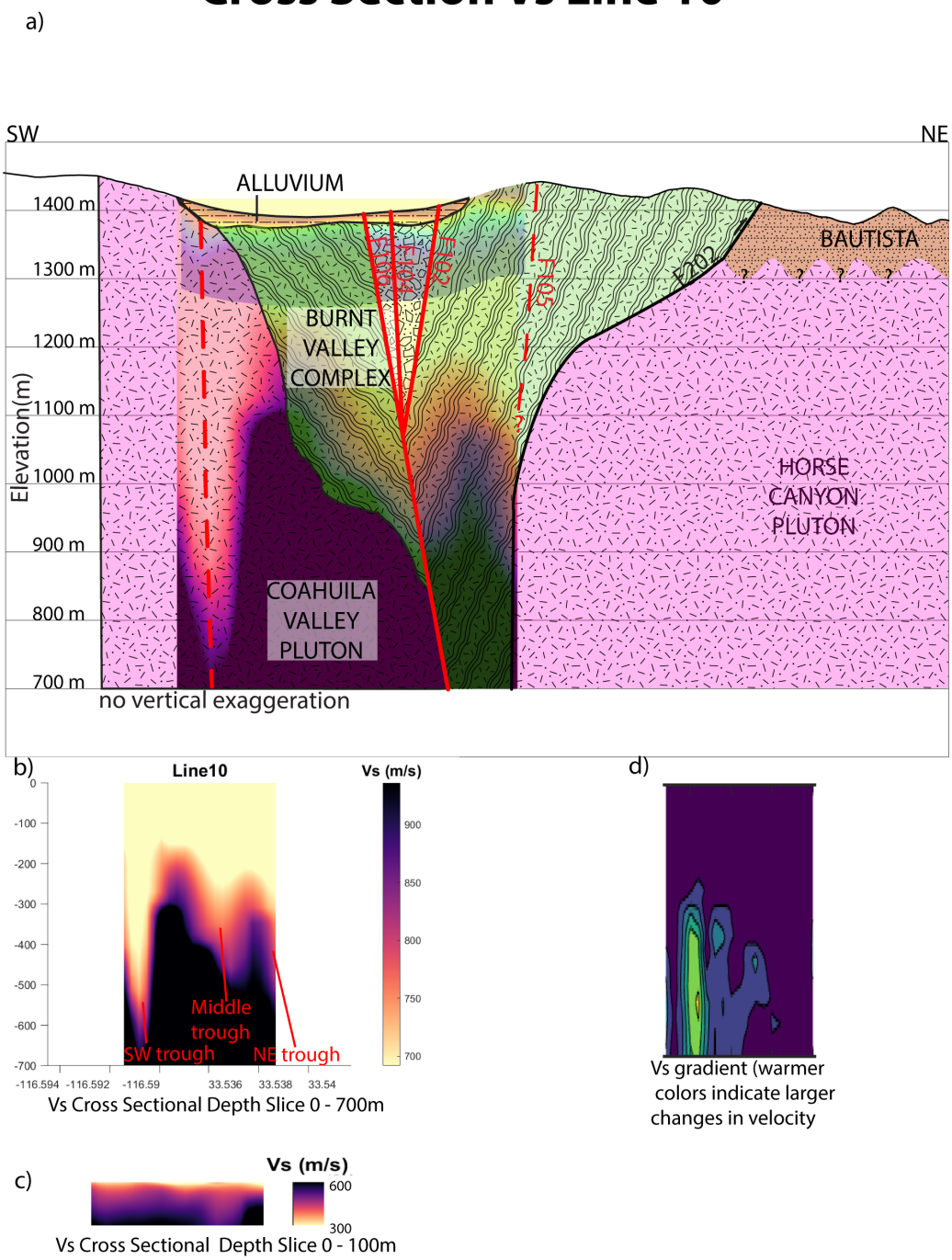

Figure 2-22: Geologic cross-section Vs Line 10. a) Interpretive cross section incorporating geologic mapping from this study and depth slice from 3D Vs model (Mordret et al., 2018). b) Vs depth slice from 3D Vs model extending from ground surface to 700 m. c) Vs depth slice from 3D Vs model extending from ground surface to 100 m. d) Gradient depth map based on a. Warmer colors indicate areas with greater velocity contrast (e.g. yellow patch adjacent to low velocity trough on SW of a and b.

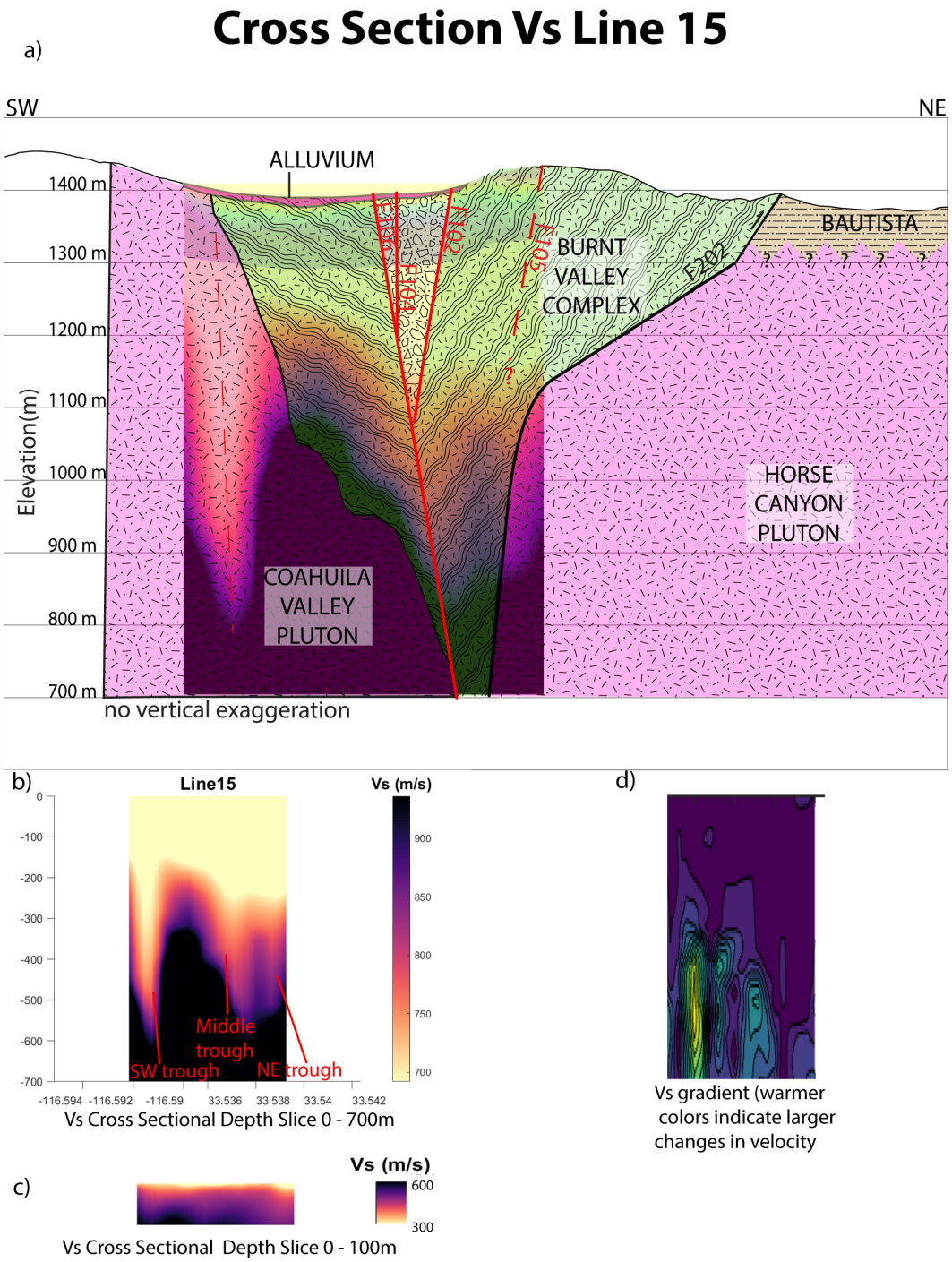

Figure 2-23: Geologic cross-section Vs Line 15: a) Interpretive cross section incorporating geologic mapping from this study and depth slice from 3D Vs model (Mordret et al., 2018). b) Vs depth slice from 3D Vs model extending from ground surface to 700 m. c) Vs depth slice from 3D Vs model extending from ground surface to 100 m. d) Gradient depth map based on a. Warmer colors indicate areas with greater velocity contrast (e.g. yellow patch adjacent to low velocity trough on SW of a and b.

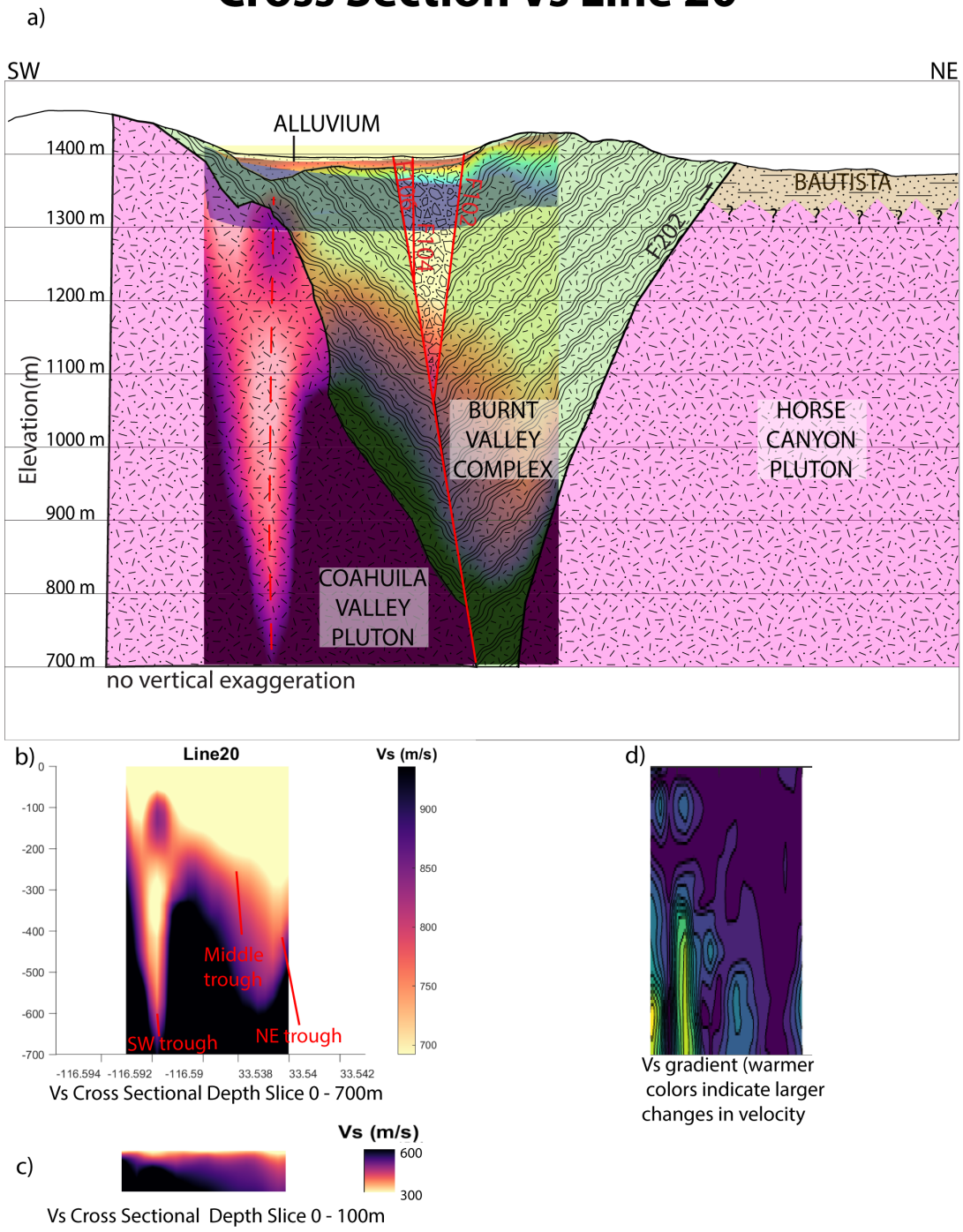

Figure 2-24: Geologic cross-section Vs Line 20: a) Interpretive cross section incorporating geologic mapping from this study and depth slice from 3D Vs model (Mordret et al., 2018). b) Vs depth slice from 3D Vs model extending from ground surface to 700 m. c) Vs depth slice from 3D Vs model extending from ground surface to 100 m. d) Gradient depth map based on a. Warmer colors indicate areas with greater velocity contrast (e.g. yellow patch adjacent to low velocity trough on SW of a and b.

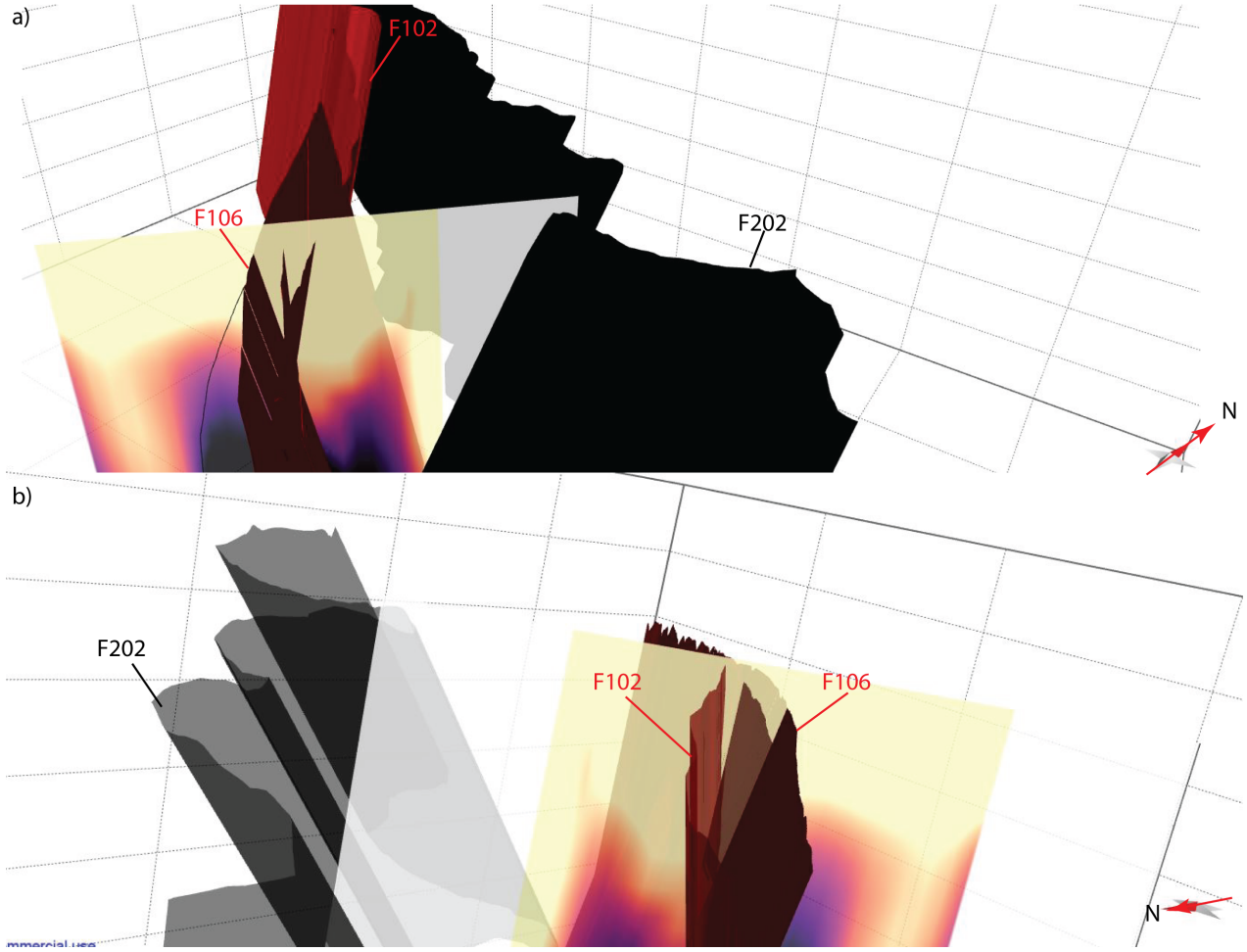

Figure 2-25: 3D fault zone model. Model of fault zone at SGB based on surface observations showing depth slice from Vs line 05 (developed from 3D-Vs model from Mordret et al., 2018). a) 3D fault zone model centered on SGB basin view towards NW, black plane (ride side) represents fault trace F202. Three main fault traces F102, F104 and F06 illustrated on left side of figure. b) 3D fault zone model centered on SGB basin view towards SE, black plane (left side) represents fault trace F202. Three main fault traces F102, F104 and F06 illustrated on right side of figure

CHAPTER 3

DISCUSSION AND CONCLUSIONS

The results described in Chapter 2 include observations from geologic mapping and site excavation, rock damage survey, displacement measurements, and a model of subsurface geology and fault zone structure. A first order assessment of these observations are heterogeneity of structural properties and damage intensity and extent. Discussed below are the implications of these findings on local earthquake mechanisms.

3.1 Discussion

Characterizing fault zones and geologic structures are key elements to understanding earthquake processes. The focus of this study is to synthesize field based observations with interpretations from shallow seismic velocity data (Mordret et al., 2018) for a fault spanning volume. This section presents a synthesis with discussions on excavation observations, fault trace mapping and displacement measurements, controls on damage extent and asymmetry, and the proposed geologic model.

3.1.1 Excavation Stratigraphy and Structure

The geologic units that bound the edges of the trench, units 100 through 103, are part of the young basin fill (alluvium) actively eroding from the hillsides and depositing across the valley floor. Samples of charcoal and soil were recovered from the NE end of the excavation within the younger alluvium, however, dating these material is beyond the scope of this project. Nonetheless, the general lack of soil structure and clay development, and poor consolidation are indicative of young material recently deposited during the Holocene.

The clast-rich material constituting the interior of the ridge and excavation, units 200 through 205) are ambiguous. Based on previous mapping (Sharp, 1967) as well as the stiff consistency and numerous large metamorphic clasts at the ridge surface, hard rock was anticipated in the near subsurface. During excavation of the trench at the NE edge, this expectation was initially thought correct based on the laborious digging efforts of the backhoe machine, and exposed rock mass. The weathering of the observed rock within the excavation ranges from slightly weathered to completely decomposed. The clasts become relatively smaller towards the SE, however the weathering is fairly consistent. The low angle orangish-brown shear planes are coincident with surface trace mapping of F104. These observations could be suggestive of dip-slip movement along the fault which has uplifted basement rock along the shear planes to the surface. The disintegrated cobbles and boulders away from the fault representing part of the older deposits observed within Alkali Wash, with brittle deformation resulting from shearing and displacement during large earthquakes. Although the shallow dip of the shear planes seems inconsistent with the linear surface trace, changes in fault geometry at or near the surface are not uncommon. The lack of striations indicating a principle slip surface in such distinct planar features, and shallow shear wave velocity profiles with no near surface high values within the ridge does not support this hypothesis. The degree of clast fracturing and disintegration, chaotic clast orientation, no soil structure development, and obvious shear planes are most likely diagnostic of slope failure events. The lack of any landslide morphology near the trench suggests the material is derived from hillslope failures farther to the SW in the steeper slopes of Alkali Wash and displaced along the fault towards SGB. This material is therefore grouped with other sedimentary deposits observed to the

SE in Alkali Wash (Figure 2-6d) and NW of the SGB basin (Figure 2-6c) and mapped as a continuous unit of the Pleistocene age Bautista beds (Figure 2-4).

3.1.2 Fault Trace Mapping and Slip Distribution

Mapped fault traces in this study are based on strong geomorphic lineaments observed in the B4 lidar, offset geomorphic features, and/or field observations (Figure 2-8). The lack of continuity along strike of inferred faults (dashed lines in figure 2-8) F101 through F109 implies—if indeed these features are fault related—that they are secondary structures. North of SGB, fault traces F100 and F102 both form strong geomorphic lineaments. Based on measurements from Salisbury et al. (2012), the most recent earthquake included displacement along F102 and F104, on the SW side of the Burnt Valley Road cut and just NW of the SGB basin, respectively (Figure 2-9). Analogous displacement measurements from this study are observed on fault traces F106 and F108 within SGB, indicating slip is distributed relatively equally amongst the faults. Within Alkali Wash apparent displacement along fault trace F106 becomes less pronounced, suggesting slip occurs principally along F104 in that area. Previous mapping by Sharp (1967) traced the SJFZ primarily on the SE side of Alkali Wash as a thrust fault juxtaposing CVP over BVC. With the aid of high resolution DTM from B4 lidar, trace of the CF is realigned to multiple faults, F104 and F106, predominantly displaying strike-slip displacement.

3.1.3 Geologic Mapping, Surface Morphology and Rock Damage Asymmetry

Several studies of rock damage along the SJFZ, including geophysical observations (Lewis et al., 2005; Qiu et al., 2017; Qin et al., 2017; Share et al; 2017),

fault zone outcrop scale mapping (Dor et al., 2006), and DEM analysis (Wechsler et al., 2009) have suggested asymmetry could be resultant of preferred NW rupture propagation along a bi-material interface (Ben-Zion and Shi, 2005; Shi and Ben-Zion, 2006). The repeated occurrence of such ruptures is expected to produce greater damage on the side with faster seismic velocities (stiffer side). Another hypothesis suggests that damage extent along the SJFZ, in the shallow subsurface, is rheologically controlled (Peppard et al., 2018) based on surficial observations and microstructural analysis of Bautista sediments.

Rock damage asymmetry has been noted on other large strike slip fault systems within the SAF (Dor et al., 2006), along the North Anatolian Fault (NAF) in Turkey (Dor et al., 2008), and along the Arima-Takatsuki Tectonic Line (ATTL)in Japan (Mitchel et al., 2011). Dor et al. (2008) performed detailed mapping of fault zone damage and DEM morphometric analyses at both the 1943 and 1944 earthquake epicenters along the NAF. Resulting asymmetric properties including 1) damage accumulation within the fault zone, 2) stream erosion, and 3) drainage density values were identified at both locations leading Dor et al. (2008) to conclude the two locations experience preferred rupture propagation direction during large seismic events. The Hakusui-kyo outcrop along the ATTL, exposes the fault core and juxtaposition of rhyolite and granite the north and south of the fault respectively (Mitchell et al., 2011). Field mapping and thin section analysis of samples from the outcrop reveal both damage extent and intensity are much larger in the granitic rock. Results from the ATTL also indicate the rock pulverization is only observed within the granitic rock, which led Mitchell et al (2011) to conclude the asymmetry results from repeated fault ruptures in a preferred direction along the bi-material interface.

FZTW indicating a trapping structure in the top 1 km of the CF at SGB are localized between two mapped fault traces; F104 and F102 of this study (Figure 3-1). The portion of the map area outlined as the trapping structure is located below the alluvial cover within the SGB basin, however metamorphic outcrops surveyed on the NE slope do provide some exposure to damage extent. Figure 3-1 includes a kriging interpolation of damage intensity based on the survey points discussed in Section 2.8. The interpolation map is least representative of actual rock damage conditions in areas with sparse survey points, e.g. areas with large surface/soil cover, regolith, or vegetation. Numerous points were recovered near the trapping structures outlined by seismic waves (Ben-Zion et al., 2015; Qin et al., 2017), marking areas with intense damage. The rock damage survey and interpolation highlights the heterogeneity of damage intensity both along the fault and at distance from the fault. Such heterogeneity is also expected at depth and explains the confined shape of the trapping structure within the dense array data set.

Geologic mapping and morphometric analysis of SGB show subtle contrasts between the NE and SW portions of the study area. From the north end of the SGB basin southward, mapped rock units on opposite sides of the valley and Alkali Wash are both crystalline, but vary from metamorphic rock with strong foliations, fractures, leucocratic dikes and minor faults, to granitic rock with some fractures and occasional pegmatite dikes. Drainages and ridgelines formed into the NE and SW slopes are asymmetric with a general increase in drainage count and ridgeline steepness formed on slopes to the NE. In Alkali Wash the opposing ridgeline slopes also vary in both vegetation cover and aspect, with thicker vegetation on the N facing slopes (SW side). In the northern hemisphere north facing slopes are associated with more shade and therefore more water retention

which can affect the overlying soils and vegetation (e.g. Hicks and Frank, 1984). The thicker vegetation cover on the north facing slopes provide more stability and therefore some control on slope gradient. Results from this study, however, do correlate with those of the broader macroscale evaluation of drainage density values (Wechsler et al., 2009); higher values on the NE side of the CF. The best exposures of outcrops in Alkali Wash demonstrate, at outcrop scale, strongest dissimilarities between rock mass of opposing slopes are pre-existing flaws in the form of geologic structures (e.g. small faults, fractures, and foliations), and the degree of rock damage intensity. This correlation agrees with conclusions from Wechsler et al. (2009) that rock damage may exercise at least partial control of morphology adjacent to the fault.

Based on the model proposed in this study, within the upper roughly 700 m of 3D-Vs model (Mordret et al., 2018), higher velocity values occur within the tonalite plutonic rock, which in outcrops expresses far fewer flaws. Griffith et al. (2010) described the effect of fractures on effective stiffness of fault zone rocks through mapping, microstructural analysis and numerical simulations. The results reveal that reduction in rock mass stiffness from mesoscopic scale fractures can induce a greater material contrast than a bi-material interface. Therefore, if rheological properties exert dominant control of damage extent during earthquake ruptures, observations at SGB should be reversed, with higher intensities in the CVP. In an effort to explain how pulverized fault zone rocks can form from subshear ruptures, Xu and Ben-Zion (2016) examine the effects of pre-existing flaws on a rupture propagated along a bi-material interface using numerical simulations. Their model results demonstrate that activation of pre-existing flaws can govern the growth and extent of rock pulverization during dynamic

ruptures (Xu and Ben-Zion, 2016). This processes may help explain the high damage intensity observed within the leucocratic dike near the end of Transect 1.

Potential flaws within the rock mass observed in the field include foliations, fractures, and small faults. In the geologic model proposed in this study, fault trace F110 extends down dip, possibly connecting to other flaws in the rock mass (Figure 2-19). This subsurface network could allow for the growth and extension of pulverization and rock damage preferentially within the metamorphic rock of the BVC. Therefore, the rock mass damage distribution observed at SGB and the northern end of Alkali Wash is probably best explained through repeated NW uni-directional earthquake ruptures and growth/extension of damage intensity away from the fault through pre-existing flaws of the BVC.

3.1.4 Geologic and Fault Zone Model

The main seismogenic fault within the SGB basin as defined by Qin et al. (2018) is consistent with the geologic model proposed here (fault trace F106), and at depth demarks the transition between the CVP and BVC. The basis for this assertion is derived from the strong contrast in velocity observed in each depth slice produced from the 3D-Vs model (Mordret et al., 2018) (Figures 2-21 through 2=24). The overall NE dip of the fault zone structure within SGB is consistent with results from deeper geophysical data on the CF (Li and Vernon, 2001). This implies that geometry of the CF within the upper 500–700 m conforms to a similar orientation as observed deeper in the crust. The low velocity trough observed on the SW side of each Vs depth slice was previously interpreted as a sedimentary basin (Mordret et al., 2018). This interpretation does not seem plausible given its location within the basin, the overall shape, depth, and the

geologic mapping presented here. The SW low velocity trough is not directly below the basin, but farther to the basin edge and underneath the mapped tonalite of the SW slope. Secondly, the depth of the trough, between 500 m to 600 m, seems rather excessive for a less than 500 m wide basin. By comparison, elevation differences between the top and base of sediments filling the broader Burnt Valley measure roughly 300 m thick using the B4 lidar DEM. Lastly, UNAVCO (2010) boring B946 is coincident with the low velocity feature within the vicinity of Vs depth slice line 10 (Figure 2-22). Descriptions from the boring's cuttings and downhole data include granitic rocks at the surface, and fractured rock with clayey material between 400 ft and 500 ft depths; strong evidence the discontinuity denotes faulting. Connecting the feature to the greater structure of the SJFZ is possible according to along strike projection in Move (supplemental 3d fault model). The lack of topographic signature over the discontinuity, though, suggests either it does not breach the surface, or has not failed during recent earthquakes as would be expected by the lineaments and displacements within fault traces observed in the basin floor.

Producing three dimensional fault zone models are often produced by the petroleum industry to help characterize complex structures and illuminate potential hydrocarbon resources. 3D models of strike slip faults provide a unique and useful perspective particularly for understanding complexities and producing more accurate models for seismic hazard assessment. In Northern California, along the Hayward-Calaveras fault junction, a 3D model incorporating both surface mapping and deep seismic data, help constrain and visualize the connection between the complex fault surface traces down to seismogenic depths (Watt, 2007). Using high resolution seismic reflection data along the Hosgri fault zone allowed for correlation between strike-slip

fault mechanics, substrate deformation, and fluid migration (Kluesner and Brothers, 2016). In the southwestern Qaidam Basin, Cheng et al (2017) compiled both surface fault trace and structural mapping with seismic reflection data to help visualize a positive flower structure along the Huangshi structure in the northeastern Tibetan Plateau (Cheng et al., 2017). The fault zone model proposed in the study, based on surficial mapping and observations, as well as interpretations from 3D-Vs depth slice, illustrate the CF in SGB (within upper 700 m) and northern portion of Alkali Wash is a complex system consisting of multiple fault strands. Geometry of the fault zone dips steeply to the NE, conforming to similar conditions of the fault at depth (Li and Vernon, 2001).

3.2 Conclusions and Recommendations for Further Research

Results of this study include a geologic map of the SGB basin and surrounding area, a geologic model based on both surficial observations and 3D-Vs data (Mordret et al., 2018), transects, and map of rock damage distribution, displacement measurements of fault traces mapped from high resolution B4 lidar, and a synthetic 3D fault zone model. Surficial geology revealed in the geologic map traces consolidated sediments of the Bautista from Alkali Wash, through SGB, to the northern edge of the mapping area at Burnt Valley Road. These deposits are missing from previous maps and with dating and further analysis using them as a marker could help establish slip rates on faults imaged in the dense array data set.

The geologic and fault zone model proposed in this study, agrees with interpretations from seismic velocity models suggesting the SW fault trace at SGB (F106) is the main interface juxtaposing differing material types (BVC and CVP) at depth, and

the measured displacement corresponds to the most recent large earthquake defined by Salisbury et al. (2012). Distribution of rock damage at SGB and the northern portion of Alkali Wash is asymmetric about the fault trace. The highest damage intensity appears concentrated predominately on the NE side supporting the argument of preferred NW rupture propagation (Lewis et al., 2005, Dor et al., 2006; Yang et al., 2014; Qiu et al., 2017; Share et al; 2017; Qin et al., 2017). Pulverization expansion and growth through pre-existing flaws in the form of faults and fractures agrees with numerical simulations of fault damage growth (Xu and Ben-Zion, 2016).

Further analysis of subsurface geophysical and material properties of the trapping structure determined by FZTW (Ben-Zion et al., 2015; Qin et al., 2017) would greatly improve understanding of fault zone complexity. Surface observations and shallow excavations may not provide the best representable sample set to fully characterize this structure which may play an influential role in earthquake propagation. Collecting core samples for laboratory testing, downhole large diameter geological borings and in-situ geophysical measurements would provide valuable information to improve both characterization of the structure, and validation of the geologic model presented in this research.

3.3 References

Ben-Zion, Y., and Shi, Z., 2005, Dynamic rupture on a material interface with spontaneous generation of plastic strain in the bulk: Earth and Planetary Science Letters, v. 236, p. 486-496.

Ben-Zion, Y., Vernon, F.L., Ozakin, Y., Zigone, D., Ross, Z.E., Meng, H., White, M., Reyes, J., Hollis, D., and Barklage, M., 2015, Basic data features and results from a spatially dense seismic array on the San Jacinto fault zone: Geophysical Journal International, v. 202, p. 370-380.

Cheng, X., Zhang, Q., Yu, X., Du, W., Liu, R., Bian, Q., Wang, Z., Zhang, T., and Guo, Z., 2017, Strike-slip fault network of the Huangshi structure, SW Qaidam Basin: Insights from surface fractures and seismic data: Journal of Structural Geology, v. 94, p. 1-12.

Dor, O., Rockwell, T., and Ben-Zion, Y., 2006, Geological Observations of Damage Asymmetry in the Structure of the San Jacinto, San Andreas and Punchbowl Faults in Southern California: A Possible Indicator for Preferred Rupture Propagation Direction: Pure and Applied Geophysics, v. 163, p. 301-349.

Dor, O., Yildirim, C., Rockwell, T.K., Ben-Zion, Y., Emre, O., Sisk, M., and Duman, T.Y., 2008, Geological and geomorphologic asymmetry across the rupture zones of the 1943 and 1944 earthquakes on the North Anatolian Fault: possible signals for preferred earthquake propagation direction: Geophysical Journal International, v. 173, p. 483-504.

Hicks, R.R., and Frank, P.S., 1984, Relationship of aspect to soil nutrients, species importance and biomass in a forested watershed in West Virginia: Forest Ecology and Management, v. 8, p. 281-291.

Griffith, W.A., Sanz, P.F., and Pollard, D.D., 2010, Influence of Outcrop Scale Fractures on the Effective Stiffness of Fault Damage Zone Rocks, *in* Ben-Zion, Y. and Sammis, C., eds., Mechanics, Structure and Evolution of Fault Zones: Basel, BirkhÃ¤user Basel, p. 1595-1627.

Kluesner, J.W., and Brothers, D., 2016, Seismic attribute detection of faults and fluid pathways within an active strike-slip shear zone: New insights from high-resolution 3D P-Cable (TM) seismic data along the Hosgri Fault, offshore California: Interpretation-A Journal of Subsurface Characterization, v. 4, p. SB131-SB148.

Lewis, M.A., Peng, Z., Ben-Zion, Y., and Vernon, F.L., 2005, Shallow seismic trapping structure in the San Jacinto fault zone near Anza, California: Geophysical Journal International, v. 162, p. 867-881.

Li Y., and Vernon, F.L., 2001, Characterization of the San Jacinto fault zone near Anza, California, by fault zone trapped waves: Journal of Geophysical Research: Solid Earth, v. 106, p. 30671-30688.

Mitchell, T.M., Ben-Zion, Y., and Shimamoto, T., 2011, Pulverized fault rocks and damage asymmetry along the Arima-Takatsuki Tectonic Line, Japan: Earth and Planetary Science Letters, v. 308, p. 284-297.

Mordret, A., P. Roux, P. Boué and Y. Ben-Zion, 2018. Shallow 3-D structure of the San Jacinto Fault zone revealed from ambient noise imaging with a dense seismic array, Geophysical Journal International., in review.

Peppard, D.W., Webb, H.N., Dennis, K., Vierra, E., Girty, G.H., Rockwell, T.K., Blanton, C.M., Brown, J.F., Goldstein, A.I., Kastama, K.W., Korte-Nahabedian, M., Puckett, D., and Richter, A.K., 2018, Micro-scale damage characterized within part of a dismembered positive flower structure, San Jacinto fault, southern California, USA: Journal of Structural Geology, v. 112, p. 53-68.

Qin, L., Ben-Zion, Y., Qiu, H., Share, P., Ross, Z.E., and Vernon, F.L., 2017, Internal structure of the San Jacinto fault zone in the trifurcation area southeast of Anza, California, from data of dense seismic arrays: Geophysical Journal International, v. 213, p. 98-114.

Qiu, H., Ben-Zion, Y., Ross, Z.E., Share, P.-., and Vernon, F.L., 2017, Internal structure of the San Jacinto fault zone at Jackass Flat from data recorded by a dense linear array: Geophysical Journal International, v. 209, p. 1369-1388.

Salisbury, J.B., Rockwell, T.K., Middleton, T.J., and Hudnut, K.W., 2012, LiDAR and field observations of slip distribution for the most recent surface ruptures along the central San Jacinto Fault: Bulletin of the Seismological Society of America, v. 102, p. 598-619.

Share, P., Ben-Zion, Y., Ross, Z.E., Qiu, H., and Vernon, F.L., 2017, Internal structure of the San Jacinto fault zone at Blackburn Saddle from seismic data of a linear array: Geophysical Journal International, v. 210, p. 819-832.

Sharp, R.V., 1967, San Jacinto fault zone in the Peninsular Ranges of Southern California: Geological Society of America Bulletin, v. 78, p. 705-729.

Shi, Z., and Ben-Zion, Y., 2006, Dynamic rupture on a bimaterial interface governed by slip-weakening friction: Geophysical Journal International, v. 165, p. 469-484.

UNAVCO, 2010, San Jacinto Fault Zone at Anza B946 sagebf946bcs2010, Unpublished Installation Report.

Watt, J.T., Graymer, R.W., Simpson, R.W., Ponce, D.A., Jachens, R.C., Phelps, G.A., and Wentworth, C.M., 2007, A Three-dimensional geologic model of the Hayward-Calaveras Fault junction: Eos Trans. AGU, v. 88, no. 52, Fall Meet. Suppl.

Wechsler, N., Rockwell, T.K., and Ben-Zion, Y., 2009, Application of high resolution DEM data to detect rock damage from geomorphic signals along the central San Jacinto Fault: Geomorphology, v. 113, p. 82-96.

Xu, S., and Ben-Zion, Y., 2017, Theoretical constraints on dynamic pulverization of fault zone rocks: Geophysical Journal International, v. 209, p. 282–296.

Yang, H., Li, Z., Peng, Z., Ben-Zion, Y., and Vernon, F., 2014, Low-velocity zones along the San Jacinto Fault, Southern California, from body waves recorded in dense linear arrays: Journal of Geophysical Research: Solid Earth, v. 119, p. 8976-8990.

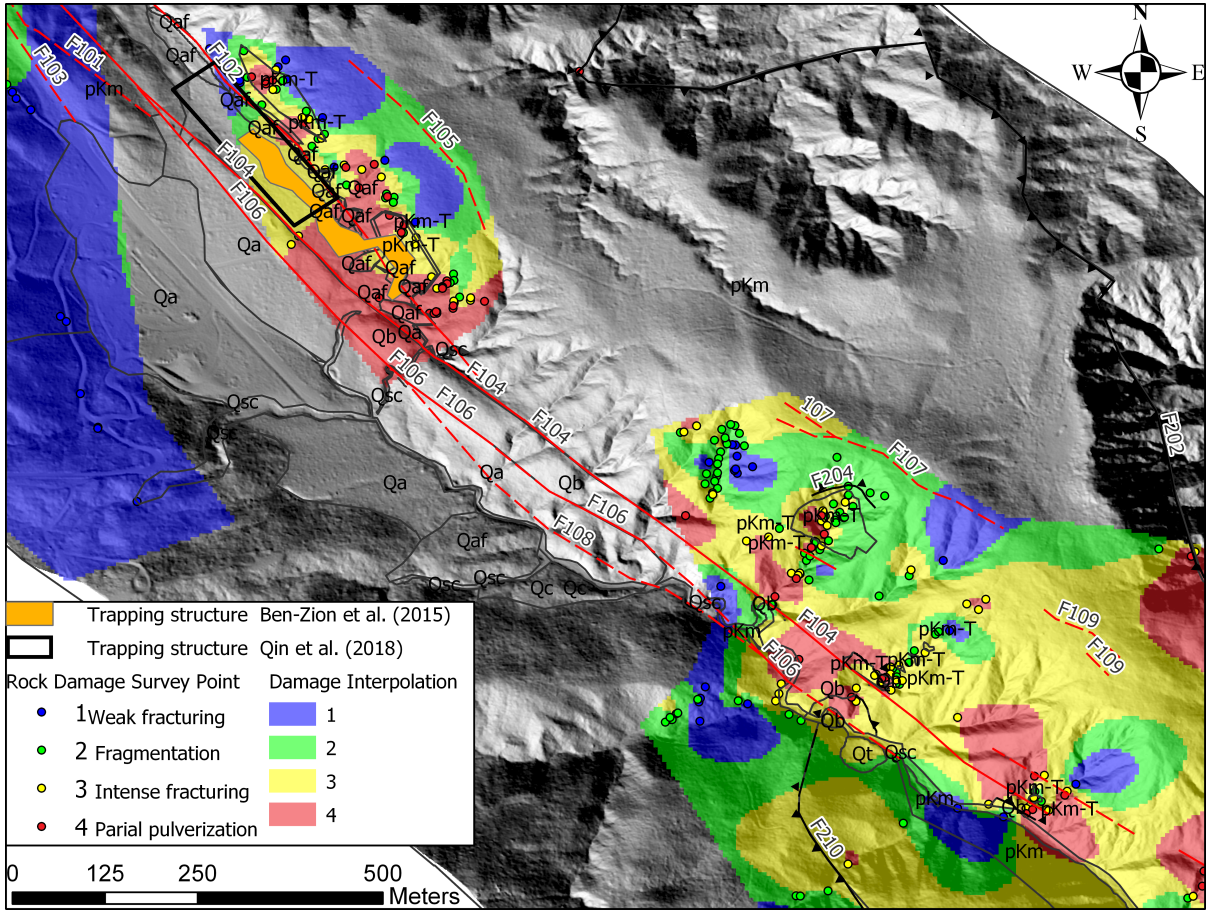

Figure 3-1: SGB rock damage interpolation map. Clipped extent of the SGB basin and Alkali Wash with rock damage survey points color coded to damage intensity classifications based on Dor et al. (2006) found in Table 4. Outlines of geologic map units are drawn in black lines and fault traces as red and black lines with teeth indicating dip direction. Kriging of rock damage indicated by blue, green, yellow and red colors corresponding to increased values of damage intensity. Highest damage intensity is primarily observed on the NE side of the mapped area and CF structure. Damage interpolation is least represented in areas with sparse survey points (e.g. steep slopes, thick soil cover and/or dense vegetation)

REFERENCES

Aben, F.M., Doan, M.-., Gratier, J.-., and Renard, F., 2017, High strain rate deformation of porous sandstone and the asymmetry of earthquake damage in shallow fault zones: Earth and Planetary Science Letters, v. 463, p. 81-91.

Allam, A.A., Ben-Zion, Y., Kurzon, I., and Vernon, F., 2014, Seismic velocity structure in the Hot Springs and Trifurcation areas of the San Jacinto fault zone, California, from double-difference tomography: Geophysical Journal International, v. 198, p. 978-999.

Bemis, S.P., Micklethwaite, S., Turner, D., James, M.R., Akciz, S., Thiele, S.T., and Bangash, H.A., 2014, Ground-based and UAV-Based photogrammetry: A multi-scale, high-resolution mapping tool for structural geology and paleoseismology: Journal of Structural Geology, v. 69, p. 163-178.

Bennett, R.A., Friedrich, A.M., and Furlong, K.P., 2004, Codependent histories of the San Andreas and San Jacinto fault zones from inversion of fault displacement rates: Geology (Boulder), v. 32, p. 961-964

Ben-Zion, Y., 1998, Properties of seismic fault zone waves and their utility for imaging low-velocity structures: Journal of Geophysical Research: Solid Earth, v. 103, p. 12567-12585.

Ben-Zion, Y., and Shi, Z., 2005, Dynamic rupture on a material interface with spontaneous generation of plastic strain in the bulk: Earth and Planetary Science Letters, v. 236, p. 486-496.

Ben-Zion, Y., Vernon, F.L., Ozakin, Y., Zigone, D., Ross, Z.E., Meng, H., White, M., Reyes, J., Hollis, D., and Barklage, M., 2015, Basic data features and results from a spatially dense seismic array on the San Jacinto fault zone: Geophysical Journal International, v. 202, p. 370-380.

Bevis, M., K. Hudnut, R. Sanchez, C. Toth, D. Grejner-Brzezinska, E. Kendrick, D. Caccamise, D. Raleigh, H. Zhou, S. Shan, (2005). The B4 project: Scanning the San Andreas and San Jacinto fault zones, Eos Trans. AGU 86, no. 52 (Fall Meet. Suppl.), H34B–01.

Brown, N.N., Fuller, M.D., and Sibson, R.H., 1991, Paleomagnetism of the Ocotillo Badlands, southern California, and implications for slip transfer through an antidilational fault jog: Earth and Planetary Science Letters, v. 102, p. 277-288.

Caine, J., Evans, J., and Forster, C., 1996, Fault zone architecture and permeability structure: Geology, v. 24, p. 1025-1028.

Cheng, X., Zhang, Q., Yu, X., Du, W., Liu, R., Bian, Q., Wang, Z., Zhang, T., and Guo, Z., 2017, Strike-slip fault network of the Huangshi structure, SW Qaidam Basin: Insights from surface fractures and seismic data: Journal of Structural Geology, v. 94, p. 1-12.

Chester, F., Evans, J.P., and Biegel, R., 1993, Internal Structure and Weakening Mechanism of the San Andreas Fault: Journal of Geophysical Research-Solid Earth, v. 98, p. 771-786.

Chester,F.M., Chester, J.S., Kirschner, D.L., Schulz, S.E., Evans, J.P., 2004, Structure of large-displacement, strike-slip fault zones in the brittle continental crust, *in Karner, G.D., et al.,* Rhyology and Deformation in the Lithosphere at Continental Margins: New York, Columbia University Press, p.223-260.

Cotton, F., and Coutant, O., 1997, Dynamic stress variations due to shear faults in a plane-layered medium: Geophysical Journal International, v. 128, p. 676-688.

Crowell, J.C., 1962, Displacement Along the San Andreas Fault, California, *in* Crowell, J.C., ed., Displacement Along the San Andreas Fault, California: Geological Society of America.

DiPietro, J.A., 2013, Chapter 17 - California Transpressional System, *in* DiPietro, J.A., ed., Landscape Evolution in the United States: Boston, Elsevier, p. 281-305.

Doan,M.L., Gary,G, 2009, Rock pulverization at high strain rate near the San Andreas fault: Nature Geoscience, v. 2, p. 709.

Dor, O., Rockwell, T., and Ben-Zion, Y., 2006, Geological Observations of Damage Asymmetry in the Structure of the San Jacinto, San Andreas and Punchbowl Faults in Southern California: A Possible Indicator for Preferred Rupture Propagation Direction: Pure and Applied Geophysics, v. 163, p. 301-349.

Dor, O., Yildirim, C., Rockwell, T.K., Ben-Zion, Y., Emre, O., Sisk, M., and Duman, T.Y., 2008, Geological and geomorphologic asymmetry across the rupture zones of the 1943 and 1944 earthquakes on the North Anatolian Fault: possible signals for preferred earthquake propagation direction: Geophysical Journal International, v. 173, p. 483-504.

Dor, O., Chester, J., Ben-Zion, Y., Brune, J., and Rockwell, T., 2009, Characterization of Damage in Sandstones along the Mojave Section of the San Andreas Fault: Implications for the Shallow Extent of Damage Generation: Pure and Applied Geophysics, v. 166, p. 1747-1773.

Frick, C., 1921, Extinct vertebrate faunas of the Badlands of Bautista Creek and San Timoteo Cañon, Southern California: Berkeley: University of California Press.

Graham, S., and Stanley, R., 1989, Oligocene and Miocene Paleogeography of Central California and Displacement Along the San Andreas Fault: Geological Society of America. Geological Society of America Bulletin, v. 101, p. 711.

Gray, B., Graehl, N., Bozkurt, S., Baldwin, J., and Clahan, K., 05/30, Seamless Photomosaic Trench Logging Using Trench-Based Photogrammetry Methods: Workflow and Case-Studies, *in* 7th International INQUA Meeting on Paleoseismology, Active Tectonics and Archeoseismology (PATA) Crestone, Colorado, p. 4.

Griffith, W.A., Sanz, P.F., and Pollard, D.D., 2010, Influence of Outcrop Scale Fractures on the Effective Stiffness of Fault Damage Zone Rocks, *in* Ben-Zion, Y. and Sammis, C., eds., Mechanics, Structure and Evolution of Fault Zones: Basel, BirkhÃ¤user Basel, p. 1595-1627.

Haddon, E. K., C. B. Amos, O. Zielke, A. S. Jayko, and R. Buergmann (2016), Surface Slip During the Large Owens Valley Earthquake, G-cubed.

Hatem, A.E., Cooke, M.L., and Toeneboehn, K., 2017, Strain localization and evolving kinematic efficiency of initiating strike-slip faults within wet kaolin experiments: Journal of Structural Geology, v.101, p. 96–108.

Hicks, R.R., and Frank, P.S., 1984, Relationship of aspect to soil nutrients, species importance and biomass in a forested watershed in West Virginia: Forest Ecology and Management, v. 8, p. 281-291.

Igel, H., Ben-Zion, Y. & Leary, P., 1997. Simulation of SH and P SV wave propagation in fault zones: Geophysical Journal International, v. 128, p. 533–546.

Johnson, K., Nissen, E., Saripalli, S., Arrowsmith, J R., McGarey, P., Scharer, K., Williams, P., Blisniuk, K., 2014, Rapid mapping of ultra-fine fault zone topography with Structure from Motion, Geosphere, v. 10; no. 5; p. 1-18.

King, G., Stein, R., and Lin, J., 1994, Static stress changes and the triggering of earthquakes: Bulletin of the Seismological Society of America, v. 84, p. 935-953.

Kluesner, J.W., and Brothers, D., 2016, Seismic attribute detection of faults and fluid pathways within an active strike-slip shear zone: New insights from high-resolution 3D P-Cable (TM) seismic data along the Hosgri Fault, offshore California: Interpretation-A Journal of Subsurface Characterization, v. 4, p. SB131-SB148.

Krummenacher, D., Gastil, R., Bushee, J., and Doupont, J., 1975, K-Ar Apparent Ages, Peninsular Ranges Batholith, Southern California and Baja California: Bulletin of the Geological Society of America, v. 86, p. 760-768.

Lewis, M.A., Peng, Z., Ben-Zion, Y., and Vernon, F.L., 2005, Shallow seismic trapping structure in the San Jacinto fault zone near Anza, California: Geophysical Journal International, v. 162, p. 867-881.

Li Y., and Vernon, F.L., 2001, Characterization of the San Jacinto fault zone near Anza, California, by fault zone trapped waves: Journal of Geophysical Research: Solid Earth, v. 106, p. 30671-30688.

Li, Q., and Liu, M., 2007, Initiation of the San Jacinto Fault and its Interaction with the San Andreas Fault: Insights from Geodynamic Modeling: Pure and Applied Geophysics, v. 164, p. 1937-1945.

Lin, A., and Yamashita, K., 2013, Spatial variations in damage zone width along strike-slip faults: An example from active faults in southwest Japan: Journal of Structural Geology, v. 57, p. 1-15.

Lundgren, P., E. A. Hetland, Z. Liu, and E. J. Fielding (2009), Southern San Andreas-San Jacinto fault system slip rates estimated from earthquake cycle models constrained by GPS and interferometric synthetic aperture radar observations, Journal of Geophysical Research, v. 114.

Lutz, A., Dorsey, R., Housen, B.A., and Janecke, S., 2006, Stratigraphic record of Pleistocene faulting and basin evolution in the Borrego Badlands, San Jacinto fault zone, Southern California: Geological Society of America Bulletin, v. 118, p. 1377-1397.

Matthews III, Vincent. 1976, Correlation of Pinnacles and Neenach Volcanic Formations and Their Bearing on San Andreas Fault Problem: AAPG Bulletin. v. 60, p. 2128-2141.

Matti, J.C., and Morton, D.M., 1993, Chapter 2: Paleogeographic evolution of the San Andreas fault in southern California: A reconstruction based on a new cross-fault correlation: Memoir of the Geological Society of America, v. 178, p. 107-159.

Meade, B. J., and B. H. Hager (2005), Block models of crustal motion in southern California constrained by GPS measurements, Journal of Geophysical Research, v.110.

Meng, H., and Ben-Zion, Y., 2017, Detection of small earthquakes with dense array data: example from the San Jacinto fault zone, southern California: Geophysical Journal International, v. 212, p. 442-457.

Miggins, D.P., Premo, W.R., Snee, L.W., Yeoman, R., Naeser, N.D., Naeser, C.W., and Morton, D.M., 2014, Thermochronology of Cretaceous batholithic rocks in the northern Peninsular Ranges batholith, southern California: Implications for the Late Cretaceous tectonic evolution of southern California, in Morton, D.M. and Miller, F.K., eds.,

Peninsular Ranges Batholith, Baja California and Southern California: Geological Society of America.

Mitchell, T.M., and Faulkner, D.R., 2009, The nature and origin of off-fault damage surrounding strike-slip fault zones with a wide range of displacements: A field study from the Atacama fault system, northern Chile: Journal of Structural Geology, v. 31, p. 802-816.

Mitchell, T.M., Ben-Zion, Y., and Shimamoto, T., 2011, Pulverized fault rocks and damage asymmetry along the Arima-Takatsuki Tectonic Line, Japan: Earth and Planetary Science Letters, v. 308, p. 284-297.

Molnar, P., Anderson, R.S., Anderson,S.P., 2007, Tectonics, fracturing of rock, and erosion: Journal of Geophysical Research: Earth Surface, v. 112.

Mordret, A., P. Roux, P. Boué and Y. Ben-Zion, 2018. Shallow 3-D structure of the San Jacinto Fault zone revealed from ambient noise imaging with a dense seismic array, Geophysical Journal International., in review

Morton, N., Girty, G.H., and Rockwell, T.K., 2012, Fault zone architecture of the San Jacinto fault zone in Horse Canyon, southern California: A model for focused post-seismic fluid flow and heat transfer in the shallow crust: Earth and Planetary Science Letters, v. 329-330, p. 71-83.

Okubo, C.H., and Schultz, R.A., 2005, Evolution of damage zone geometry and intensity in porous sandstone: insight gained from strain energy density: Journal of the Geological Society, v. 162, p. 939-949.

Peacock, D.C.P., Nixon, C.W., Rotevatn, A., Sanderson, D.J., and Zuluaga, L.F., 2016, Glossary of fault and other fracture networks: Journal of Structural Geology, v. 92, p. 12-29.

Peppard, D.W., Webb, H.N., Dennis, K., Vierra, E., Girty, G.H., Rockwell, T.K., Blanton, C.M., Brown, J.F., Goldstein, A.I., Kastama, K.W., Korte-Nahabedian, M., Puckett, D., and Richter, A.K., 2018, Micro-scale damage characterized within part of a dismembered positive flower structure, San Jacinto fault, southern California, USA: Journal of Structural Geology, v. 112, p. 53-68.

Peter, M., Anderson, R.S., and Anderson, S.P., 2007, Tectonics, fracturing of rock, and erosion: Journal of Geophysical Research: Earth Surface, v. 112.

Qin, L., Ben-Zion, Y., Qiu, H., Share, P., Ross, Z.E., and Vernon, F.L., 2017, Internal structure of the San Jacinto fault zone in the trifurcation area southeast of Anza, California, from data of dense seismic arrays: Geophysical Journal International, v. 213, p. 98-114.

Qiu, H., Ben-Zion, Y., Ross, Z.E., Share, P.-., and Vernon, F.L., 2017, Internal structure of the San Jacinto fault zone at Jackass Flat from data recorded by a dense linear array: Geophysical Journal International, v. 209, p. 1369-1388,

Reber, J.E., Lavier, L.L., and Hayman, N.W., 2015, Experimental demonstration of a semi-brittle origin for crustal strain transients: Nature Geoscience, v. 8, p. 712–715.

Rockwell, T., Loughman, C., and Merifield, P., 1990, Late Quaternary rate of slip along the San Jacinto Fault Zone near Anza, southern California: Journal of Geophysical Research: Solid Earth, v. 95, p. 8593-8605.

Rockwell, T., Dawson, T., Young Ben-Horin, J., and Seitz, G., 2015, A 21-Event, 4,000-Year History of Surface Ruptures in the Anza Seismic Gap, San Jacinto Fault, and Implications for Long-term Earthquake Production on a Major Plate Boundary Fault: Pure and Applied Geophysics, v. 172, p. 1143-1165.

Roux, P., Moreau, L., Lecointre, A., Hillers, G., Campillo, M., Ben-Zion, Y., Zigone, D., and Vernon, F., 2016, A methodological approach towards high-resolution surface wave imaging of the San Jacinto Fault Zone using ambient-noise recordings at a spatially dense array: Geophysical Journal International, v. 206, p. 980-992.

Salisbury, J.B., Rockwell, T.K., Middleton, T.J., and Hudnut, K.W., 2012, LiDAR and field observations of slip distribution for the most recent surface ruptures along the central San Jacinto Fault: Bulletin of the Seismological Society of America, v. 102, p. 598-619.

Salisbury, J. B., Haddad, D. E., Rockwell, T., Arrowsmith, J R., Madugo, C., Zielke, O., Scharer, K., 2015, Validation of meter-scale surface faulting offset measurements from high-resolution topographic data, Geosphere, v. 11, no. 6, p. 1–18.

Salisbury, B., Rockwell, T., and Buga, M., 2017, Paleoseismic Evidence for the 21 April 1918 Mw 6.9 Surface Rupture of the Northern Clark Strand of the Central San Jacinto Fault, California: Bulletin of the Seismological Society of America.Berkeley CA, v. 107, p. 1027-1032.

Sanders, C.O., and Kanamori, H., 1984, A seismotectonic analysis of the Anza Seismic Gap, San Jacinto Fault Zone, southern California: Journal of Geophysical Research: Solid Earth, v. 89, p. 5873-5890.

Sanders, C., Magistrale, H., and Kanamori, H., 1986, Rupture patterns and preshocks of large earthquakes in the southern San Jacinto fault zone: Bulletin of the Seismological Society of America, v. 76, p. 1187-1206.

Schwanghart, W., Scherler, D., 2014, TopoToolbox 2 – MATLAB-based software for topographic analysis and modeling in Earth surface sciences. Earth Surface Dynamics, v.2, p. 1-7.

Share, P., Ben-Zion, Y., Ross, Z.E., Qiu, H., and Vernon, F.L., 2017, Internal structure of the San Jacinto fault zone at Blackburn Saddle from seismic data of a linear array: Geophysical Journal International, v. 210, p. 819-832,

Sharp, R.V., 1967, San Jacinto fault zone in the Peninsular Ranges of Southern California: Geological Society of America Bulletin, v. 78, p. 705-729.

Sharp, R.V., 1981, Variable rates of Late Quaternary strike slip on the San Jacinto Fault Zone, southern California: Journal of Geophysical Research: Solid Earth, v. 86, p. 1754-1762.

Shi, Z., and Ben-Zion, Y., 2006, Dynamic rupture on a bimaterial interface governed by slip-weakening friction: Geophysical Journal International, v. 165, p. 469-484.

Sibson, R.H., 1977, Fault rocks and fault mechanisms: Journal of the Geological Society, v. 133, p. 191-213.

Sibson, R.H., 1985, Stopping of earthquake ruptures at dilational fault jogs: Nature, v. 316, p. 248.

Sibson, R.H., 1986, Rupture Interaction with Fault Jogs, *in* Earthquake Source Mechanics: American Geophysical Union, p. 157-167.

Sibson, R., 2011, The scope of earthquake geology, in: Fagereng, A., Toy, V. G., and Rowland, J. V., ed., Geology of the Earthquake Source: A Volume in Honour of Rick Sibson. Geological Society, London, Special Publications, p. 319-331.

Thatcher, W., Hileman, J., and Hanks, T., 1975, Seismic Slip Distribution along the San Jacinto Fault Zone, Southern California, and Its Implications: Bulletin of the Geological Society of America, v. 86, p. 1140-1146.

UNAVCO, 2010, San Jacinto Fault Zone at Anza B946 sagebf946bcs2010, Unpublished Installation Report.

US Geological Survey, 2006, Quaternary fault and fold database for the United States: https://earthquake.usgs.gov/hazards/qfaults/ (accessed January 2017).

Vernon, F. & Ben-Zion, Y.2010. San Jacinto Fault Zone Experiment. International Federation of Digital Seismograph Networks. Other/Seismic Network.

Watt, J.T., Graymer, R.W., Simpson, R.W., Ponce, D.A., Jachens, R.C., Phelps, G.A., and Wentworth, C.M., 2007, A Three-dimensional geologic model of the Hayward-Calaveras Fault junction: Eos Trans. AGU, v. 88, no. 52, Fall Meet. Suppl.

Wechsler, N., Rockwell, T.K., and Ben-Zion, Y., 2009, Application of high resolution DEM data to detect rock damage from geomorphic signals along the central San Jacinto Fault: Geomorphology, v. 113, p. 82-96.

Whearty, J.J., Rockwell, T. K., and Girty, G., 2017, Incipient pulverization at shallow burial depths along the San Jacinto fault , southern California, *in* Thomas, M.Y., Mitchell, T.M., and Bhat, H.S., ed., Fault Zone Dynamic Processes: Evolution of Fault Properties During Seismic Rupture, American Geophysical Union Monograph 227, p. 3-20.

Whitcomb, J.H., Allen, C.R., Garmany, J.D., and Hileman, J.A., 1973, San Fernando Earthquake series, 1971: Focal mechanisms and tectonics: Reviews of Geophysics, v. 11, p. 693-730.

Wilcox, R.E., Harding, T.P. and Seely, D.R. (1973). Basic wrench tectonics. The American Association of Petroleum Geologists Bulletin 57:1, 74–96.

Xu, S., and Ben-Zion, Y., 2017, Theoretical constraints on dynamic pulverization of fault zone rocks: Geophysical Journal International, v. 209, p. 282–296.

Yang, H., and Zhu, L., 2010, Shallow low-velocity zone of the San Jacinto fault from local earthquake waveform modelling: Geophysical Journal International, v. 183, p. 421-432.

Yang, H., Li, Z., Peng, Z., Ben-Zion, Y., and Vernon, F., 2014, Low-velocity zones along the San Jacinto Fault, Southern California, from body waves recorded in dense linear arrays: Journal of Geophysical Research: Solid Earth, v. 119, p. 8976-8990.

Zielke, O., Y. Klinger, and J R. Arrowsmith, 2015, Fault Slip and Earthquake Recurrence Along Strike-Slip Faults --Contributions of High-Resolution Geomorphic Data, Tectonophysics, v. 638, p. 43-62.